

THESIS

EFFECTS OF THE ADDITION OF BORON – NITRIDE NANOPATELETS TO
HYDROXYAPATITE: PROCESSING, TESTING, AND CHARACTERIZATION

Submitted by

Trevor G. Aguirre

Department of Mechanical Engineering

In partial fulfillment of the requirements

For the Degree of Master of Science

Colorado State University

Fort Collins, Colorado

Spring 2017

Master's Committee:

Advisor: Troy B. Holland

Donald W. Radford
James R. Neilson

Copyright by Trevor G. Aguirre 2017

All Rights Reserved

ABSTRACT

EFFECTS OF THE ADDITION OF BORON – NITRIDE NANOPATELETS TO HYDROXYAPATITE: PROCESSING, TESTING, AND CHARACTERIZATION

Bioceramics range in biocompatibility from inert oxides that do not react with the body to the other extreme of materials that completely absorbed by the human body, but are prone to failure by fracture. Limited fracture toughness (K_{IC}) and flexural strength (σ_{FS}) are major factors limiting wider scale application as structural implant materials. K_{IC} and σ_{FS} of ceramics can be improved through grain size refinement and through the addition of various reinforcement materials. The bioceramic hydroxyapatite (HA), the primary inorganic component of bone, has excellent osteoconductivity which offers a suitable surface for new bone growth and integration but suffers from low K_{IC} .

To improve the K_{IC} of HA we used boron nitride nanoplatelets (BNNPs), a strong and biocompatible material, making them excellent candidate for use in the human body. However, these materials have been shown to cause embrittlement of the material they are incorporated in; thus, it becomes important to understand the effect of BNNPs through analysis of the failure statistics of tested samples.

Using spark plasma sintering to create these materials HA – BNNP composites with 0.5, 1.0 and 2.0 wt% BNNPs were fabricated. Sample grain sizes were measured to evaluate the effect the BNNPs had on the microstructure and the flexural strength, fracture toughness, and hardness were tested to observe the effect BNNP had on the mechanical properties of HA and as well as the failure statistics. To analyze the failure statistics of the HA BNNP composites the Weibull

Distribution was used because studies have shown that the Normal Distribution does not accurately report the failure statistics of brittle materials.

This work summarizes the effect of the addition of BNNPs to spark plasma sintered HA. The results of this study show that BNNPs are capable of increasing flexural strength and fracture toughness through grain size refinement but BNNPs lead to a measurable decrease in the reliability of the material, which is indicative of the predictability of measured material property value and yields information about the flaw distributions in these materials.

ACKNOWLEDGEMENTS

I would like to thank my advisor for providing invaluable feedback and guidance when I started on this project and allowing me to develop into a scientist at my own pace.

I would like to thank the members of the AMPT Lab: Corson Cramer, Paul Colasuonno, Thomas Hamman, Vincent Torres, and Tucker Hensen for their help and support.

I would like thank my family and friends for their patience, understanding, and continual emotional support, without which I would have not succeeded in this endeavor.

Most importantly I would like to thank my parents for raising me to value education and giving me the work ethic and desire to succeed with my education.

TABLE OF CONTENTS

ABSTRACT.....	ii
ACKNOWLEDGEMENTS.....	iv
CHAPTER 1: OVERVIEW OF STUDY	1
1.1. Significance	1
1.2. Introduction	2
1.2.1. Background.....	2
1.2.2. Literature review	4
1.2.3. Cytotoxicity.....	7
1.2.4. Fabrication	7
1.3. Scope	8
1.3.1. Project Principal.....	8
1.3.2. Hypothesis.....	8
1.3.3. Aim of research.....	9
CHAPTER 2: THEORY	10
1.4. Fracture Mechanics and Testing.....	10
1.4.1. Griffith Crack Theory	10
1.4.2. Testing.....	11
1.5. Fracture Toughness.....	13
1.5.1. Intrinsic and Extrinsic Toughness.....	13

1.6.	Fractures: Metal, Ceramics, Porous materials, and Modes	14
1.6.1.	Metals.....	14
1.6.2.	Ceramics	18
1.6.3.	Porous materials.....	19
1.6.4.	Modes of fracture.....	21
1.7.	Strengthening mechanisms: Metals and Ceramics	23
1.7.1.	Metals.....	23
1.7.2.	Ceramics	23
CHAPTER 3: METHODS.....		25
1.8.	Spark Plasma Sintering.....	25
1.8.1.	Theory.....	25
1.8.2.	Tooling.....	27
1.9.	Powder Preparation.....	28
1.10.	Densification Parameters	28
1.11.	Sample preparation for mechanical testing.....	30
1.12.	Mechanical Testing.....	33
1.12.1.	Single Edge V Notch Testing (SEVNB).....	33
1.12.2.	Vickers Hardness Testing.....	34
1.12.3.	Vickers Indentation Fracture (VIF).....	36
1.12.4.	Flexural Testing.....	37

1.13.	Grain Size Analysis.....	38
1.14.	Experimental Shortcomings.....	38
1.15.	Taguchi Design of Experiments.....	38
1.16.	Weibull Analysis.....	39
1.17.	Characterization	41
1.18.	American Society for Testing and Materials (ASTM) specifications	42
CHAPTER 4: RESULTS.....		43
1.19.	Taguchi Design of Experiments.....	43
1.20.	Characterization	44
1.21.	Grain Size and Fracture Surfaces.....	46
1.22.	Flexural testing: Average and Weibull Distribution.....	47
1.23.	Vickers Hardness testing: Average and Weibull Distribution.....	50
1.24.	Fracture toughness: Average and Weibull Distribution.....	52
1.25.	Summary of Nanoplatelet effect on Weibull Distribution.....	55
CHAPTER 5: DISCUSSION.....		57
1.26.	Effect of tooling	57
1.26.1.	Potential Issues.....	57
1.27.	Thermal stability	60
1.28.	Densification.....	60
1.29.	Grain size effect on mechanical properties.....	63

1.30.	Mechanical Testing.....	66
1.30.1.	Flexural Testing.....	66
1.30.2.	Vickers Hardness.....	70
1.30.3.	Fracture Toughness	70
1.31.	Statistical Effects of BNNP Addition to Hydroxyapatite	76
1.32.	Statistically Designed Loading of Materials.....	78
CHAPTER 6: CONCLUSIONS		80
CHAPTER 7: FUTURE DIRECTIONS.....		82
1.33.	Pressure effects on the mechanical properties of hydroxyapatite.....	82
1.34.	BN nanotubes.....	84
1.35.	Homogenous dispersion.....	84
1.36.	Surface functionalization of BNNTs	86
REFERENCES		89

CHAPTER 1: OVERVIEW OF STUDY

1.1. Significance

Due to the inability to manufacture hierarchical structures similar to natural materials and consequently match their mechanical properties it is necessary to design and manufacture new materials in an attempt to mimic these properties. The intrinsic fracture toughness of human cortical bone is $2.38 \text{ MPa}\sqrt{m}$ [2], of human cancellous bone (depending on relative density) is between $0.05 - 1 \text{ MPa}\sqrt{m}$ [3], and for pure hydroxyapatite is $1.0 \text{ MPa}\sqrt{m}$ [4]. This difference in fracture toughness is due to the hierarchical structure of the bone. In order to match these properties new measures must be taken. This research investigated the effects of adding boron nitride nanoplatelets to hydroxyapatite. Though research on the effects of adding boron nitride nanotubes to various materials, including hydroxyapatite, exist in the literature there has been no research into adding boron nitride nanoplatelets. Therefore, this study is the first to investigate the toughening effect of boron nitride nanoplatelets. Due to low intrinsic fracture toughness of HA the proposed research serves to create a suitable implant material for non-loading bearing maxillofacial and cranial bones by toughening hydroxyapatite and mimicking the fracture toughness of the native bone.

1.2. Introduction

1.2.1. Background

Ceramics, specifically bioceramics¹, have been used in the medical industry for various purposes. Bioceramics range in biocompatibility from ceramic oxides, which do not react with the chemistry of the human body to the other extreme of resorbable materials, which are eventually replaced by the materials which they are used to repair. A primary medical procedure where bioceramics are used is in implants. However, ceramics are inherently brittle due to the nature of their bonding and susceptible to failure by fracture. Studies to improve the mechanical properties of ceramics, specifically of the bioceramic hydroxyapatite (HA), the addition different materials have been investigated various scientists. These materials include alumina and titania, graphene, carbon nanotubes, boron nitride nanotubes, and more [1,4,6–9].

Materials possess low fracture toughness relative to their theoretical capacity because most materials deform plastically at much lower stress levels and eventually fail by an accumulation of this irreversible damage. In addition, engineering materials may contain defects that are microstructural in origin or introduced during manufacture. These defects include porosity, shrinkage cavities, quench cracks, grinding and stamping marks, seams, and weld related cracks. Other constituents, such as inclusions, brittle second phase particles, and grain-boundary films, can lead to crack formation if the applied stress level exceeds some critical value [10]. Therefore, it becomes crucial to understand how the material will behave before, at, and after the critical stress level to cause crack propagation in the presence of defects.

¹ Bioceramics are ceramic materials that are biocompatible [5].

Ceramics are inherently prone to failure by fracture [10,11] However, the mechanical properties of ceramics can be extrinsically improved through the addition of other materials [4,12–15].

Carbon nanotubes (CNTs) when added to HA can improve the fracture toughness of the composite through crack bridging, crack deflection, pull-out, and grain bridging [6] and provide nucleation sites for micro-cracks ahead of the main crack [15]. All the listed benefits in one way or another provide a form of energy dissipation that would have otherwise gone into crack extension or provide a means of increasing the energy needed to cause crack extension. Crack bridging improves the toughness by creating a “bridge” between the crack faces, increasing the energy needed to extend the crack further (i.e. cause the bridged surfaces to become further apart). Crack deflection increases the tortuosity² of the crack path and thus the energy needed to cause crack extension. Pull-out like crack bridging increases the energy needed for crack extension by dissipating energy to the matrix before the element (grain, fiber, whisker, or sheet) is pulled out of the matrix. Pull-out has higher effect on improving the toughness strong bond (mechanical or chemical) exists between the constituent and the matrix, which results in a higher interfacial shear stress needed before the element can be pulled out [14]. Grain bridging works through the added element (fiber, whisker, or sheet) distributing an applied load across several grains thus increasing the load (energy) needed to cause fracture to propagate through a single grain [17]. Micro-cracks are small cracks that form ahead of the main crack tip and dissipate energy through the creation of new crack surfaces and cause a volume expansion which tries to close the crack through induced compressive stresses.

² Tortuosity is a property of a curve being tortuous (twisted; having many turns) [16].

However, these toughening mechanisms are not unique to CNTs. The effects seen are because of the introduction of an outside material to the HA matrix. CNTs have been reported as cytotoxic and non-cytotoxic while at the same time being reported in promoting bone growth [1,12,13]. This difference in reporting leaves the debate open about using CNTs in bioceramic implants [1]. As mentioned before, even though several biomedical applications of CNTs have already been proposed, the use of BNNPs in this field has been unexplored [18]. BNNPs has been proven to be non-cytotoxic [19,9] have high strength comparable to CNT, and are capable of providing the same extrinsic toughening mechanisms as CNTs.

1.2.2. *Literature review*

The bioactivity and osteoconductivity of hydroxyapatite offers a suitable surface for new bone growth and integration [1]. HA has the hexagonal crystal structure is ionically bonded. This combination leads to brittle behavior because of the lack of close packed planes to accommodate dislocation motion and for dislocation motion to occur similarly charged atoms would have to slide past each other. Attempts have been made to improve the mechanical properties of HA through various methods. Aminzare, et al., created two different composites of HA reinforced with alumina and titania, respectively [4]. It was discovered the addition of these oxides improved densification and mechanical behavior of HA and postponed the decomposition of HA to tricalcium phosphate (TCP) from 1250 °C to 1300 °C and 1400 °C, respectively, and also increased flexural strength and hardness. These improvements originate from the formation of calcium aluminates and calcium titanates [4].

Tubular structures have been shown to strengthen the matrix they are added to. CNTs have been shown to strengthen HA. CNTs, an allotrope of carbon, can be envisioned as sheets of graphite rolled into tubes with hemispherical fullerene caps on the ends [20]. A single sheet of graphite,

known as graphene, can be rolled in different directions to produce nanotubes with different configurations. Graphene is known to have a tensile strength of 130 GPa and an elastic modulus of 0.5 – 1 TPa. In the studies of Zhang et al graphene nanosheets (GNSs) we added to HA, where GNSs can be thought of as a single walled CNT that has been cut down the middle and unrolled and exhibits the same mechanical properties as CNT. It was discovered that GNSs, when added to HA powder and solidified via spark – plasma – sintering (SPS), wrapped around HA grains, which enhances mechanical interlocking and thus increases load transfer from the sheet to the matrix. The study also yielded an ~80% increase in fracture toughness through crack bridging, crack deflection, pull-out, and grain bridging due to the GNSs [6]. Ramirez et al. have reported 135% increasing using GNS reinforcement in Si_3N_4 ceramics, due to nucleation of micro-cracks in the nanosheet direction [21]. These results show that the addition of a sheet-like structure can increase the fracture toughness of a composite. Nieto et al. [22] have shown an increased toughness due to the incorporation of graphene nanoplatelets (GNPs) into an alumina matrix with varying volume fractions. Where GNPs are stacks of GNSs.

Boron nitride nanotubes (BNNTs) have also been shown to improve the mechanical properties of a matrix. Boron nitride is an inorganic compound with chemical formula BN. BNNTs can be thought of as a CNT, but with boron and nitrogen replacing the carbon atoms, in a similar lattice. It is known that BNNTs are equally as mechanically robust as CNTs where studies have indicated that BNNT exhibit excellent elastic properties and the mechanical stiffness of BNNT challenge the stiffness of CNT and have been reported with an elastic modulus of 1.3 TPa [23]. They have been reported as having an elastic modulus of 1.5 TPa. In one study, Lahiri et. al have reported a polylactide–polycaprolactone copolymer (PLC) reinforced with 2 and 5 wt. % BNNTs for an orthopedic scaffold application [19]. The elastic modulus of the 5 wt% composites showed a

1370% increase, while the tensile strength showed 109% increase, without any adverse effect on the ductility, which was reported as 240% elongation. Even though PLC is polymer, and is outside the scope of this project, this shows that the addition of BNNTS can greatly improve the mechanical properties of a composite. Several other studies have investigated the addition of BNNT to different ceramics such as Si_3N_4 , Al_2O_3 , SiO_2 , and HA [24–28] and it has been shown that the mechanical properties of the composite were higher than the monolithic material. In one study, Lahiri et al. reported 120% increase to elastic modulus, 129% harder, and 86% greater fracture toughness in a 5 wt% BNNTs – HA composite as compared to the similarly prepared pure HA samples [9]. The BNNTs was found to have a sufficient lattice match with the HA, therefore strong interfacial bonding caused the increase in modulus. The fracture toughness was improved crack bridging due to the BNNTs.

Boron nitride nanoplates (BNNP) are 5 – 10 layer stacks of hexagonal boron nitride and are structurally analogous to GNP and to the author's knowledge; there are no discussions or research investigating the addition of BNNP to HA. It is important to investigate the properties of sheets versus tubes because it has been shown via finite element models that the efficiency of load transfer to the matrix decreases with increasing number of layers in multi-walled carbon nanotubes, due to poor interfacial bonding between layers caused by low strength van der Waal's interactions [29,30]. BNNT and CNT, when synthesized are often multi-layered and suffer from this problem and plates suffer less from this problem. Since it has been shown that plate like structure can increase mechanical properties BNNPs serve as a novel method for increasing the mechanical properties of HA.

1.2.3. *Cytotoxicity*

HA–CNT composite systems are intended for orthopedic application in a living body. Therefore, it is extremely important to assess their biocompatibility. The biocompatibility of CNT is still under debate due to contradictory reports [1,8]. For example, Cherukuri et al. reported that CNT can be ingested by macrophages without producing any toxic effect [12], whereas Cheng et al. have reported incomplete consumption of CNT in macrophages, causing irreparable tissue damage and thus, cell death [31]. However, there have been multiple reports of CNT being able to promote accelerated bone growth due to the porous CNT matrix [7,32,33]. Comprehensive reviews on this issue have agreed that the reported cytotoxic response of a CNT is mostly not due to CNT itself, but is associated transition metal catalyst particles, degree of agglomeration, and surface defects [34–38]. However, the debate is still open. BNNTs seem to be non-toxic, making them favorable candidates for biomedical applications. Although several biomedical applications of CNTs have already been proposed, the use of BNNTs in this field has largely been unexplored [18]. Although, BNNTs interactions with osteoblasts and macrophages prove them to be non-cytotoxic (biocompatible) [19]. Because BNNPs are unrolled BNNTs it is assumed the biological response will be the same, though this still needs to be fully investigated.

1.2.4. *Fabrication*

It has been shown that high heating rates are readily able to produce nanogranular materials via SPS [39]. Therefore, SPS is the best method for obtaining nanogranular materials. It is well known that grain size strengthening is an effective method for toughening metals due to increased impedance to dislocation motion due to an increased amount of grain boundaries [20]. This method also applies to ceramics; however impeded dislocation motion is not the mechanism by which toughening occurs. Grain boundaries represent areas of atomic disorder (mismatch),

which act as barriers and thus increase crack path tortuosity and increase the fracture toughness.

An important thing to note is that this is only observed in nanogranular ceramics. Grain size independence of the fracture toughness has been shown in alumina for grain sizes in the 0.5 – 3.0 micrometer range [40] and a decrease for hydroxyapatite in the range 4.6 – 6.4 μm [41] .

However, it has been shown decreasing grain size leads to increased fracture toughness in FeMoSiB [42] in the 11 – 25 nanometer range as well as in hydroxyapatite for grain sizes smaller than 141 nanometers [43].

In conclusion, it has been shown that plate-like structure can lead to increases in fracture toughness. This coupled with mixed cytotoxicity reports of CNTs and the non-cytotoxic response of BNNTs it can be concluded that BNNPs are great candidates to increase fracture toughness, while maintaining cytocompatibility. It has also been shown that decreasing grain size increases fracture toughness. Therefore, ultrafine grained ($< 1 \mu\text{m}$) HA with added BNNPs are an ideal candidate for a suitable and tough implant material.

1.3. Scope

1.3.1. Project Principal

To investigate the effects of adding boron nitride nanoplates to spark plasma sintered HA to toughen the composite for applications in the human body.

1.3.2. Hypothesis

Due to the high stiffness of boron nitride the addition of boron nitride nanoplates to hydroxyapatite will increase the fracture toughness and flexural strength of the composite.

1.3.3. *Aim of research*

Nanometric (~ 40 nm) hydroxyapatite powders were consolidated using spark-plasma sintering. Boron nitride nanoplates were added to the hydroxyapatite matrix in predetermined weight fractions of 0.5, 1.0, and 2.0 %, respectively. For mechanical testing, pure hydroxyapatite and composite samples, rectangular sections that are 3 x 3 x 20 mm were cut and polished for fracture toughness testing via Vickers indentation and by the single edge V-notch (SEVNB) method. Both indentation and the SEVNB methods can verify the hardness and fracture toughness through empirically derived relations. Due to the stochastic nature of ceramics, data reliability will be assessed via the Weibull distribution, where a large Weibull modulus indicates high reliability and conversely a low Weibull modulus indicates low reliability.

CHAPTER 2: THEORY

1.4. Fracture Mechanics and Testing

1.4.1. Griffith Crack Theory

Alan Griffith noted that when a crack is introduced to a stressed plate of elastic material, a balance must be struck between the decrease in potential energy, which is related to the release of stored elastic energy and work done by the external load, and the increase in surface energy resulting from the presence of the crack. Likewise, an existing crack would grow by some increment if the necessary additional surface energy were supplied by the system. This “surface energy” arises from the fact that there is a non-equilibrium configuration of nearest neighbor atoms at any surface in a solid [10]. Using the model of a full-thickness crack through a large plate he postulated that the change in the potential energy of the plate associated with the introduction of a crack may be given by Equation 1:

$$U - U_0 = -\frac{\pi\sigma^2 a^2 t}{E} + 4at\gamma_s \quad (1)$$

Where, U is the potential energy of the cracked body, U_0 is the potential energy of the uncracked body, σ is the applied stress, a is the crack half-width, t is the thickness, E is the modulus of elasticity, and γ_s is the specific surface energy [10]. With some simplifications and assumptions Griffith came to Equation 2 for computing the stress at the crack tip.

$$\sigma = \sqrt{\frac{2E\gamma_s}{\pi a}} \quad (2)$$

However, this equation does not take into consideration the radius of curvature of the crack tip and is therefore not a sufficient method for calculating the failure stress.

Building on this result Egon Orowan developed Equation 3.

$$\sigma_a = \frac{1}{2} \sqrt{\frac{2E\gamma_S}{a} \left(\frac{\rho}{a_0}\right)} = \frac{1}{2} \sqrt{\frac{2E\gamma_S}{\pi a} \left(\frac{\pi\rho}{8a_0}\right)} \quad (3)$$

Where a_0 is the equilibrium atomic separation, σ_a is the applied stress for fracture, and ρ is the radius of curvature at the tip of the crack. It can now be seen if the radius of curvature ρ is equivalent to $8\frac{a_0}{\pi}$ then Equation 2 reduces to 3, meaning that the Griffith equation (Equation 2) is valid for ρ less than $8\frac{a_0}{\pi}$.

At the same time Orowan modified the Griffith equation George Irwin considered an approach to fracture in materials that could deform plastically. He developed an approach that considered the energy that would initiate a crack (source) instead of the energy need to continue crack propagation (sink) [10] (Eq. 4).

$$\sigma = \sqrt{\frac{E\Upsilon}{\pi a}} \quad (4)$$

Where Υ is the elastic strain energy release rate which is the crack driving force.

1.4.2. *Testing*

Due to the contributions of Griffith, Orowan, and Irwin it became possible to perform and interpret fracture toughness tests. Before these concepts engineers would conduct tests with laboratory-sized samples under testing conditions that would simulate field failures. However, these tests often suppressed the capacity of the material to deform plastically such as low testing temperatures, high strain rates, and multi-axial stress states caused by the presence of a notch or defect in a sample and plastic deformation which are of importance in some metals. For example, body-centered-cubic (BCC) metals, such as ferritic steel alloys, are far more sensitive

to temperature and strain rate than are face-centered-cubic (FCC) metals such as copper, nickel, and aluminum [10].

One test that can be performed due the contributions of Griffith, Orowan, and Irwin is the Charpy Impact Test. A notched sample is loaded at very high strain rates by forcing the material to absorb impact from a falling pendulum (Figure 1, [44]). The energy absorbed during impact can be calculated by measuring the initial and final heights of the pendulum. These tests can be performed at various temperatures to directly see the effect of temperature on fracture toughness. It can be shown that there is a decrease in absorbed energy as temperature decreases due to a transition from ductile failure to brittle failure. This has lead engineers to design components to have operating temperatures higher the than temperature at which brittle failure of the component would occur [10].

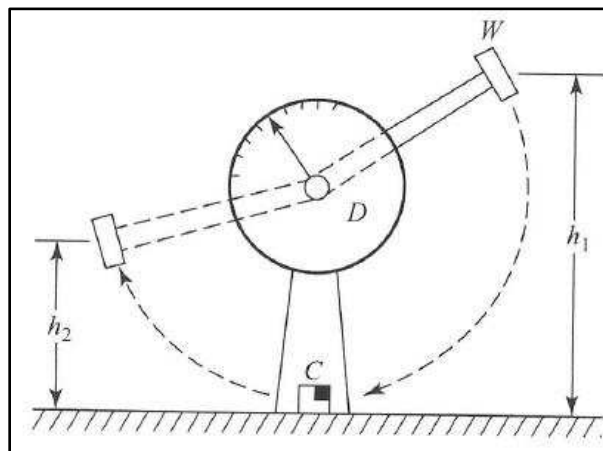


Figure 1: Diagram showing impact hammer W dropping from height h_1 , impacting sample C and rising to maximum final height h_2 .

These tests ultimately lead to the development of new theories and other tests for determining fracture toughness.

1.5. Fracture Toughness

It is important to note here that fracture toughness is a material property. Values of fracture toughness vary between classes of materials (metals, ceramics, polymers, woods, composites, etc.), vary inside the class of materials (steel, copper, nickel) and even vary within the alloy (1080, 1015, 304S steels). Fracture toughness of a given material is dependent on its intrinsic and extrinsic toughness.

1.5.1. *Intrinsic and Extrinsic Toughness*

Intrinsic toughness is defined as the aspects of a materials structure that have fundamental influence on fracture resistance. Atomic bonding provides the bases for the great differences in toughness among the different classes of materials. In general, it is seen that the more rigid the bond (ionic or covalent) the more brittle the material is likely to be. Covalent bonding involves the sharing of valence electrons between atoms and their nearest neighbors and tends to be brittle. Ionic bonds involve donating an electron to another atom and which are less restrictive bonds, therefore less brittle than covalently bonded materials. Furthermore, great ductility is seen in monovalent ionic materials as compared to multivalent ionic materials. Ductility in these materials is also dependent on the number of independent slip systems. This causes a tendency for brittle behavior because during deformation similarly charged ions may be forced to slide past each other, thus resisting the deformation. Materials with ionic, covalent, or mixed type bonds (glasses and ceramics) tend to have low intrinsic toughness and little improvement is available by alterations of the chemical composition. Metallic bonding, on the other hand, provides the least restriction of valence electron movement because all valence electrons are shared by all atoms in the solid. Metals generally have the greatest deformation capability and the greatest intrinsic toughness [10].

Intrinsic toughness is also related to the atomic arrangement of the material crystal structure.

Brittle behavior is more prevalent in materials of low crystal symmetry due to the difficulty for slip to occur and conversely, considerable ductility is seen in close-packed metals with high crystal symmetry. BCC metals have more slip systems than do FCC metals and consequently show higher intrinsic toughness, because of the ability to accommodate more slip.

Extrinsic toughness is defined as the aspects of a material that reduce the crack driving force rather than dissipating the crack energy. The first mechanism of extrinsic toughness is crack deflection. Deflection can be accomplished either by interaction of the crack with particles or with weak planes in the materials. When hard discrete particles in brittle matrices act to temporarily pin the advancing crack energy is dissipated because of the decrease in the crack propagation rate. This forces the crack to move around both sides of the particle before linking back together and continuing behind the particle. A second, mechanism of enhancing extrinsic toughness is the transformation of unstable phases to more stable phases. This volume expansion/contraction leads to dissipation of energy and in the case of volume contraction leads to favorable compressive forces. A third mechanism is referred to as contact shielding. Contact shielding is the physical contact of fracture surfaces behind the crack. Contact shielding may also be seen in the form of unbroken fibers “bridging” the gap between fracture surfaces [10].

1.6. Fractures: Metal, Ceramics, Porous materials, and Modes

1.6.1. Metals

Metals are often thought of as solids composed of atoms held together by a matrix of electrons, which are free to move anywhere in the crystal. When crystalline solids are subjected to loads, on the atomic scale, there is a tendency to pull the atoms apart. If the bonds between the atoms are very strong, there is a tendency to cleave the crystals apart. In metals, the interatomic bonds

are such that rather than causing cleavage, loading can cause atomic slip through dislocation motion. A dislocation is a crystal imperfection characterized by regions atomic disorder where neighboring atoms do not properly surround the site where the dislocation is, which in turn is a site where an atom once was. When metals are deformed, the atoms making up the crystalline structure of the metal rearrange to accommodate the deformation, where dislocation motion is the primary mechanism. Dislocations can be produced by crystal mismatch during solidification, can be introduced by plastic deformation, can occur by phase transformations that cause atomic mismatch, or can be caused by alloying elements that cause atomic mismatch. Deformation by dislocation motion is one of the characteristics that make metals useful engineering materials. Many metals can tolerate significant plastic deformation before failing; the same cannot be said for ceramics [44].

Metals have the greatest potential for high fracture toughness of any material class, which is the primary reason that metals are so widely used for structural applications [10]. Metals can prevent dislocations and blunt crack tips via one or more of the following: work hardening, solution hardening, precipitation hardening, grain boundary strengthening, and transformation hardening. Solution hardening and precipitation hardening can serve to blunt crack tips when the crack encounters a material of larger atomic size than that of the parent material. The same methods also serve in preventing dislocation motion. However, this decreases ductility which decreases the fracture toughness of a material. Therefore, there is trade off by which you can improve the fracture toughness of a metal, while improving other mechanical properties.

Metals that are capable of plastic deformation tend to fail by a process called microvoid coalescence (MVC). This fracture mechanism, observed in most metallic alloys, takes place by the nucleation of microvoids, followed by their growth and eventual coalescence into a crack.

These mechanically induced micropores should not be confused with preexisting microporosity sometimes present because of a casting or sintering process. Depending on the nature of the loading, the MVC on the surface will appear differently (Figure 2, [10]). In addition to MVC, two other fracture micro-mechanisms can occur in metals: intergranular fracture and cleavage fracture [10].

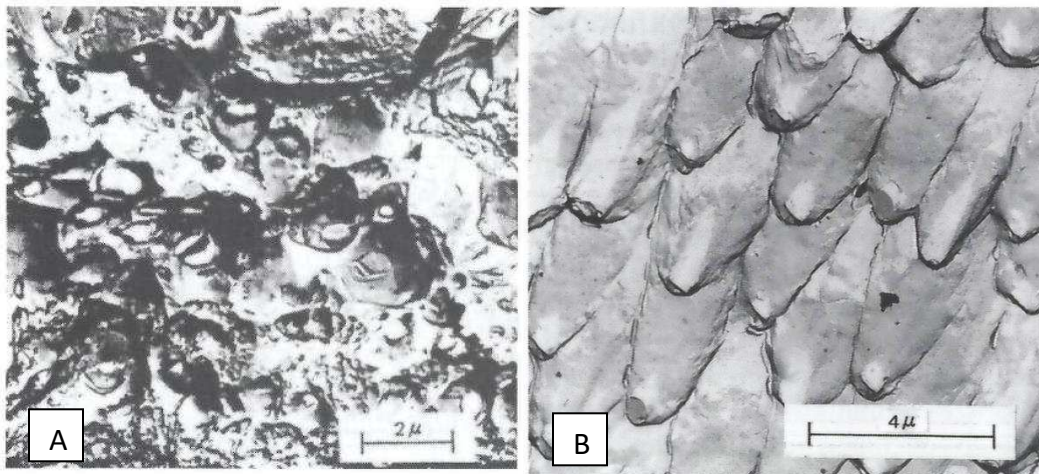


Figure 2: (A) SEM image of MVC under tensile loading ("equiaxed dimple" morphology). (B) SEM image of MVC under shear loading ("elongated dimple" morphology) [10]

Intergranular failure is characterized by crack growth primarily along grain boundaries. It leaves behind a fracture plane with exposed grain boundary surfaces and a distinctly faceted morphology (Figure 3, [10]). Intergranular fracture can result from a number of processes. These include microvoid nucleation and coalescence at inclusions or second-phase particles located along grain boundaries; grain-boundary crack and cavity formations associated with elevated temperature stress rupture conditions, decohesion between contiguous grains due to the presence of impurity elements at grain boundaries and in association with aggressive atmospheres such as gaseous hydrogen and chemical dissolution along grain boundaries. If the

material has an insufficient number of independent slip systems to accommodate plastic deformation between contiguous grains, grain boundary separation may occur [10].

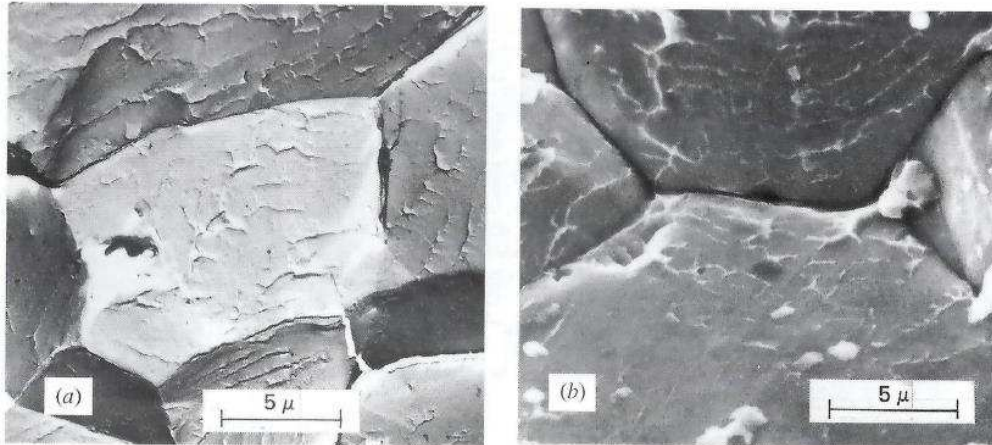


Figure 3: Intergranular fracture in steel: (a) TEM; (b) SEM [10]

The process of metal cleavage (Figure 4, [10]) involves transgranular fracture along specific crystallographic planes. This mechanism is commonly observed in certain BCC and HCP metals, but can also occur in FCC metals when they are subjected to severe environmental conditions such as extremely high strain rates or very low temperatures. A relatively flat fracture surface with small converging ridges known as river patterns within many of the grains is indicative of cleavage fracture. [10].

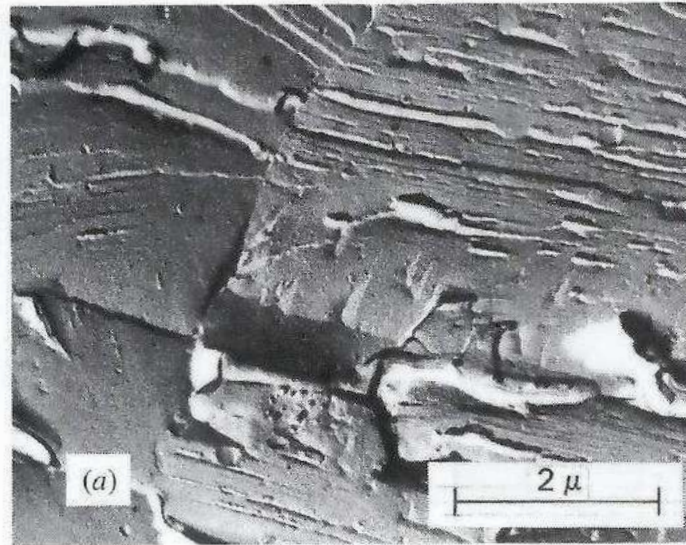


Figure 4: TEM image of cleavage fracture in a low-carbon steel [10]

1.6.2. *Ceramics*

A ceramic can be defined as a combination of one or more metals with a nonmetallic element.

What distinguishes ceramics from other engineering materials is the nature of the interatomic bonds. As opposed to the long-range “sea of electrons” in metals, ceramic materials usually have very rigid covalent or ionic bonds. Both ionic and covalent bonds involve very strong bonds between neighboring atoms where electrons are shared or donated, respectively. Because of these charged bonds it makes it difficult to move dislocations because atoms would have to relocate to a site with same charge before making to a site with opposite charge. Thus, crystalline ceramics with these types of bonds tend to be very brittle, where tensile loading tends to result in crystal cleavage [44].

In ceramics the occurrence of intergranular fracture (Figure 5, [10]) is indicative of a number of processes typically associated with slow crack growth. The fracture often proceeds along grain boundaries where the material is weakest. When the crack grows to a critical size it will

transition to a fast-fracture mode. As it does a considerable amount of transgranular fracture may develop [10].

Transgranular (or transcrystalline) (Figure 5, [10]) fracture occurs along specific crystallographic planes just as it does in metals. This cleavage process results in a morphology that is typically flat. Although within individual grains it may appear as a parallel plateau and ledge morphology. Often these cleavage steps appear as river patterns wherein fine steps are seen to merge progressively into larger ones [10].

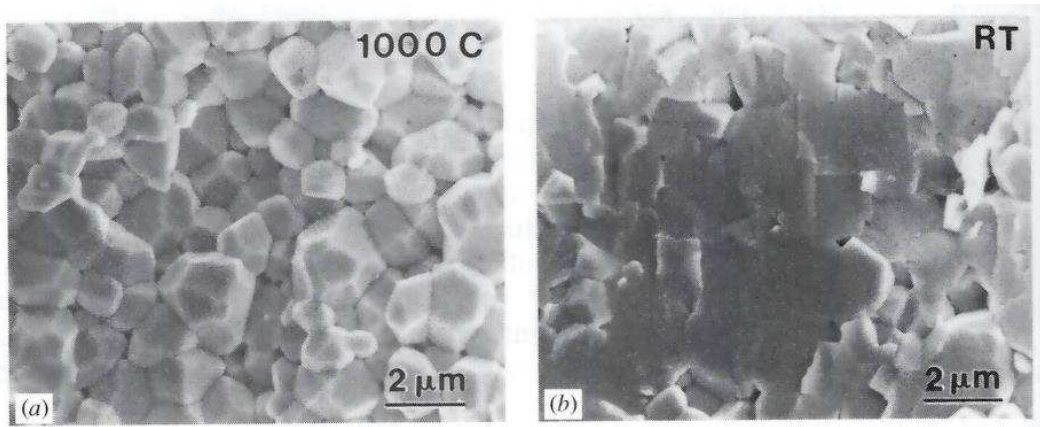


Figure 5: (a) ZrO₂ intergranular fracture at high temperature and (b) transgranular fracture at room temperature [10]

1.6.3. Porous materials

The random distribution of pores in location, size, and shape makes the fracture of porous materials a very difficult problem and there is not much literature available to help with the issue. Assuming the pore size is small, compared to the component, a fracture criterion involving both toughness and tensile strength has allowed the study of the competition between the crack blunting due to the pores and resulting in toughness enhancement and the weakening effect caused by the increased volume of pores. [1]. This study dealt with fracture in ceramics and therefore is most useful in context of this discussion and the author's research area. Through

experimentation Leguillon and Piat discovered that if the distance between pores is small the crack has enough energy to “jump” from one pore to the next leading to an apparent weakening effect. Conversely for larger distances between pores and low crack initiation energy (low applied stress) the crack cannot make the “jump” to the next pore to initiate further cracking and thus leads to an apparent strengthening effect (Figure 6, [45]). However, this did not stop the crack, it merely stops it from “jumping” to the next pore, crack growth still occurs toward the next pore. It is important to note that there is always a weakening effect due to the presence of the pores. In their study, Leguillon and Piat, define μ as the crack length and ζ as the distance between pores [45].

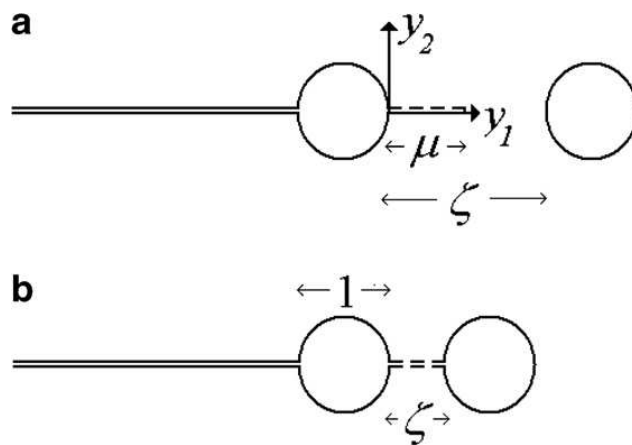


Figure 6: Two pores and the expected crack path (a) mixed criterion where $\mu < \zeta$, (b) $\mu > \zeta$ [45]

In a different study, discrete-element-method (DEM) numerical simulations were performed to compute the effective strengths of porous microstructures in tension as function of porosity. The DEM simulations were performed on microstructures typical of partially sintered ceramics in investigate the fracture behavior. A first approach consisted in recording the fracture stress of homogeneous samples that did not contain defects larger than the characteristic length scale of

the sample microstructure. However, brittle fracture of ceramics is known to initiate at surface defects created during the manufacturing process that produced the ceramic. Their DEM simulation used defect free “samples”, because it would require much larger “sample” sizes for samples with defects. Therefore, they believed that the obtained fracture stresses overestimated experimental values. However, after experimentation the fracture toughness values obtained by the simulation over a large density range agreed with experimental data, thus validating their approach [46].

1.6.4. *Modes of fracture*

The Griffith, Orowan, and Irwin approaches (above) provide important conceptual and practical ways to inform design decisions but their limitations leave considerable uncertainty for assessing the likelihood of component failure due to fracture. A more sophisticated approach to the fracture of flawed components is available through a stress analyses based on the elastic theory [10]. There are three modes of loading that cause crack propagation, i.e., fracture. A graphical depiction of each failure mode can be seen in Figure 7, [10].

1. Mode 1 – Opening or tensile mode, where the crack surfaces move directly apart.
2. Mode 2 – Sliding or in-plane shear mode, where the crack surfaces slide over one another in a direction perpendicular to the leading edge of the crack.
3. Mode 3 – Tearing or anti-plane shear mode, where the crack surfaces move relative to one another parallel to the leading edge of the crack.

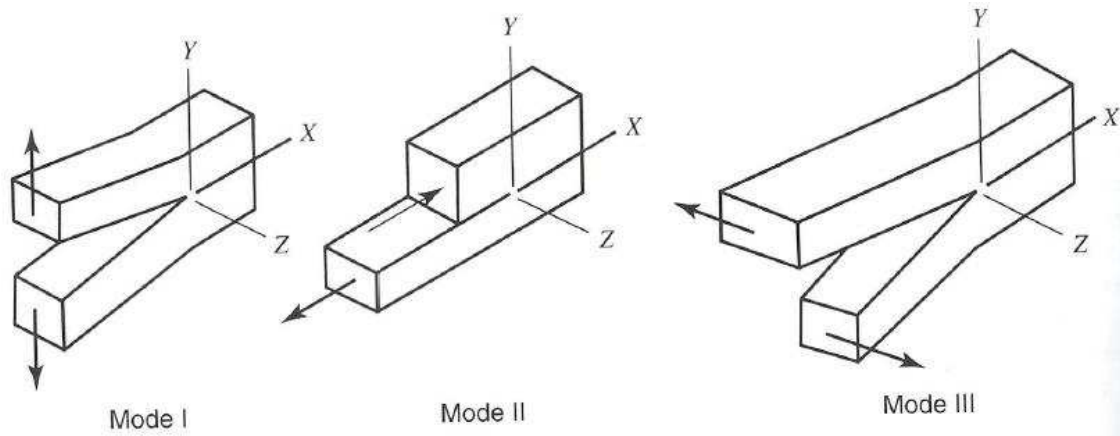


Figure 7: Mode 1, 2, and 3 fracture [10]

Mode 1 loading is encountered in the majority of actual engineering situations involving cracked components. Mode 2 happens less frequently in structural components, but is useful when analyzing the failure of adhesive joints. Mode 3 can be regarded as a pure shear problem, such as during torsion testing. Since Mode 1 is the dominant form of loading in engineering applications, and most applicable to ceramics, much research and testing has been performed to understand and quantify fracture due to this loading mode to help prevent failure and drive design decisions [10]. To help understand how this can drive design decisions it is useful to define:

$$K = \sigma Y \sqrt{\pi a} \quad (5)$$

Where K is the stress field parameter that describes the intensity of the stress concentration, σ is the applied stress, Y is a geometry parameter of the system, and 'a' is the crack half-width.

It can be seen that for a known crack size (through experimental design or NDT detection) and a fixed value of K , one can design for a value of σ less than the ratio of $K / Y \sqrt{\pi a}$ [10].

1.7. Strengthening mechanisms: Metals and Ceramics

1.7.1. *Metals*

There are several methods by which a metal can be strengthened to resist dislocation movement, which in turn have a negative effect on the metal's ability to resist fracture (i.e., causes a decrease in ductility and therefore a decrease in fracture toughness)

- Solid solution strengthening – impurity atoms (alloying elements) are added to a pure metal [44].
- Precipitation hardening – a strengthening mechanism that relies on a sequence of solid-state transformations in generating a dispersion of ultra-fine particles of a second phase [47].
- Dispersion strengthening – increasing the strength of a material by forming more than one phase [47].
- Grain size strengthening – increasing the number of grains or reducing the grain size to cause surface imperfections which block dislocation movement [47].
- Strain-hardening – strengthening of a material by increasing the number of dislocations by deformation (also called cold-working or work hardening) [47].
- Fiber reinforcement – the addition of a fiber, of a material different from the parent material, to improve the mechanical properties of a composite [47].

1.7.2. *Ceramics*

The same mechanisms for strengthening metals, as mentioned above, are available to ceramics; however, their effect is limited due to the atomic bonding of ceramics, or will not work at all. Most ceramics are crystalline but, unlike metals, they do not have close packed planes on which dislocation motion can readily occur. However, there are micro-mechanisms that lead to

improved fracture resistance in modern ceramics such as micro-crack toughening, transformation toughening, ductile phase toughening, fiber toughening, and whisker toughening [48].

- Micro-crack toughening – the formation of small cracks that allow the release of strain energy which results in an increase in compliance [47].
- Transformation toughening – energy dissipation through a stress-induced martensitic transformation that results in shear deformation and volume change [48].
- Ductile phase toughening – alloying a ceramic with ductile materials. The ductile materials can experience plastic deformation, which dissipates crack energy and causes crack blunting [48].
- Fiber and whisker toughening – for ceramics, a brittle ceramic fiber (whisker) is added to another brittle ceramic to improve toughness. The secret to the high toughness of ceramic composites lies in the bond between the matrix and the fibers (whiskers). [48].

1.8. Spark Plasma Sintering

1.8.1. Theory

Spark plasma sintering (SPS) also known as pulsed electric current sintering (PECS) or electric field assisted sintering (EFAS) is a sintering process by which DC electric current is passed through a graphite die and punch (Figure 8) causing resistive (Joule) heating that provides the energy for sintering to occur. Pressure is applied to the graphite plungers which aids in the densification process. Joule heating has been found to play a dominant role in the densification of powder compacts, which results in achieving near theoretical density at lower temperatures as compared to conventional sintering techniques. SPS occurs in a vacuum, a chemically inert environment, which prevents chemical reactions with the atmosphere which can alter experimental results. However, since graphite tooling is typically used, it is also a reducing environment, which can be of major concern for sintering oxide ceramics and metals.

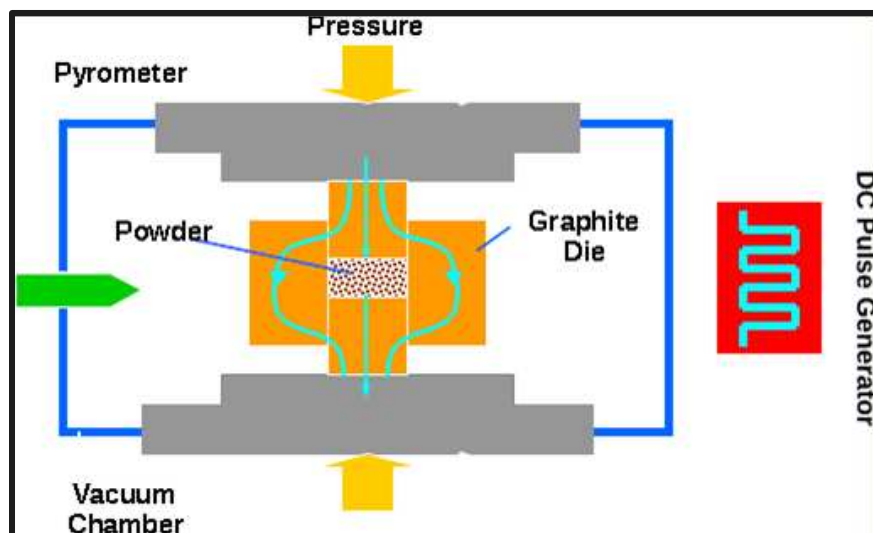


Figure 8: SPS process

The heat generation is internal, in contrast to the conventional hot pressing, where the heat is provided by external heating elements. This facilitates a very high heating or cooling rate (up to 1000 K/min) hence the sintering process generally is very fast (within a few minutes). The general speed of the process ensures it has the potential of densifying powders with nanometric sized features while avoiding coarsening which accompanies standard densification through various diffusion mechanisms [49] (Figure 9). The fast heating rates of SPS have been shown to be an excellent method for preparing ceramics with enhanced piezoelectric [50], thermoelectric [51], optical [52], or biomedical [41] properties.

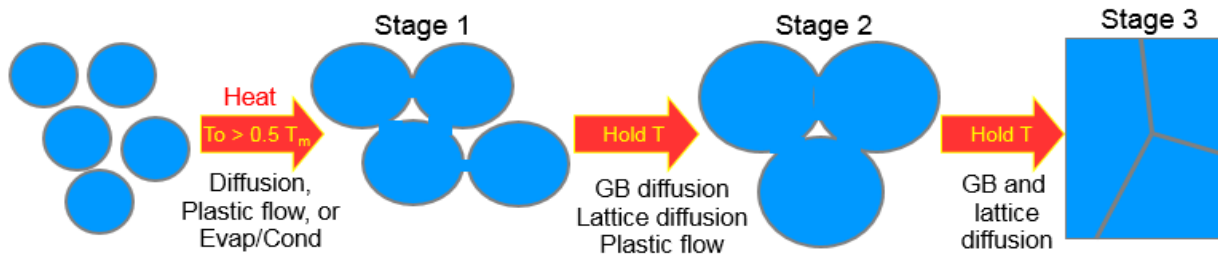


Figure 9: Particle sintering and diffusion

SPS utilizes applied pressure to assist in densification. Densification is enhanced by the application of pressure due to: increase initial particle packing, increase plastic flow of particles at elevated temperature, and creep of the porous compact. Another key factor for the enhanced densification is stress amplification at pores. Compressed particles have increased stress intensity at the point of contact, when the contacts are small the effective stress at these contacts is very high. The effective pressure increases with decreasing particle size and decreases to the applied pressure at full density [53]. Pressure assisted sintering is particularly important during the manufacture of ceramic matrix composites where the reinforcing phase can severely limit the

sintering of the powder matrix [54]. For the reasons mentioned above SPS is ideal for creating nanometric HA ceramic matrix composites.

1.8.2. Tooling

All powders are densified using a Dr. Sinter spark plasma sintering machine manufactured by the Sumitomo Coal Mining Company. All samples are densified using graphite dies, plungers, a graphite – foil sleeve, and graphite – foil plunger faces (Figure 10). The graphite – foil was used as a lubricating and buffer layer between the plunger and inner die wall as well as the plunger faces to prolong the life of the die and plunger. A hole for a Type K thermocouple was drilled radially into the dies 3 mm away from the sample.

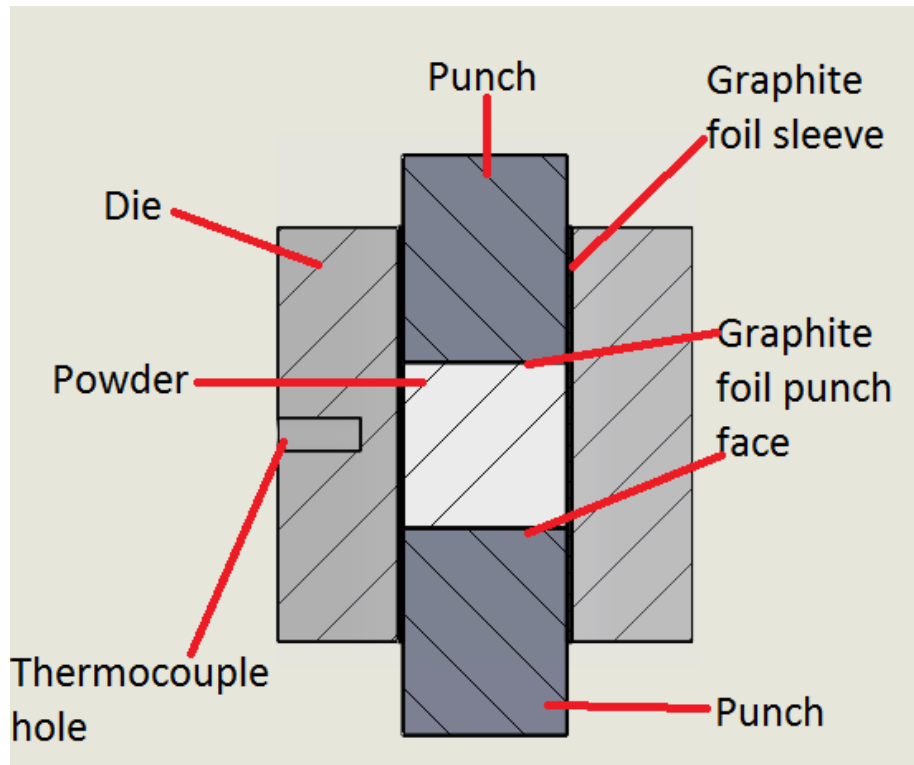


Figure 10: Standard SPS tooling geometry for this study

HA powder tooling geometry:

- Dies: 50 mm tall, 50 mm outer diameter, 20 mm inner diameter.

- Punches: 30 mm tall, and 19.8 mm diameter.

HABNNP tooling geometry:

- Dies: 50 mm tall, 50 mm outer diameter, 20.2mm inner diameter.
- Punches: 30 mm tall, and 19.8 mm diameter.

1.9. Powder Preparation

HA powders (40 nm, 98% purity, Skyspring Nanomaterials, Houston, Texas) were calcined in air at 500 °C for 1 hour, furnace cooled, and desiccated before use. BNNP (100 nm, 99.5% purity, Skyspring Nanomaterials, Houston, Texas) were dispersed in lab grade ethanol using an ultrasonication wand (MSK – USP – 3N, MTI Corporation, Richmond, California) with a 33% duty cycle at 50% power for 30 minutes before mixing in the appropriate amount of HA powders to obtain the appropriate mass fraction. The mixture was then mixed using the same ultrasonication wand for an additional 60 minutes using the same duty cycle. The composite powders were dried at 70 °C, to prevent boiling, on a hot plate for several days. A magnetic stir bar was used and set to 350 rpm to prevent the mixture from settling and/or separating. After drying the composite powders were calcined and desiccated similar to the neat HA powders. Powders were densified using a Dr. Sinter spark plasma sintering machine (SPS, 8000A system, Sumitomo Coal Mining Company Ltd, Tokyo, Japan) using graphite tooling (AR14, Ohio Carbon Blank, Willoughby, Ohio).

1.10. Densification Parameters

HA powders were densified under the following conditions and can be seen below in Figure 11.

1. 0 – 200 °C in 5 minutes
2. 200 °C hold for 2 minutes to allow outgassing of powders
3. 200 – 900 °C in 7 minutes (100 °C/min)

4. 900 °C hold for 15 minutes
5. 8 kN load (25.5 MPa) was applied throughout entirety of experiment.

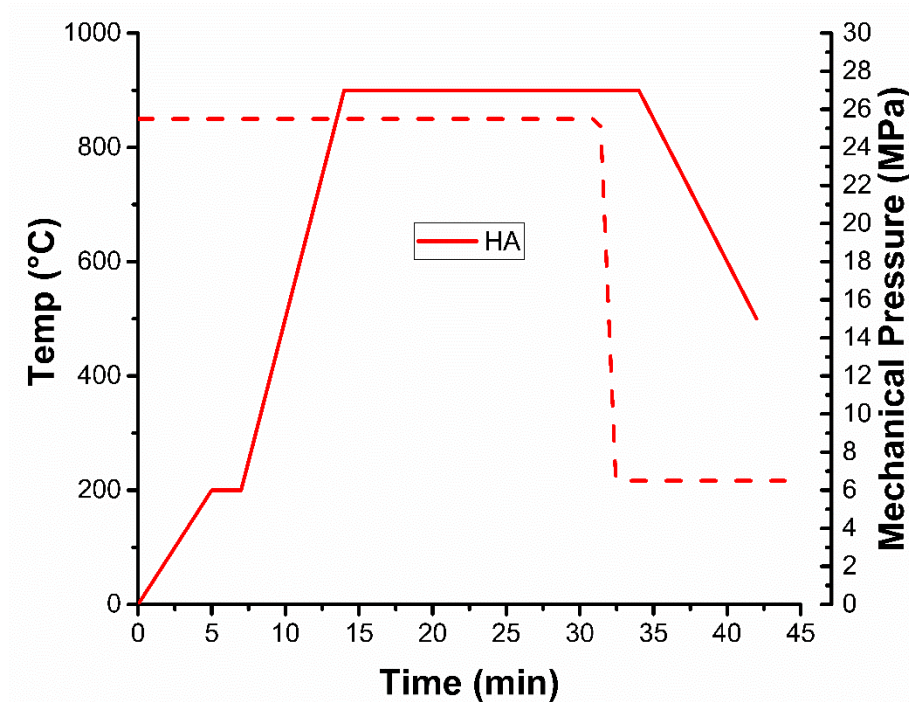


Figure 11: HA sintering parameters

Composite powders were densified under the following conditions and can be seen below in Figure 12.

1. 0 – 200 °C in 5 minutes
2. 200 °C hold for 2 minutes to allow outgassing of powders
3. 200 – 900 °C in 7 minutes (~100 °C/min)
4. 900 °C hold for varying times
5. 8 kN load (25.5 MPa) during 200 °C isothermal hold and increased 24.6 kN (80 MPa) at 600 °C and released at 800 °C during cool down.

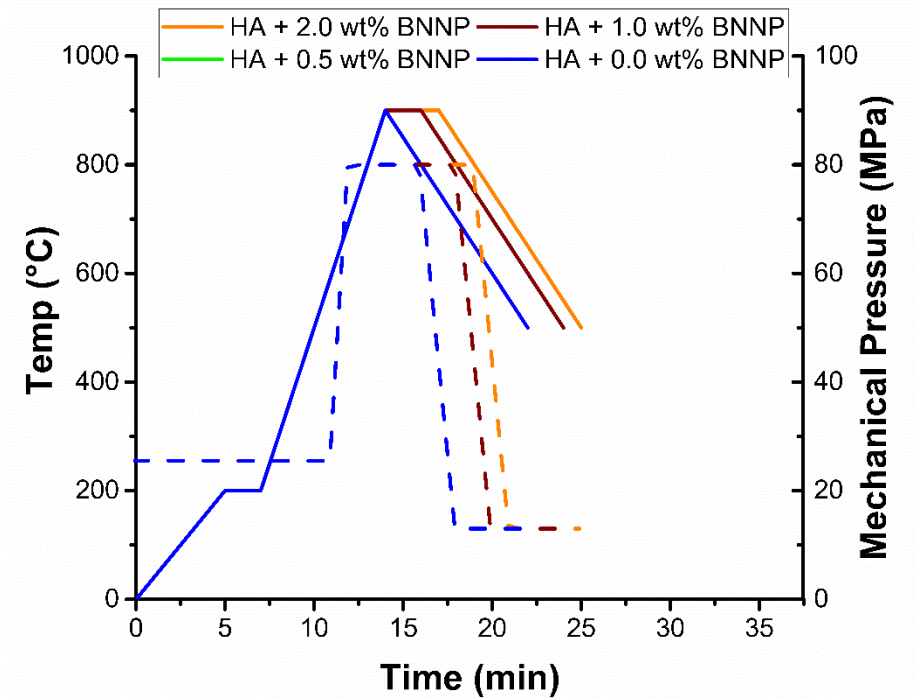


Figure 12: HA BNNP sintering parameters

Sintering parameters for composite powders were obtained using the Taguchi Design of Experiments Method and are discussed below.

1.11. Sample preparation for mechanical testing

For mechanical testing samples were cut into rectangular sections (3 x 3 x 18 mm) using a low diamond content slow speed (Isomet, Buehler, Lake Bluff, Illinois) wafering blade (5" x 0.015" x 1/2" Medium grit, high conc. DIAMAT Wafering Blade, Pace Technologies, Tucson, Arizona).

The slow speed avoids microstructural changes due to heat produced at fast speeds. Samples were sectioned by adhering the cylindrical puck to a sacrificial graphite backing and mounted into the chuck of the Isomet saw (Figure 13).

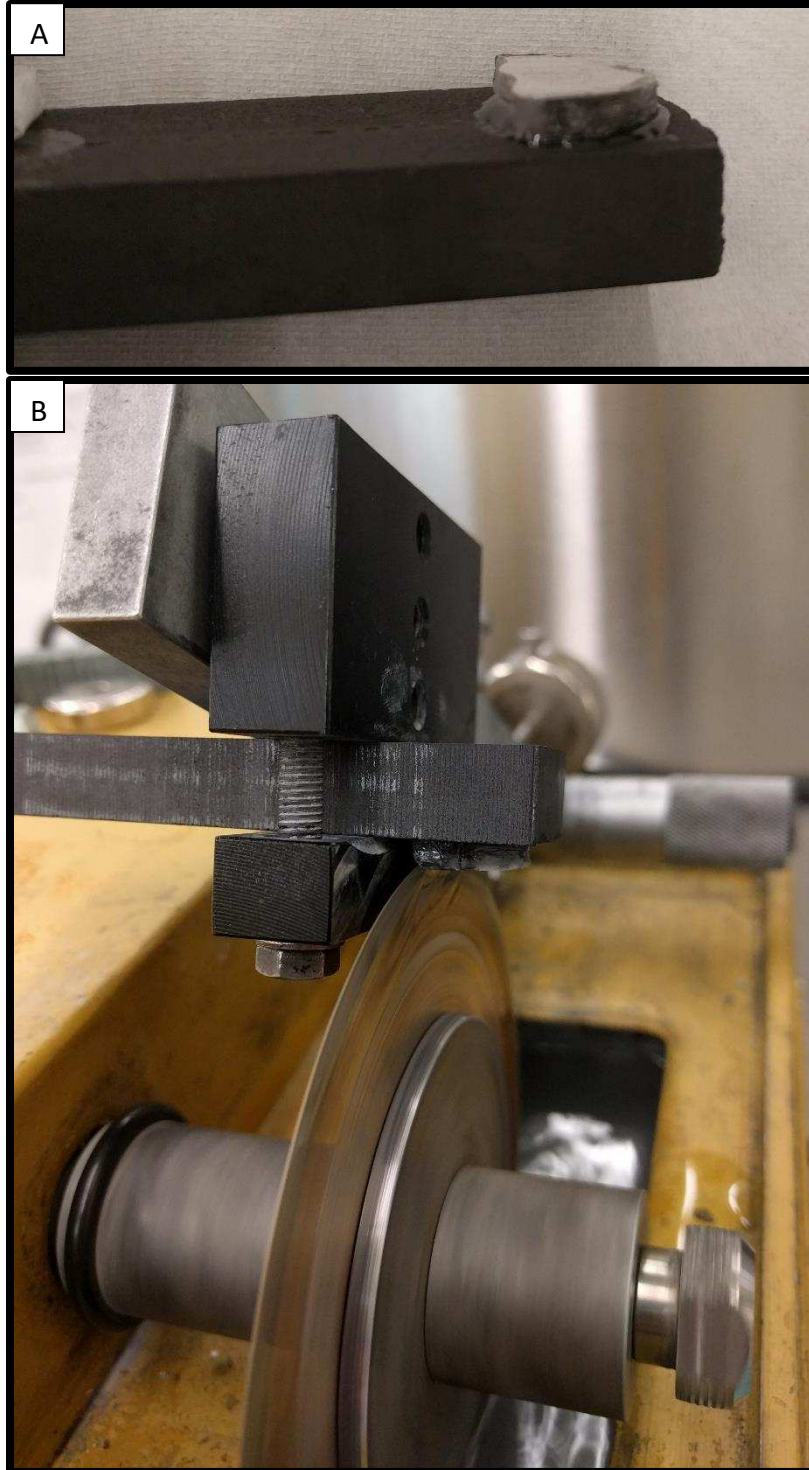


Figure 13: A) Sample mounted to sacrificial graphite backing, B) Sacrificial graphite backing mounted in chuck of Isomet during sample sectioning procedure

The sintered samples were made as 19.8 mm pucks and sectioned into two beam samples and two hardness samples. Figure 14 shows the geometry for cutting samples, where R is the radius of the sample, r is the height to the chord length a from the center of the sample, h is the distance between the chord length a and the edge of the specimen, and s is the arc length that extends between the intersections of R and a . Prior to cutting r was determined by equating the chord length a to 18, which maximizes the cross sectional area of the tested beam, while producing a specimen whose round edges are outside of the 16mm span of the 4 – pt. bend tester.

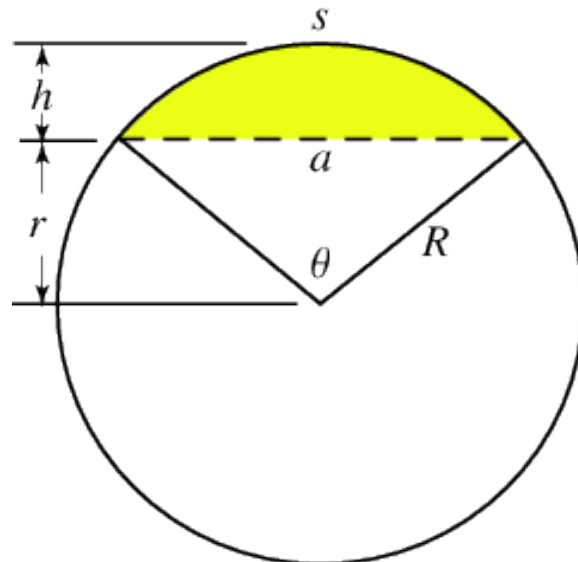


Figure 14: Sample cutting geometry

Samples were ground using 200, 400, 800, grit silicon – carbide abrasive papers (Pace Technologies, Tuscon, Arizona) and then polished using 6, 3, and 1 micron polishing media (DIAMAT PC High Viscosity Diamond Suspension, Pace Technologies, Tuscon, Arizona) to remove surface defects from cutting/processing that could dominate mechanical behavior during testing.

1.12. Mechanical Testing

1.12.1. Single Edge V Notch Testing (SEVNB)

The fracture toughness in flexure was calculated per the method detailed in ASTM STP 1409 [55] using Eqns. 6 and 7.

$$K_{1c} = \frac{F}{B\sqrt{W}} \frac{S_1 - S_2}{W} \frac{2\sqrt{\alpha}}{2(1-\alpha)^{1.5}} Y^* \quad (6)$$

$$Y^* = 1.9887 - 1.326\alpha - (3.49 - 0.68\alpha + 1.35\alpha^2)\alpha(1 - \alpha)(1 + \alpha)^{-2} \quad (7)$$

Where F is the load at fracture, S1 is the outer span length, S2 is the inner span length, B is the specimen width, W is the specimen height, a is the notch depth, α is a/W, and Y* is the stress intensity shape factor.

Cracks were prepared per STP1409 as demonstrated in Figure 15 [55]. The notch was initially made using a diamond blade and sharpened by dipping a razor blade in 1-micron diamond polishing media (Pace Technologies, DIAMAT PC High Viscosity Diamond Suspension, Tuscon, Arizona). The notch was made using an in-house jig (Figure 16).

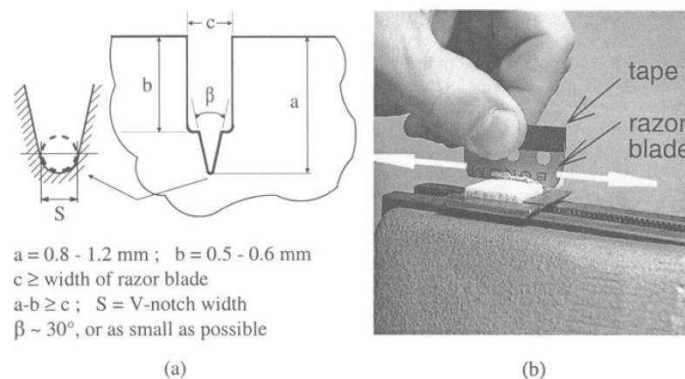


Figure 15: (a) notch geometry criteria and (b) notch tip sharpening [55]

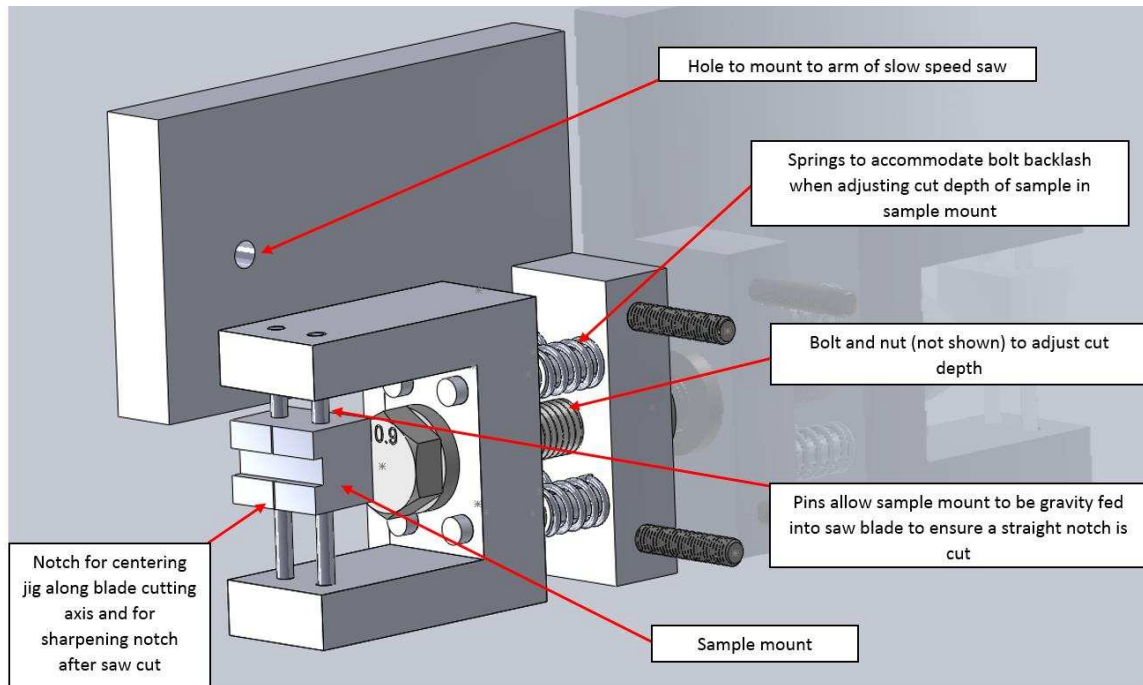


Figure 16: Saw mounted notch jig for SEVNB testing

1.12.2. Vickers Hardness Testing

Samples tested using the indentation hardness method will be tested using a standard Vickers indenter per ASTM C1421-10 [56]. Vickers indentation is the standard hardness testing procedure for hard or brittle materials. The applied load was 1 kilo - grams-force with a 15 second dwell time. The hardness can be used to compute the fracture toughness through empirically derived equations presented in [56]. Hardness measurements were taken using an HV – 1000Z Microhardness Tester (Pace Technologies, Tuscon, Arizona) with a standard Vickers Tip. Hardness was computed using Equation 8.

$$H_V = 1.8544 \frac{P}{D^2} \quad (9)$$

Where P is the applied load in kilograms – force and D is the diagonal length in millimeters as shown in Figure 17.

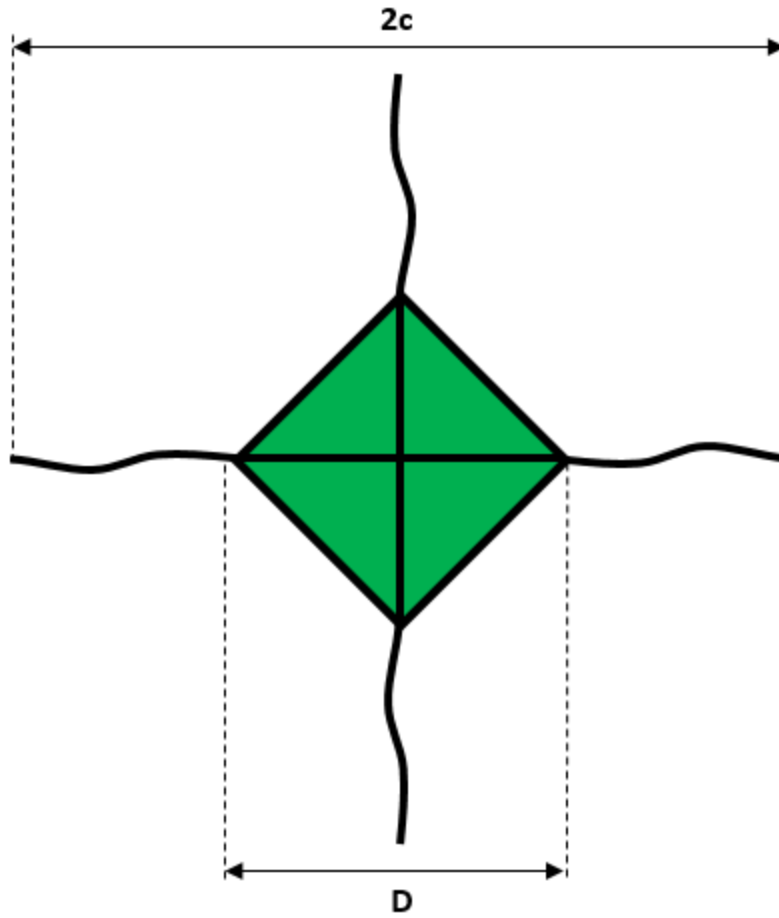


Figure 17: Crack measurement from Vickers indentation

Samples were polished on both sides and placed on an epoxy puck that had been ground flat on both sides (Figure 18) during indentation.



Figure 18: Sample mounted on an epoxy puck during hardness test

1.12.3. *Vickers Indentation Fracture (VIF)*

The fracture toughness measured by the VIF method was computed using the equations derived by Anstis et al [57] in Eq. 9.

$$K_{1c} = 0.016 \left(\frac{E}{HV} \right)^{1/2} \frac{P}{c^{3/2}} \quad (9)$$

Where E is the Young's modulus of the matrix material, HV is the Vickers hardness, P is the applied load, and C is the length of the crack induced by the tip of the indenter, shown schematically in Figure 17. VIF cracks were imaged using optical microscopy (OM) with a 12

wt% level 1 dye penetrant (SKL – SP2, Zoro Industrial Supplies) diluted in acetone to enhance crack contrast, similar to the method developed at AIST Japan [58]. VIF cracks were also imaged using SEM in backscatter electron detection mode where crack contrast was greatly enhanced as compared to secondary electron detection mode.

1.12.4. Flexural Testing

Flexural strength in 4 point bending was computed per ASTM C1161 [56] using Eq. 10.

$$S = \frac{3PL}{bd^2} \quad (10)$$

Where S is the flexural strength of the composite, P is the force at rupture, L is the distance between outer supports, b is the specimen width, and d is the specimen thickness. Flexural tests were performed on in house made bend tester and precision alignment tool (Figure 19).

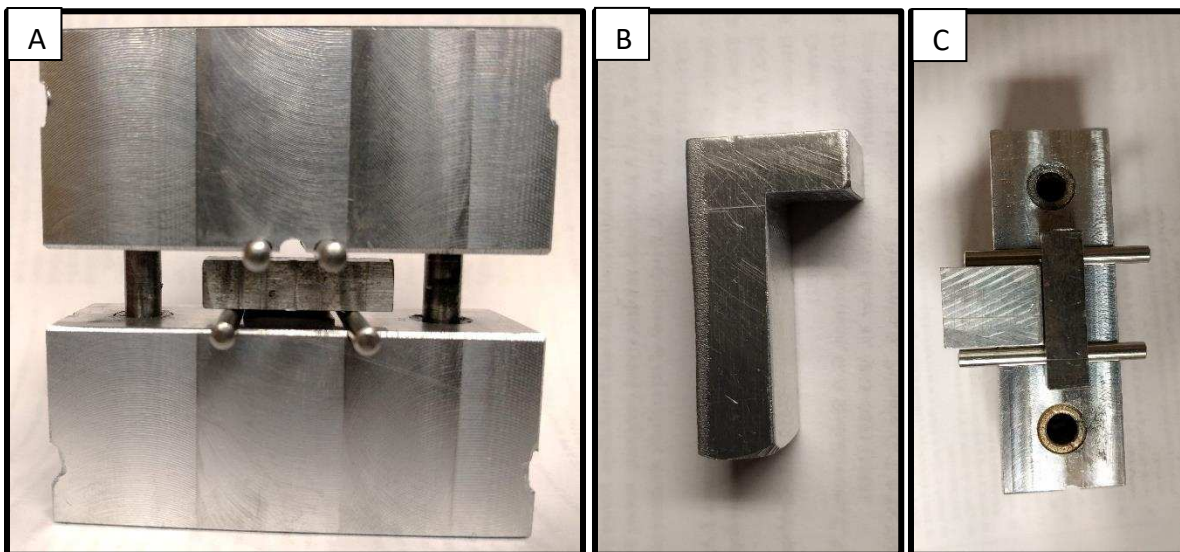


Figure 19: A) Hybrid 3-4-point bend tester with calibration beam, B) precision alignment tool, C) precision alignment tool shown aligning beam. The distance between the bottom two pins in A is 16mm, while the distance between the top two pins is 8mm.

1.13. Grain Size Analysis

Polished samples were thermally etched in air at 700 °C for 4 hours, coated with 5 nm of gold, observed in SEM, and the grain size was computed using Abram's 3 – circle method as outlined in ASTM E – 112 [59].

1.14. Experimental Shortcomings

The SEVNB method only allows one recording of the fracture toughness per test. This allows one average grain size to be compared to the recorded fracture toughness. The indentation fracture toughness method allows several hardness measurements to be taken, an average computed, then related to the fracture toughness as a function of grain size via standard equations. This allows more information about the material to be extracted through a single set of tests. However, the indentation fracture toughness has been scrutinized because it creates a three-dimensional network of cracks that are stopped after short distances as opposed to rapid crack propagation as seen in the SCF method [60].

1.15. Taguchi Design of Experiments

To determine optimum sintering parameters for the HA BNNP composite powders the Taguchi Design of Experiments (DOE) was combined with SPS sintering. The Taguchi method was used chosen over full and fractional factorial methods because it is economical approach that requires fewer experiments than full and fractional factorial methods and the results can be associated with a statistical level of confidence. Hence, this method is more flexible and more versatile than classical DOE techniques. In a SPS parameter optimization study [61], density, hardness, and fracture toughness were used as the response factors to find optimize sintering hold temperature, hold pressure, hold time, and heating rate. Here we used density as our response factor, because decreasing density has been shown to lead to degradation in mechanical properties [62], to

optimize our sintering heating rate, hold temperature, hold time, and hold pressure. Shown below in Table 1 are levels over which the chosen parameters were varied using a standard L9 array. Experimental order was randomized to avoid self-selection and avoid unknown systematic effects that may have affected the final density of sintered specimens.

Table 1: Taguchi DOE of experiments parameters

Experiment #	Independent Variables			
	Pressure (MPa)	Temperature (°C)	Heating Rate (°C/min)	Hold time (min)
9	70	850	50	0
1	70	900	100	10
3	70	950	200	20
6	80	850	100	20
7	80	900	200	0
5	80	950	50	10
4	90	850	200	10
8	90	900	50	20
2	90	950	100	0

1.16. Weibull Analysis

Experience has shown that a normal (Gaussian) distribution of property values for a ductile material yields a reasonably accurate characterization of material behavior; the same cannot be said for the case of brittle materials. Instead, other statistical theories, such as the Weibull analysis, are necessary to account for the variability of strength and the probability of survival of a particular component as a function of its volume and the applied stress [10].

Fracture toughness, flexural strength, and hardness data were analyzed using the Weibull probability density function [63] with Eq. 11.

$$f(x) = \frac{\beta}{x} \left(\frac{x}{\alpha}\right)^{\beta} e^{-\left(\frac{x}{\alpha}\right)^{\beta}} \quad (11)$$

Where x is the property of interest (fracture toughness, flexural strength, hardness, etc), β is the Weibull Shape factor or Weibull Modulus, and α is the Weibull scale parameter. Figure 20 shows a typical Weibull probability distribution function with decreasing values of β . High values of β indicate high reliability and therefore predictable values for the mechanical property of interest, with the accepted cut off for reliability of $\beta = 2$, with higher values being preferred. The scale parameter, α , is a representation of how far on the x -axis the sample will last, where this x axis can be flexural strength, fracture toughness, hardness, etc. Larger scale factors indicate higher strength, fracture toughness, or hardness for this study. This parameter is the value where 63% of sample failures have occurred before this point.

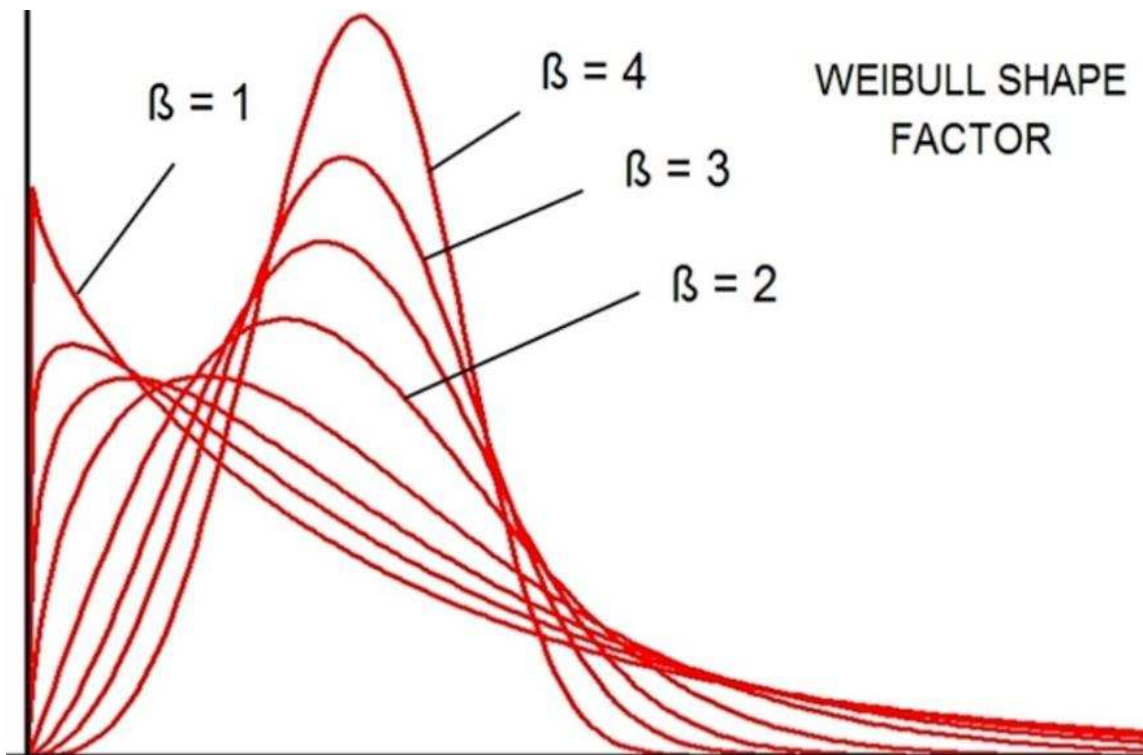


Figure 20: Weibull distribution with decreasing shape factor [64]

The Weibull Cumulative Distribution Function (Eq. 12, Figure 21) was also used to analyze the failure data and to visualize the probability of failure based on the applied stress. In Figure 21, the y-axis represents probability of failure given an x value, where x is flexural strength, fracture toughness, hardness, etc.

$$F(x) = 1 - e^{-\left(\frac{x}{\alpha}\right)^\beta} \quad (12)$$

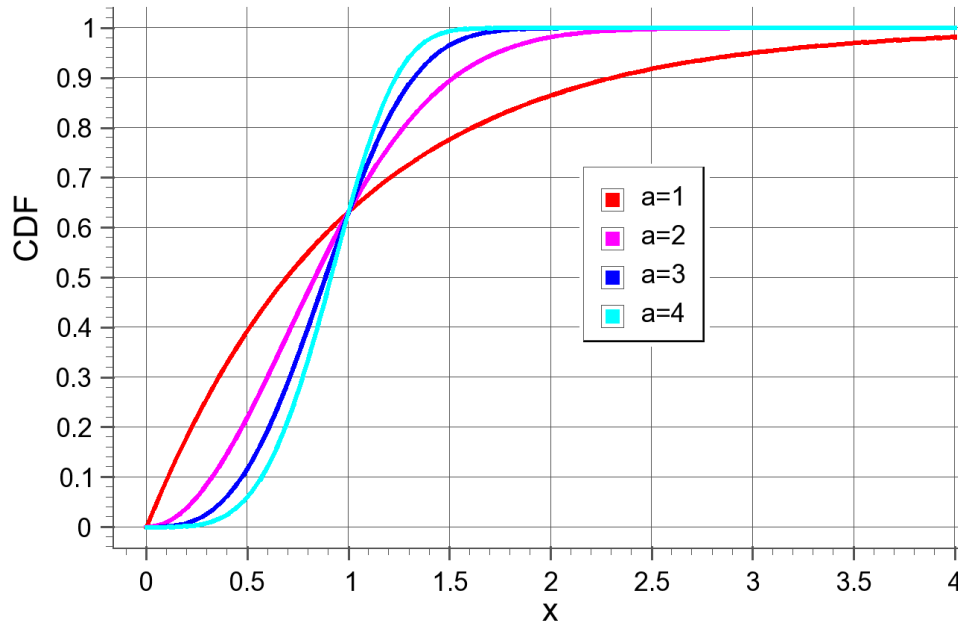


Figure 21: Weibull Cumulative Distribution Function with varying values of alpha[65]

1.17. Characterization

Powders and sintered samples were characterized using X-Ray Diffraction (XRD) and scanning electron microscopy. SEM was used to image fracture surfaces and analyze the grain size of thermally etched samples. Imaged surfaces were evaluated for grain size, porosity, fracture mechanism (transgranular or intergranular), fiber pull-out, and evidence of crack bridging. XRD was used to evaluate the chemical composition of the various samples and provide information about the unit cell.

1.18. American Society for Testing and Materials (ASTM) specifications

The following ASTM specifications will be used to test for the listed properties:

- C1421 – 10 – Standard Test Methods for Determination of Fracture Toughness of Advanced Ceramics at Ambient Temperature
- C1161 – 13 – Standard Test Method for Flexural Strength of Advanced Ceramics at Ambient Temperature
- E112 – 13 – Standard Test Methods for Determining Average Grain Size

CHAPTER 4: RESULTS

1.19. Taguchi Design of Experiments

In Figure 22 the vertical axis for these main effects plots shows the average sample density and the data point for each factor was created by averaging the density for each sample sintered at that particular condition and the horizontal axes correspond to heating rate, hold time, hold pressure, and hold temperature for the four plots. As an example, the samples sintered at 50 °C/min had an average density of 95.72%, the samples sintered at 100 °C/min had an average density of 97.1%, and samples sintered at 200 °C/min had an average density of 91.75%. From Figure 22 the 100 °C/min, 0-minute hold time, 80 MPa hold pressure, and 900 °C hold temperature produced samples with the highest average density for the HA + 0.5wt% BNNP samples. These results were then used to densify the HA and HA + 0.5wt% BNNP samples. For the 1.0 wt% and 2.0 wt% samples the hold time was increased to achieve to full density, due to thermal stability of BNNP causing them to inhibit densification during sintering.

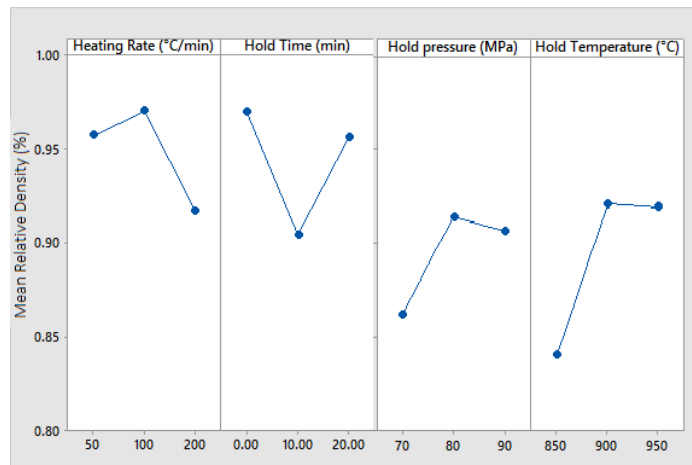


Figure 22: Density Main Effects Plot for heating rate, hold time, hold pressure, and hold temperature

1.20. Characterization

Transparent hydroxyapatite was sintered at 900 °C Figure 23. XRD analysis of post – sintered samples and calcined powders show that significant decomposition did not occur during experimentation Figure 24 and Figure 25. Slight peaking shifting occurred due to hydroxylation but this can be expected [66].



Figure 23: Translucent HA sintered at 900 °C. Sample is 1mm thick and 20 mm in diameter.

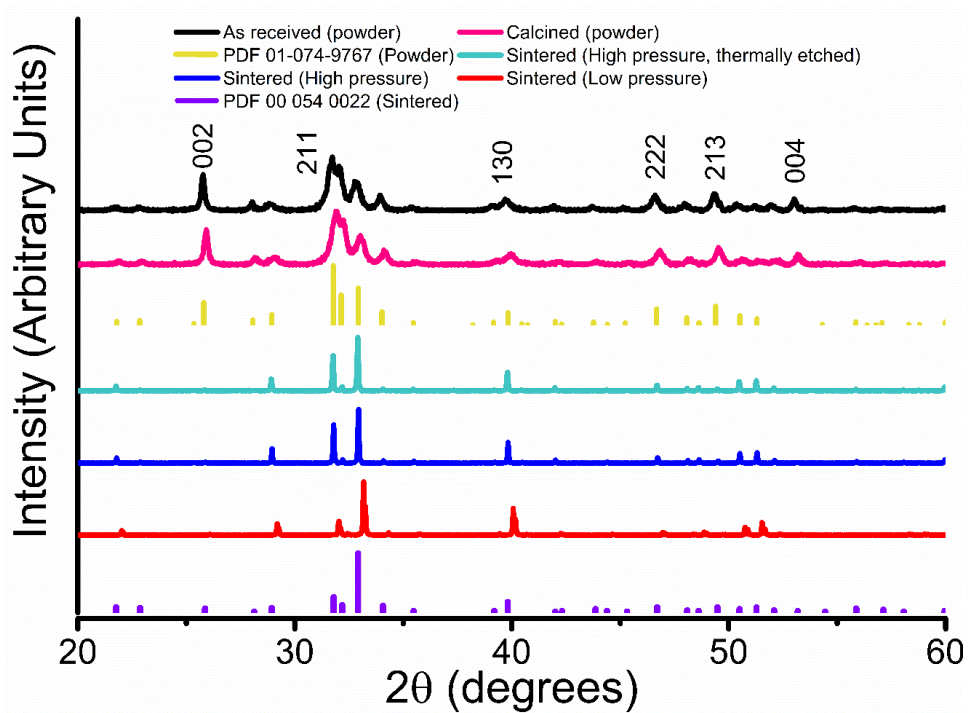


Figure 24: XRD spectra of hydroxyapatite powders and samples

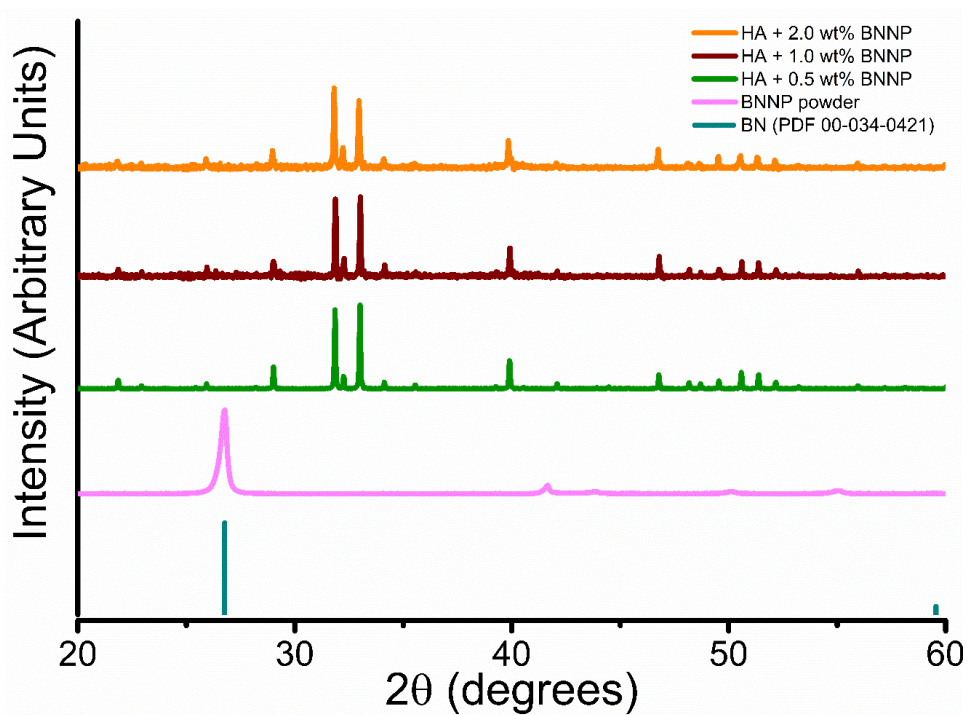
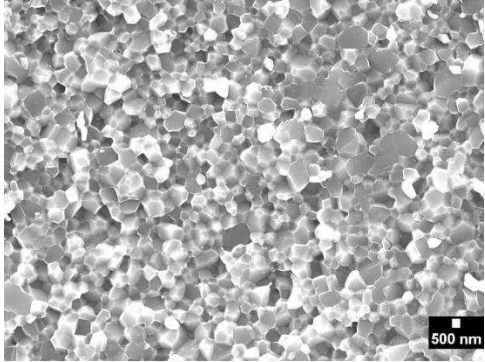
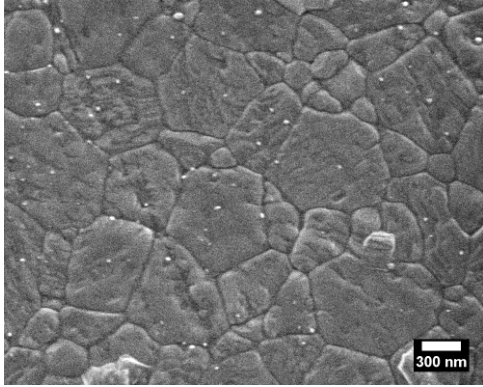
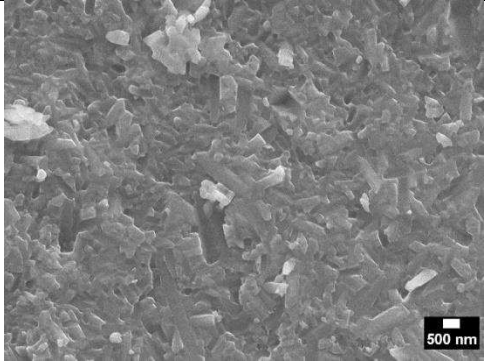
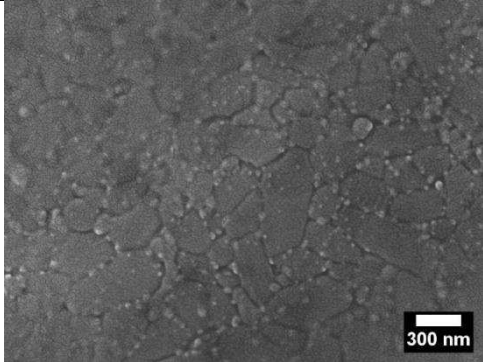
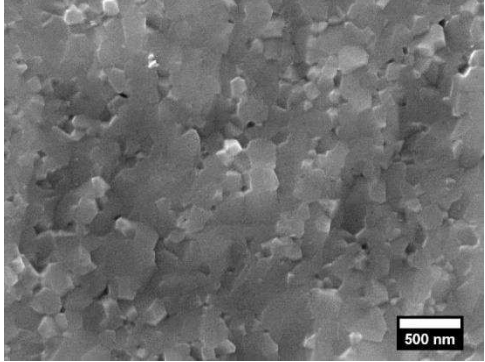
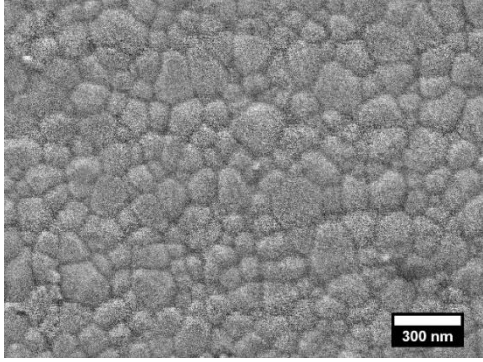


Figure 25: XRD spectra of HA BNNP sintered samples.

1.21. Grain Size and Fracture Surfaces

The grain sizes of HA and HA BNNP composites were evaluated using the Abrams 3 circle method. Grain size and fracture surfaces are shown below in Figure 26 and summarized in Table 2. For these figures and all following figures HA + 0.0 wt% BNNP denotes pure HA sintered at the same conditions as the HA BNNP powders.

	Fracture surfaces	Grain size
HA (low pressure)		
HA + 0.0wt% BNNP		
HA + 0.5wt% BNNP		

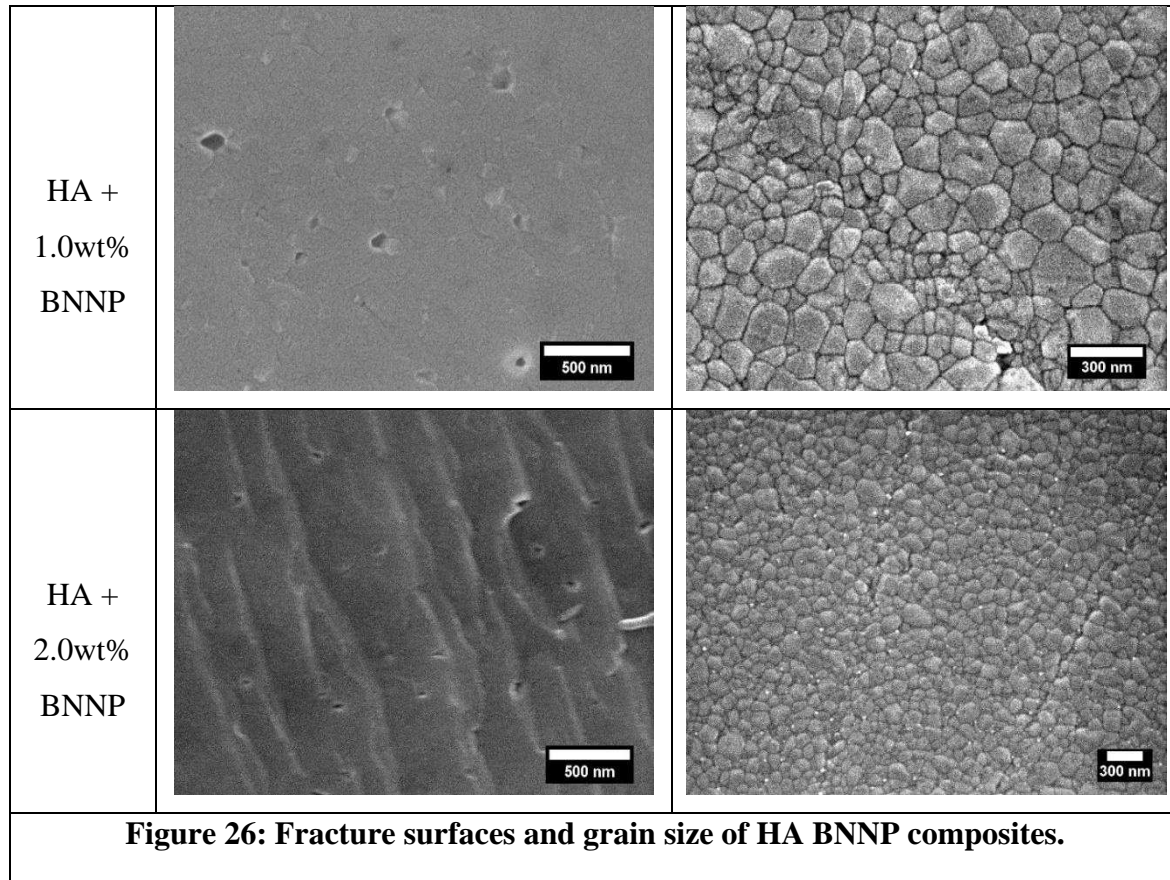


Table 2: HA and HA BNNP Grain sizes

Sample	Grain size (nm)	Primary Fracture Mechanism
HA (low pressure)	1031	Intergranular
HA + 0.0wt% BNNP	630	Transgranular
HA + 0.5wt% BNNP	356	Transgranular
HA + 1.0wt% BNNP	290	Transgranular
HA + 2.0wt% BNNP	261	Transgranular

1.22. Flexural testing: Average and Weibull Distribution

Table 3 summarizes the measured flexural strength of this study and Figure 27 shows the average flexural strength and Weibull distribution for the samples of this study.

Table 3: Average HA and HA BNNP σ_{FS} and literature comparison

Ref.	Material	Avg. σ_{FS} (MPa)	Avg. d_g (nm)	Testing method	Method	Pressure (MPa)	Temp. (°C)
Pres.	HA + 0.0 wt% BNNP	70.96	630	4PB	SPS	80	900
Pres.	HA 0.5 wt% BNNP	71.19	356	4PB	SPS	80	900
Pres.	HA 1.0 wt% BNNP	79.79	290	4PB	SPS	80	900
Pres.	HA 2.0 wt% BNNP	60.64	261	4PB	SPS	80	900
Pres.	HA	80.14	1031	4PB	SPS	25.5	900
[67]	HA	12.3	---	3PB	Furnace	100 or 150 (CIP*)	1100
[67]	HA + 2.5 wt% hBN	22.55	---	3PB	Furnace	100 or 150 (CIP*)	1100
[67]	HA + 5.0 wt% hBN	30.86	---	3PB	Furnace	100 or 150 (CIP*)	1100
[67]	HA + 10.0 wt% hBN	36.22	---	3PB	Furnace	100 or 150 (CIP*)	1100
[68]	HA	69.57	---	BAF ⁺	HIP***	400	950
[69]	HA	61	---	3PB	NIS**	250	1250
[4]	HA	61.89	---	3PB	NIS**	150	1250

* Cold isostatic pressing, ** Non-isothermal sintering, *** Hot isostatic pressing, ⁺ Biaxial flexure

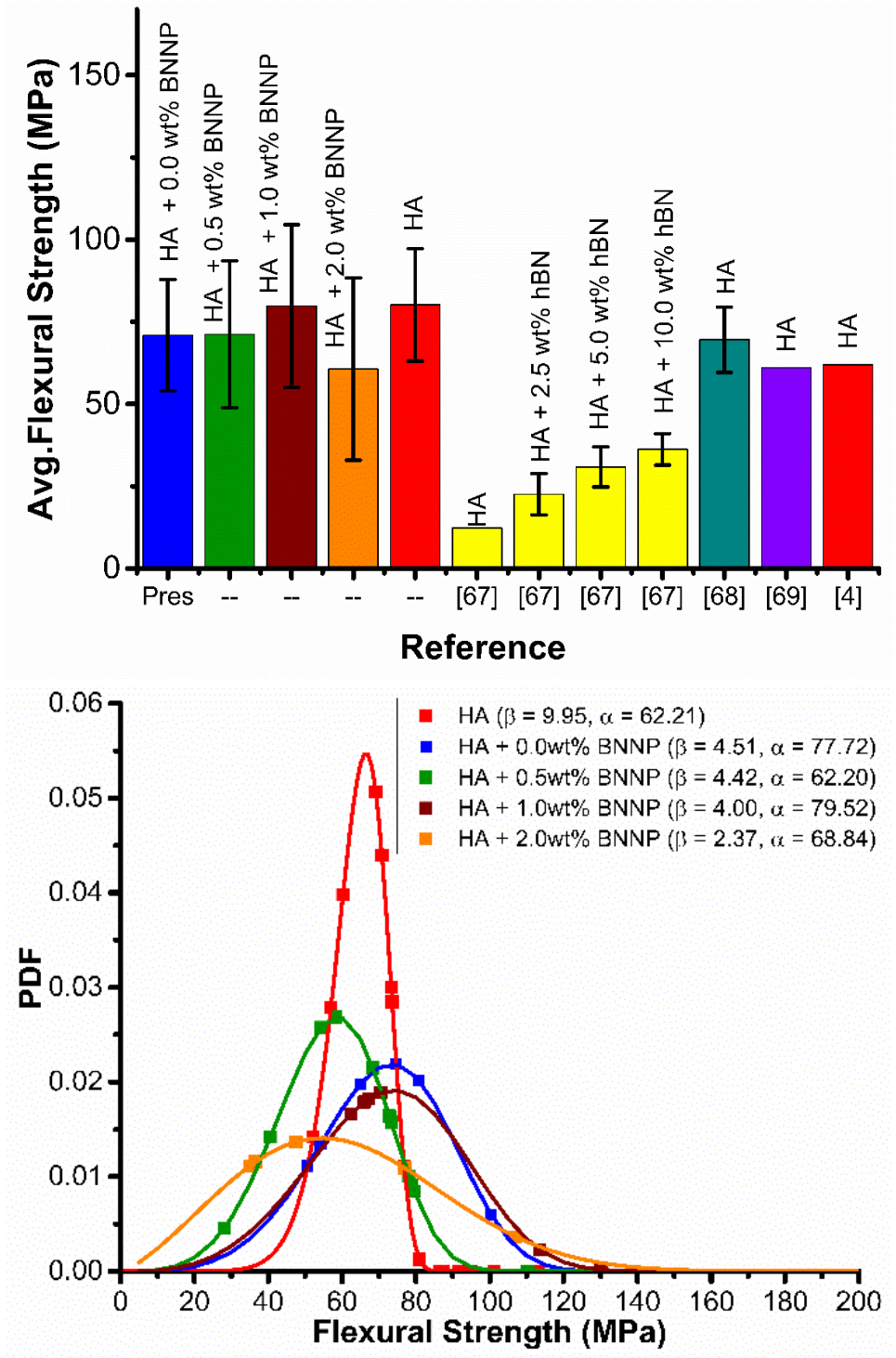


Figure 27: Average flexural strength vs literature and Weibull distribution

1.23. Vickers Hardness testing: Average and Weibull Distribution

Table 4 summarizes the measured Vickers Hardness of this study and Figure 28 shows the average Vickers Hardness and Weibull distribution for the samples of this study.

Table 4: Average HA and HA BNNP HV and literature comparison

Ref.	Material	Avg. HV (MPa)	Avg. d_g (nm)	Method	Pressure (MPa)	Temp. (°C)
Pres.	HA + 0.0 wt% BNNP	5.20	630	SPS	80	900
Pres.	HA + 0.5 wt% BNNP	4.40	356	SPS	80	900
Pres.	HA + 1.0 wt% BNNP	4.90	290	SPS	80	900
Pres.	HA + 2.0 wt% BNNP	3.90	261	SPS	80	900
Pres.	HA	4.54	1031	SPS	25.5	900
[33]	HA	3.16	---	HIP***	160	1150
[33]	HA + 0.5 wt% rGO	3.56	---	HIP***	160	1150
[33]	HA + 1.0wt% rGO	4.17	---	HIP***	160	1150
[33]	HA + 1.5 wt% rGO	3.74	---	HIP***	160	1150
[70]	HA	7.00	600	SPS	60	100
[70]	HA + 4.0 wt% CNT	9.00	600	SPS	60	1100
[28]	HA	6.00	610	SPS	70	1100
[28]	HA + 4.0 wt% BNNT	12.00	170	SPS	70	1100
[71]	HA	3.65	1200	SPS	40	900
[71]	HA + 2.0 wt% hBN	4.00	500	SPS	40	900
[71]	HA + 4.0 wt% hBN	4.37	200	SPS	40	900

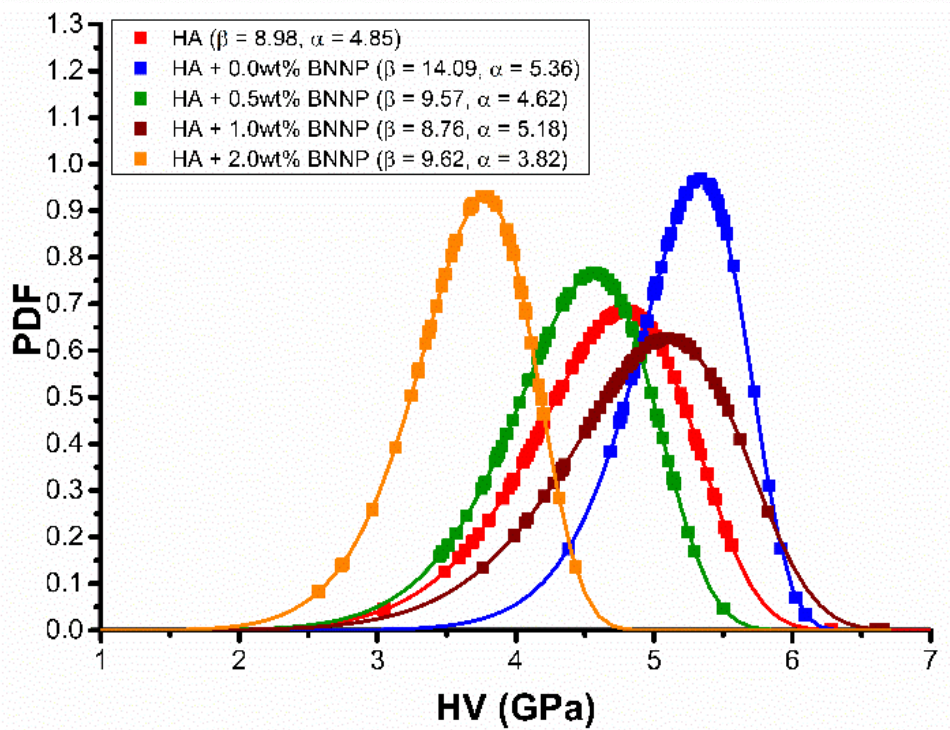
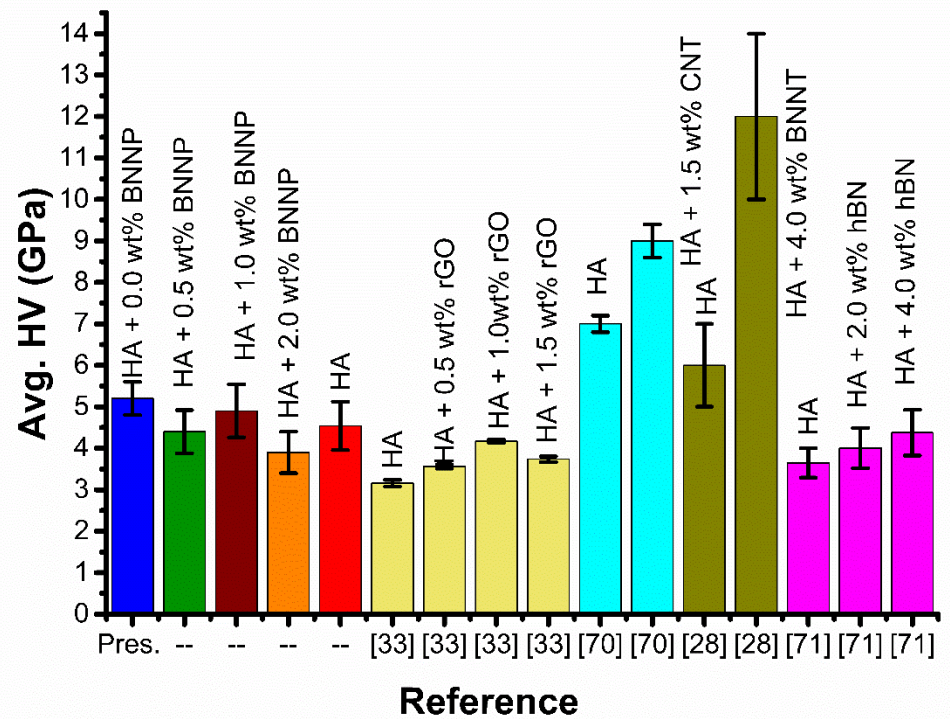


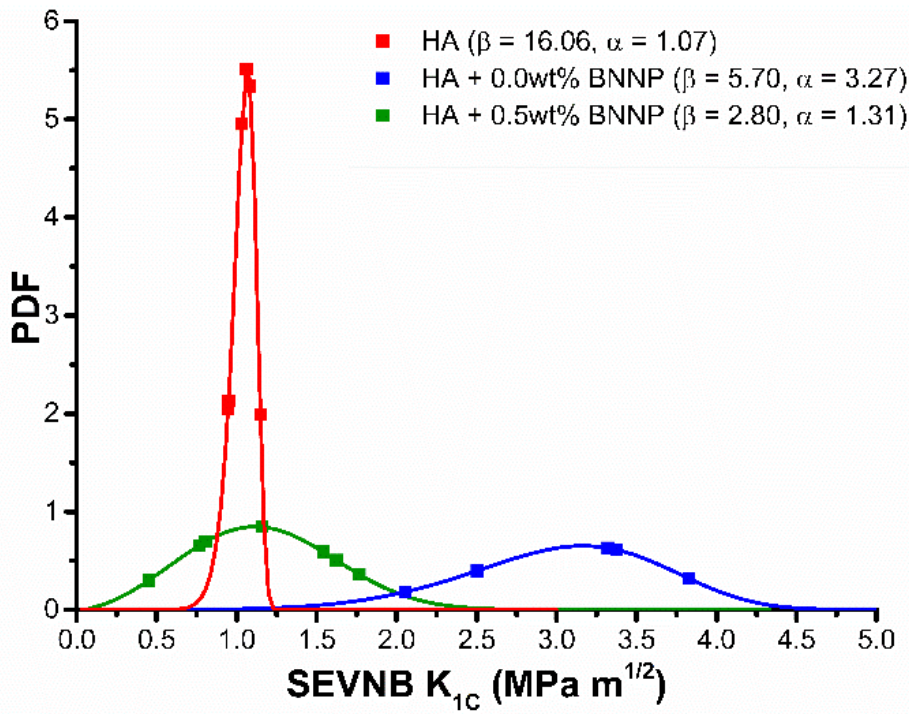
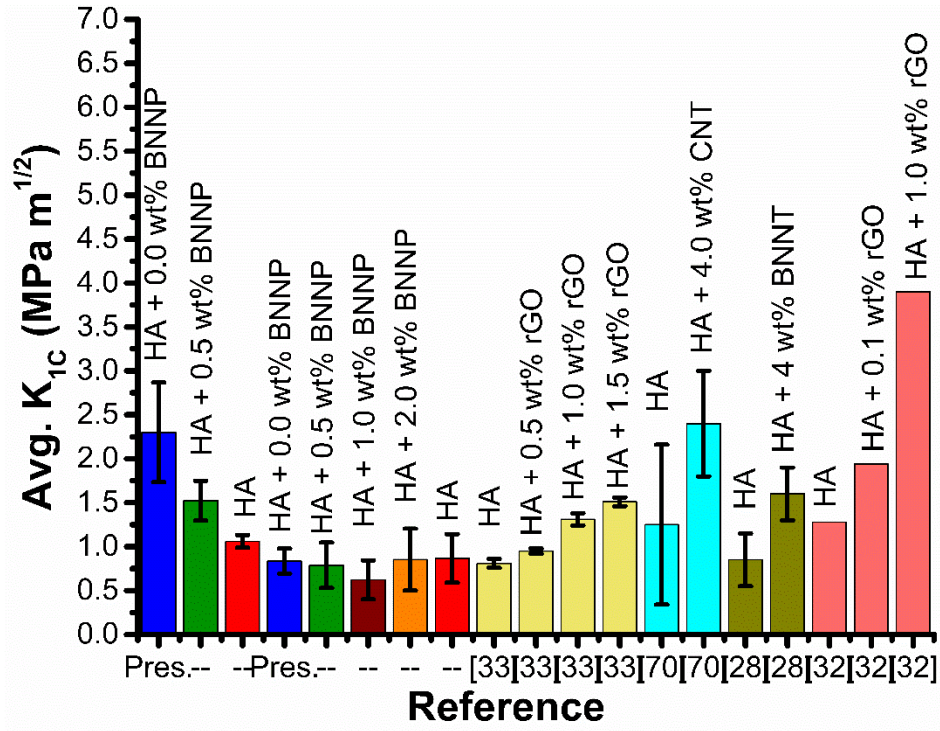
Figure 28: Average Vickers Hardness vs literature and Weibull distribution

1.24. Fracture toughness: Average and Weibull Distribution

Table 5 summarizes the measured fracture toughness and literature comparison. Figure 29 shows average VIF and SEVNB fracture toughness and Figure 30 shows BNNP spanning a VIF crack.

Table 5: Average HA and HA BNNP K_{IC} and literature comparison

Ref.	Material	Avg. K_{IC} (MPa $m^{1/2}$)	Avg. d_g (nm)	Testing method	Method	Pressur e (MPa)	Temp. (°C)
Pres.	HA + 0.0 wt% BNNP	2.30	632	SEVNB	SPS	80	900
Pres.	HA + 0.5 wt% BNNP	1.52	356	SEVNB	SPS	80	900
Pres.	HA	1.06	1031	SEVNB	SPS	25.5	900
Pres.	HA + 0.0 wt% BNNP	0.84	632	VIF, SEM	SPS	80	900
Pres.	HA + 0.5 wt% BNNP	0.79	356	VIF, SEM	SPS	80	900
Pres.	HA + 1.0 wt% BNNP	0.62	290	VIF, SEM	SPS	80	900
Pres.	HA + 2.0 wt% BNNP	0.85	261	VIF, SEM	SPS	80	900
Pres.	HA	0.87	1031	VIF, SEM	SPS	25.5	900
Pres.	HA	1.2	1031	VIF, OM	SPS	25.5	900
[33]	HA	0.81	---	VIF, SEM	HIP	160	1150
[33]	HA + 0.5 wt% rGO	0.95	---	VIF, SEM	HIP	160	1150
[33]	HA + 1.0 wt% rGO	1.31	---	VIF, SEM	HIP	160	1150
[33]	HA + 1.5 wt% rGO	1.51	---	VIF, SEM	HIP	160	1150
[70]	HA	1.25	170	VIF, SEM	SPS	60	100
[70]	HA + 4.0 wt% CNT	2.40	1200	VIF, SEM	SPS	60	1100
[28]	HA	0.85	1500	VIF, SEM	SPS	70	1100
[28]	HA + 4 wt% BNNT	1.60	200	VIF, SEM	SPS	70	1100
[32]	HA	1.28	2000	VIF, SEM	SPS	30	950
[32]	HA + 0.1 wt% rGO	1.94	200	VIF, SEM	SPS	30	950
[32]	HA + 1.0 wt% rGO	3.90	100	VIF, SEM	SPS	30	950



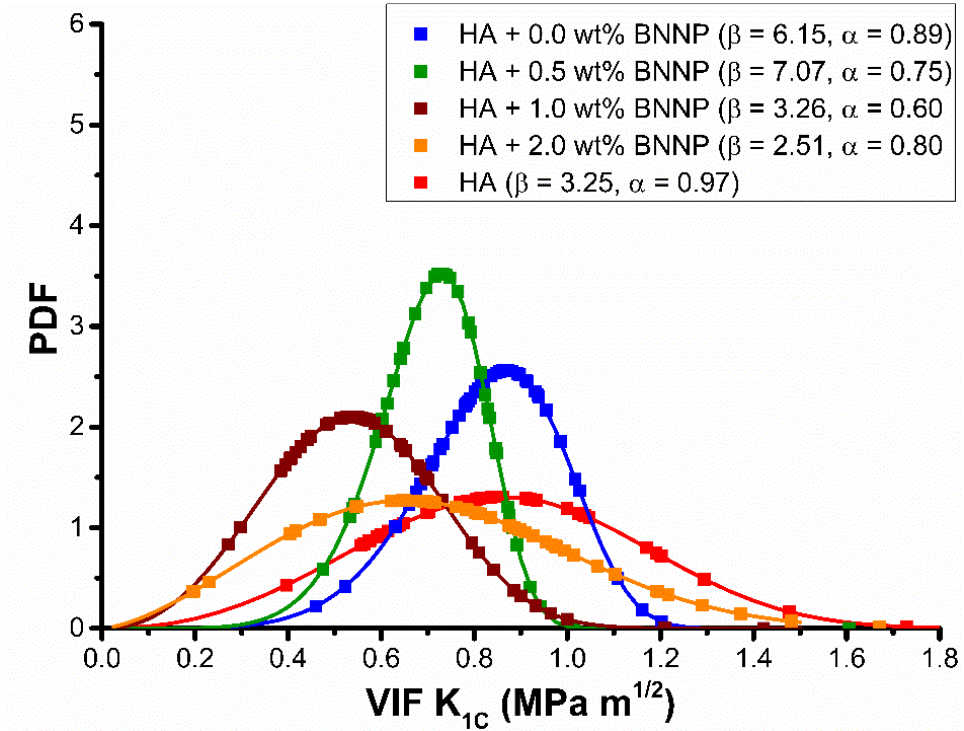


Figure 29 : Average fracture toughness versus literature and Weibull distributions of SEVNB and VIF K_{1C} NOTE: For the SEVNB fracture toughness samples the 1.0 wt% and 2.0wt% BNNP samples were extremely brittle and did live through the notch sharpening process.

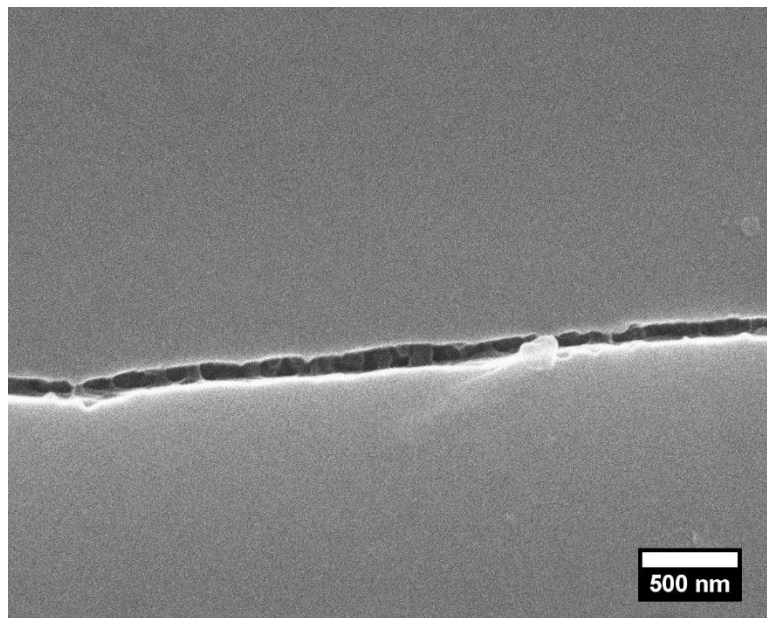


Figure 30: BNNP spanning VIF crack

1.25. Summary of Nanoplatelet effect on Weibull Distribution

Figure 31 shows the effect on the Weibull Modulus with increasing BNNP content for all mechanical tests of this study and the Weibull Scale Parameter is compared to the averages in Table 6.

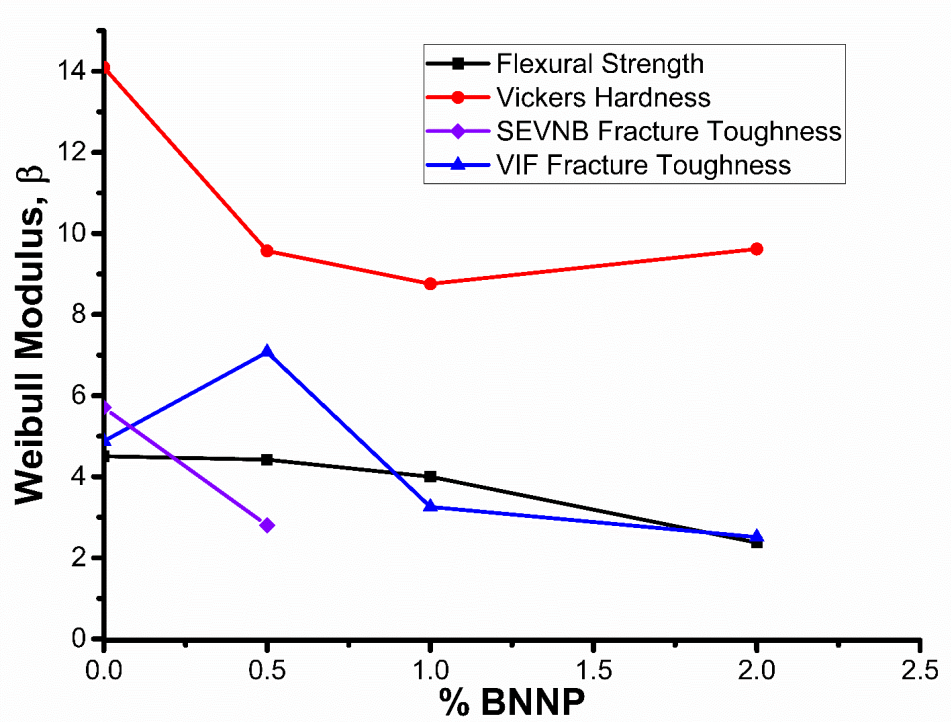


Figure 31: Change in Weibull Modulus versus BNNP content

Table 6: HA and HA BNNP Scale Factor and Average Comparison

Material	Avg. σ_{FS} (MPa)	Scale factor, α (MPa)	Avg. HV (GPa)	Scale factor, α (GPa)	Avg. VIF K_{IC} (MPa m^{1/2})	Scale factor, α (MPa m^{1/2})	Avg. SEVNB K_{IC} (MPa m^{1/2})	Scale factor, α (MPa m^{1/2})
HA + 0.0 wt% BNNP	70.96	77.72	5.20	5.36	0.84	0.89	2.30	3.27
HA + 0.5 wt% BNNP	71.19	62.2	4.40	4.62	0.79	0.75	1.52	1.31
HA + 1.0 wt% BNNP	79.79	79.52	4.90	5.18	0.62	0.60	NA	NA
HA + 2.0 wt% BNNP	60.64	68.84	3.90	3.82	0.85	0.80	NA	NA
HA	80.14	62.21	4.54	4.85	0.87	0.97	1.06	1.07

CHAPTER 5: DISCUSSION

1.26. Effect of tooling

During densification of the HA – BNNP powders it was discovered that the use of two graphite foil layers aided in removal of samples from the die. To accommodate, the addition of a second layer of foil the die ID had to be expanded. The ID was initially expanded using abrasive paper attached to stiff rod and rolled, as opposed to using the appropriate size tooling to create a uniform ID. It was later noticed that this method caused inconsistencies in experimentation. Upon further analysis, it was rationalized that there were several reasons that these inconsistencies could have occurred.

1.26.1. Potential Issues

During ID expansion, uneven pressure or a slight angle could lead to conical shape as demonstrated in Figure 32 and Figure 33, respectively.

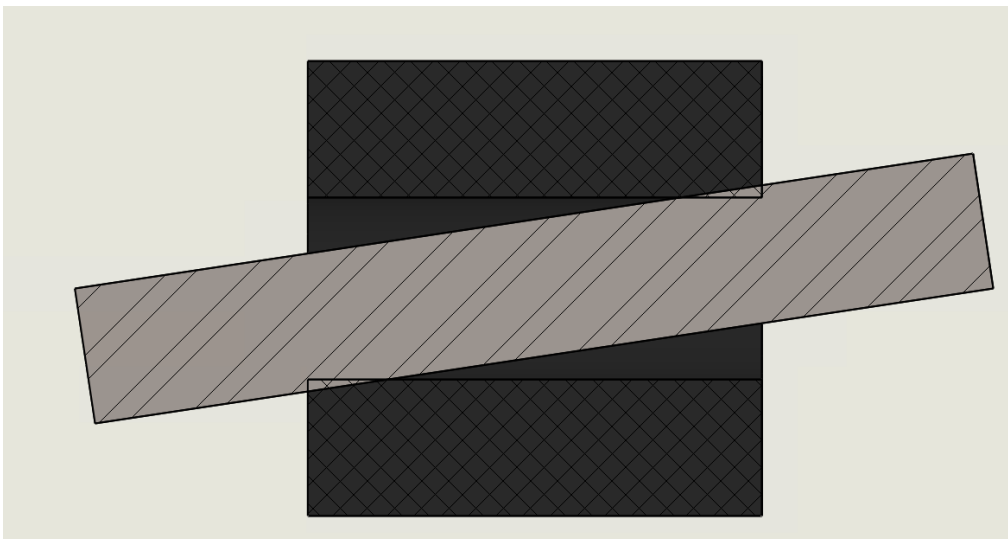


Figure 32: Die bore expansion. This image can be viewed as: A) top view where the rod is angled in the x - plane or B) a side view where uneven pressure is applied to the ends of the rod resulting in the rod being angled in the x – plane.

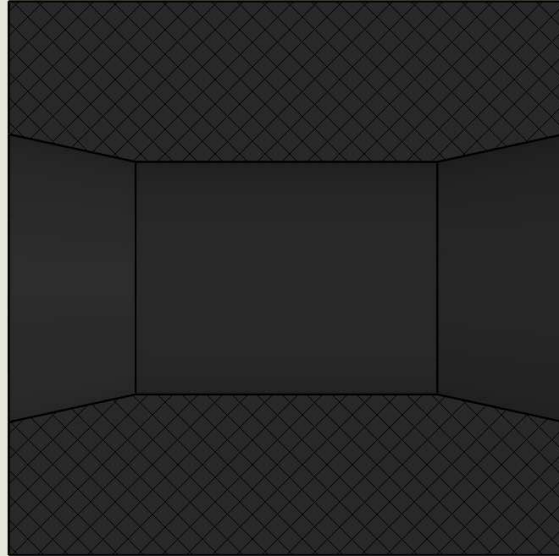


Figure 33: Conical die interior

This would result in a loaded die configuration shown in Figure 34.

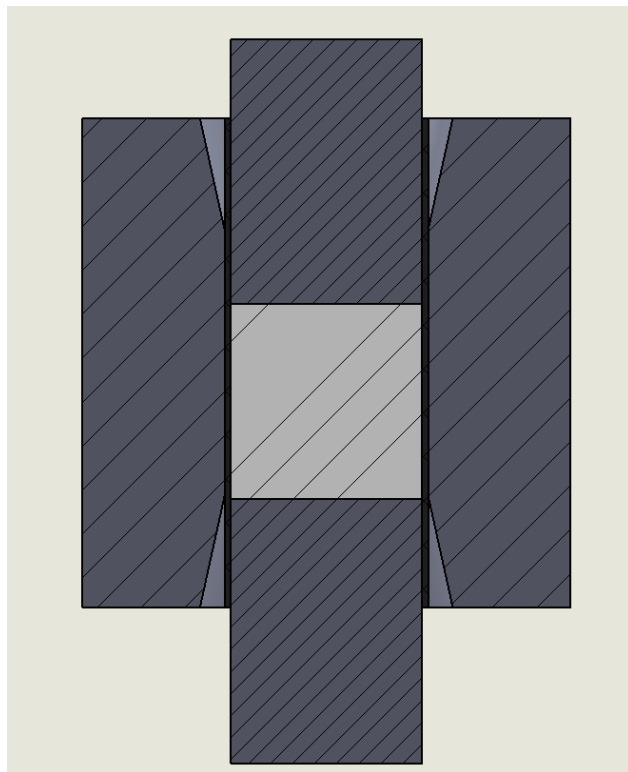


Figure 34: Cross section of plungers, graphite foil, powder, and die with conical interior

This configuration could lead to several issues such as minimal contact between the punch, graphite foil, and the die, torn graphite foil, or the punch becoming cockeyed in the die Figure 35. All of which would lead to decreased conductive pathways and therefore an increase in local temperature.

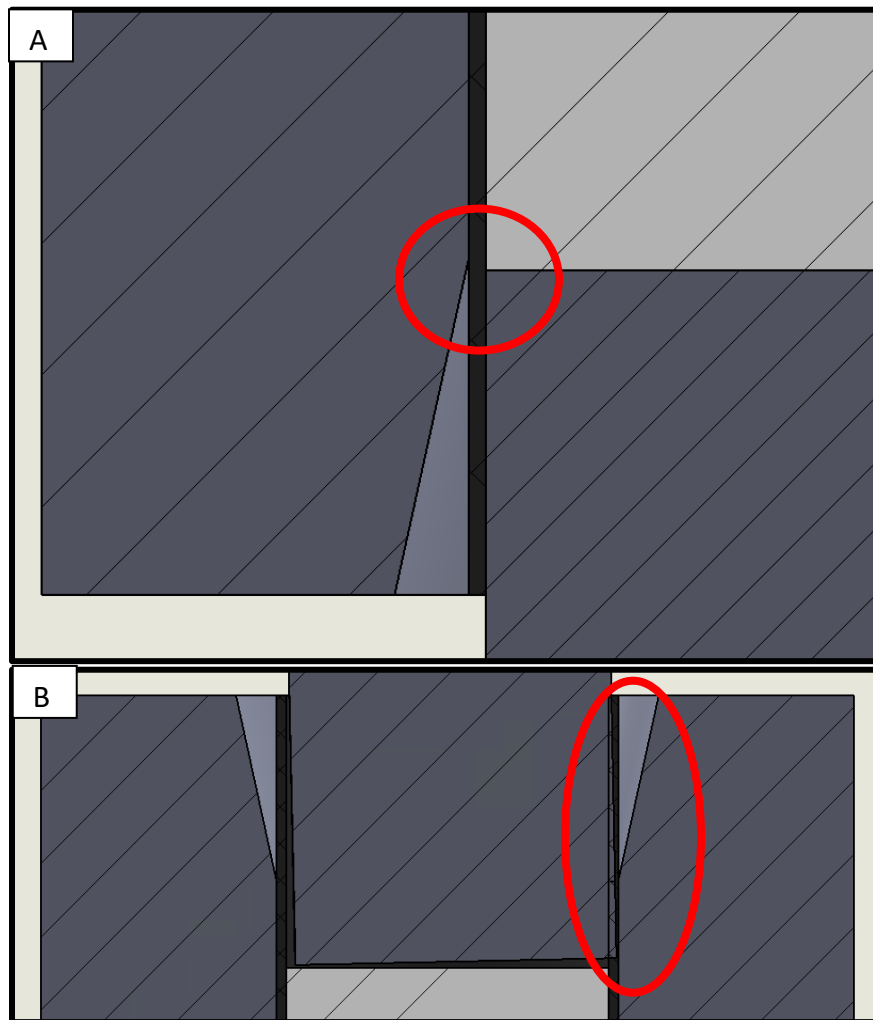


Figure 35: A) Minimal contact, B) cock – eyed punch.

From this it was learned that die geometry is the most critical factor for maintaining consistent heating and pressure during sintering.

1.27. Thermal stability

It is been shown that at temperatures equal to or greater than 1,000 °C, hydroxyapatite dehydroxylates which leads to volume expansion and the creation of pores [72], decomposes to oxyapatite, and then to tricalcium phosphate [73] leading to degradation of mechanical properties [74,75]. Therefore, the most reliable material is made at temperatures below 1,000 °C. Figure 24 shows that decomposition did not occur. Figure 24 shows that decomposition to tricalcium phosphate did not occur during calcination or sintering for all powders. Slight peak shift in sintered specimens in XRD is expected and has been previously observed for slightly dehydroxylated HA [66]. Calculation of the full-width at half-maximum shows no grain distortion during calcination. It can also be seen from Figure 24 that there is an increase in the intensity of the (211) peak, first with pressure, and then continues to increase with increasing BNNP content. This behavior has been seen in other HA composites and is explained by the HA (211) plane forming a 68° angle with CNT and BN walls coupled with the angle between the HA (211) and (001) forming a 65° angle, so there is increased probability of the HA basal planes being parallel to the CNT and BN surface resulting in minimized lattice mismatch increasing the likelihood of epitaxial growth of the HA (211) plane off of the surface of our BNNPs [28,70].

1.28. Densification

When densifying neat HA powders, it was learned the heating rate and isothermal hold temperature played the largest role in creating fully dense samples. It is been shown that at temperatures at and above 1000 °C and in a vacuum dehydroxylation (Figure 36) of hydroxyapatite occurs which leads to volume expansion and the creation of pores [72] and decomposes to hydroxy – oxyapatite and then to tricalcium phosphate [73], and leads to degradation of the mechanical properties [74,75]. Therefore, for spark plasma sintering the most

reliable material is made at temperatures below 1,000 °C. Figure 23 shows optically opaque hydroxyapatite prepared using SPS.

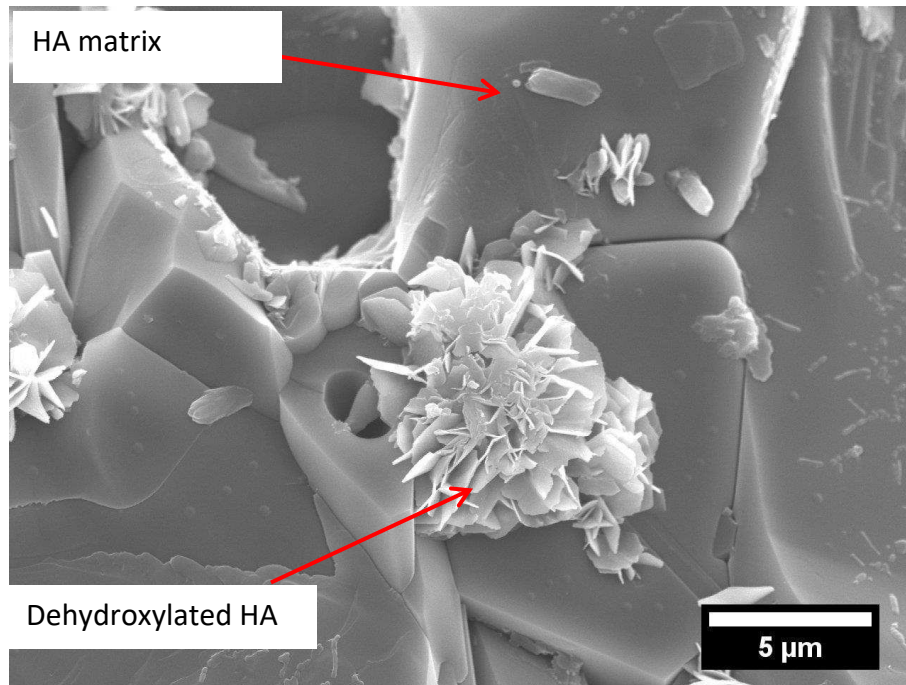


Figure 36: Fracture surface of sample showing dehydroxylation at grain boundaries

Therefore, a highly-controlled heating rate is key for attaining the isothermal hold without overshooting to a temperature where dehydroxylation will occur. Furthermore, the applied load also plays a role in the densification. As mentioned before dehydroxylation of HA becomes favorable at temperatures above 1000 °C. During dehydroxylation a water group is released. The produced water can be trapped inside the sample during pore collapse or when pore channels are no longer connected and thus cause desintering at elevated temperatures due to the expansion of the trapped gas. Therefore, it is important that the load be such that it causes plastic collapse of pores but allows the pores to remain open enough to remove all water before stage III sintering (Figure 37, [76]).

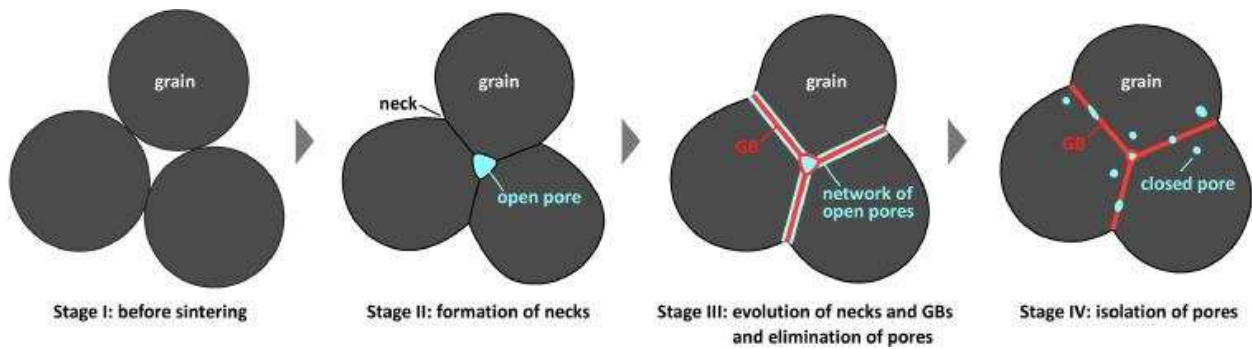


Figure 37: Sintering stages

The above considerations also apply to densifying the composite powders but have one further consideration which is that the nanoplates act as diffusion barriers [22,25–27,77] and thus hinder densification. To overcome this, the isothermal hold temperature and applied load were increased while the hold time was decreased. This however, did not produce samples with densities between 97 and 100%. The Taguchi Design of Experiments method was used in conjunction with SPS parameters to determine sintering parameters that produced samples with the highest density for the HA + 0.5wt% BNNP powders. From here, it was discovered that pressure and hold time played a larger role here than with pure HA. From Figure 22, it can be seen that for the HA + 0.5wt% BNNP samples that the average sample density was highest at 80 MPa. The samples sintered with 70 MPa applied pressure likely didn't experience enough plastic flow to eliminate pores and create a fully dense structure. The samples sintered with 90 MPa hold pressure had lower densities than samples with 80 MPa hold pressure and experienced more plastic flow likely closing off pore channels and trapping water in the isolated pores prior to stage III sintering and experience pore expansion due to the trapped water vapor.

1.29. Grain size effect on mechanical properties

Using the shear lag model (Figure 38) to compute the critical length that BNNPs would have to be to experience maximum loading during applied stress can tell us the effect of the BNNPs.

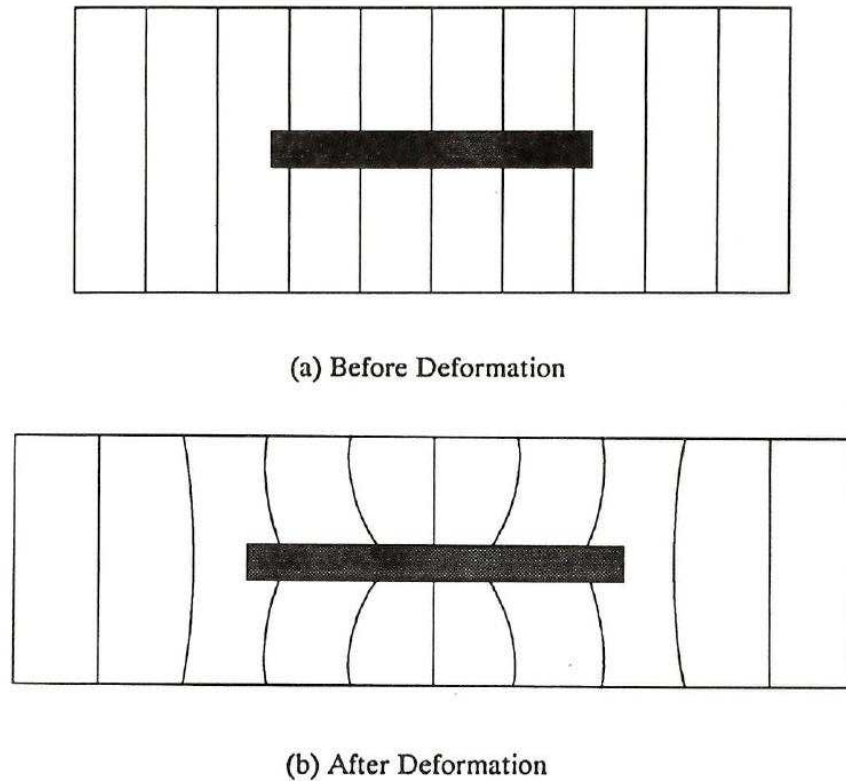


Figure 38: Shear lag model

For the shear lag model [78] it is assumed that:

1. There exists a perfect bond between fiber and matrix, i.e. there is no sliding between the two.
2. Poisson's ratios of the fiber and the matrix are equal, which implies an absence of transverse stresses when the load is applied along the fiber direction.
3. All load transfer occurs via shear in the matrix and at the fiber/matrix interface. This shear stress is assumed to be constant and there is no direct loading of the fibers.

4. Stress concentrations at the fiber ends are ignored.

This shear stress can be computed using Equations 13, 14, 15, and 16.

$$\beta = \sqrt[2]{\frac{2\pi G_{HA}}{E_{BNNP} d_{BNNP} w_{BNNP} \sqrt{\ln\left(\frac{R_{HA}}{r_{BNNP}}\right)}}} \quad (13)$$

Where β is the load transfer parameter, G_{HA} is the shear modulus of the matrix, in our case hydroxyapatite, E_{BNNP} is the elastic modulus of the fiber, $BNNP$, d_{BNNP} is the fiber thickness, w_{BNNP} is the fiber width, and R_{HA} is the thickness of the radius surrounding the fiber which is assumed to be the grain size, and r_{BNNP} is half the thickness of the fiber.

$$G_{HA} = \frac{E_{HA}}{(1 + \nu_{HA})} \quad (14)$$

The shear modulus is computed using Equation 13, where E_{HA} is the elastic modulus of the hydroxyapatite, and ν_{HA} is the Poissons ratio of the matrix.

$$\tau_i = \frac{r_{BNNP} \sigma_{applied} \beta}{2} \frac{\sinh\left(\beta \left[\frac{l_{BNNP}}{2} - \frac{l_{BNNP}}{4}\right]\right)}{\cosh\left(\beta \frac{l_{BNNP}}{2}\right)} \quad (15)$$

Where $\sigma_{applied}$ is the stress applied to the matrix, here the maximum or failure stress was used to for this parameter.

$$l_c = \frac{\sigma_{ultimate\ BNNP}}{\tau_i} d_{BNNP} \quad (16)$$

Where $\sigma_{ultimate\ BNNP}$ is the ultimate strength of the fiber and d_{BNNP} is the diameter of the fiber.

With $E_{HA} = 120$ GPa, $\nu_{HA} = 0.27$, $\sigma_{ultimate\ BNNP} = 83$ MPa, $E_{BNNP} = 1$ TPa, $l_{BNNP} = 262$ nm, and $d_{BNNP} = w_{BNNP} = 75$ nm, using these equations to generate Table 7 it was found that the length of the BNNPs (262 nm) used in this study were all shorter than the critical length based on grain

size and applied stress and therefore did not contribute to the increases in strength or fracture toughness.

Table 7: Shear lag analysis of BNNP critical lengths

Sample	Average Failure stress (MPa)	Grain size (nm)	Critical length of BNNP (μm)
HA + 0.5wt% BNNP	71.19	356	2.89
HA + 1.0wt% BNNP	79.79	290	2.51
HA + 2.0wt% BNNP	60.64	261	3.25

The critical length of the reinforcement is displayed below in Figure 39, which shows the effect of the critical length of a reinforcing fiber as a function of applied stress and consequently the stress the fiber experiences via shear.

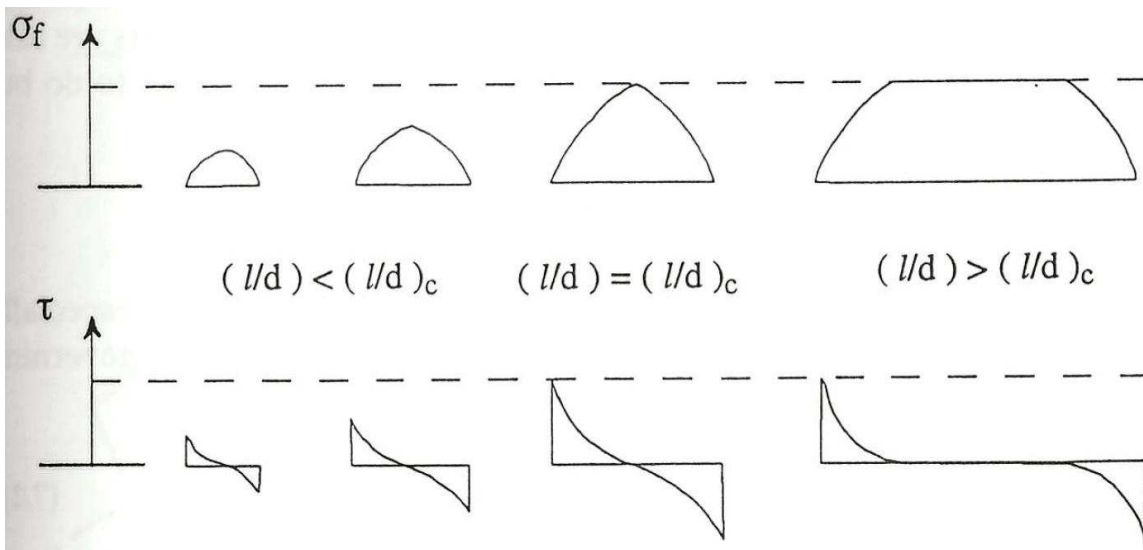


Figure 39: Graphical depiction of fiber critical length versus applied stress and shear stress

These increases in strength and fracture toughness can be attributed to the grain size refinement caused by the BNNP because the BNNP of this study are all shorter than the critical length to experience maximum loading in the HA matrix. The Hall-Petch relationship which equates the increase in yield strength to the decrease in grain size [20], has been claimed for ceramics [4,40,43], though this is inaccurate assessment of the mechanism by which the toughness or strength increases with decreased grain size. The Hall-Petch relationship implies dislocation motion and increased dislocation pile-up due to the increased amount of grain boundaries. Because of the ionic or covalent bond type of ceramics dislocation motion is difficult because similar charges would have to slide past each other to accommodate a new bond to form. Instead, the increase in fracture toughness with fracture toughness can be attributed to the grain boundaries themselves. Grain boundaries are regions of atomic disorder and lattice mismatch. This increases the difficulty for crack propagation through a previously intact grain. From Figure 26 we see that that there is transition from intergranular fracture to transgranular fracture first with increasing pressure and then with increasing BNNP content.

1.30. Mechanical Testing

1.30.1. Flexural Testing

Because of differences in testing method and differences in the reported material properties it is critical that the method used be the most appropriate method. Materials tend to fail at the region of highest stress intensity and ceramics especially are sensitive to porosity and cracks in a tested sample. During 3 – point bending, the region of highest stress is the mid – span of the beam (Figure 40). This constrains to sample to fail in the middle. During 4 – point bending a region of constant moment and therefore a region of constant stress (Figure 40).

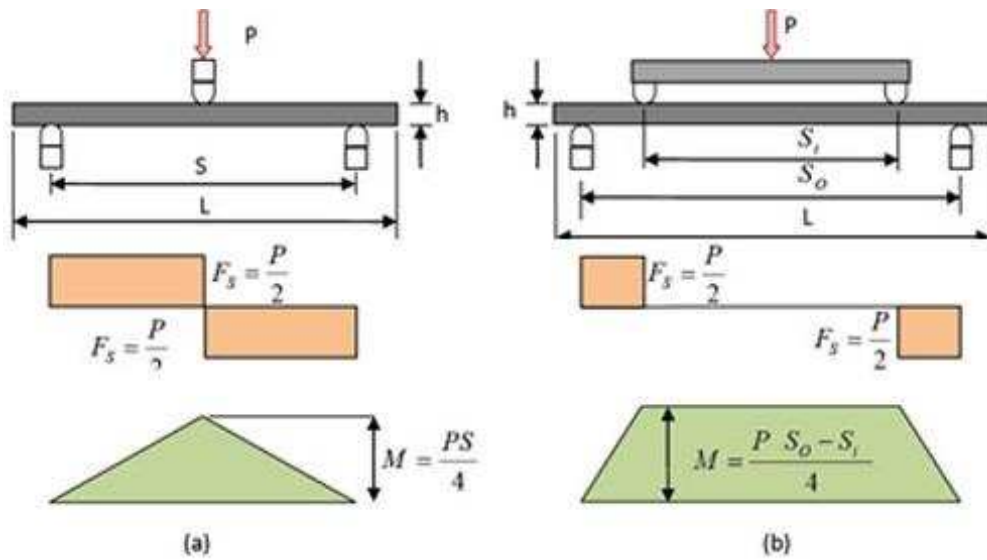


Figure 40: a) 3 – point bending and b) 4 – point bending, schematic, shear, and moment diagrams.

Consider the simple scenario shown below in Figure 41, where two cracks of unequal length are present in a beam; a short crack at the middle of the beam and a long crack located at one – quarter the length of the beam.

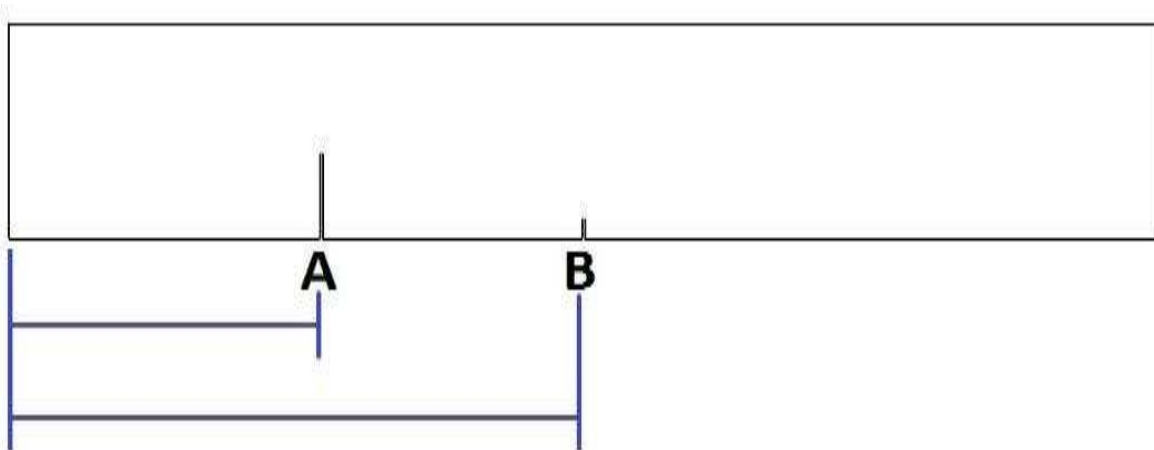


Figure 41: Cracked beam with crack at middle of beam and crack at quarter length of the beam.

One would reason that since the crack at site A is longer than at site B that the sample would like have higher stress and fail at that site. However, it can be shown that the stress intensity (K) is higher at site B. Consider the following analysis where K is defined as:

$$K = Y \sigma \sqrt{a} \quad (17)$$

Where, σ is the applied stress, a is the length of the crack and the geometry factor, Y , is defined as $Y \sqrt{\pi}$ [10] and is assumed be the same for both cracks in this analysis. During 3 – point bending the stress at site A and B, respectively are:

$$K_A = Y \sigma_A \sqrt{a_A} \quad (18)$$

$$K_B = Y \sigma_B \sqrt{a_B} \quad (19)$$

For 3 – point bending the stress at site A will be:

$$\sigma_A = \frac{1}{2} \sigma_B \quad (20)$$

For the stress intensity factor to be larger at site B to occur:

$$Y \sigma_B \sqrt{a_B} > Y \frac{1}{2} \sigma_B \sqrt{a_A} \quad (21)$$

Dividing by common terms and solving for the crack length at site B yields:

$$a_B > \frac{1}{4} a_A \quad (22)$$

Therefore, for crack lengths at site B that are greater than 25% the length of the crack at site A the stress intensity factor will be higher at site B in 3 – point bending. Now consider a crack at site A that is 1% longer than the above criterion in Equation 22. The ratio of stress intensity factors is:

$$\frac{K_B}{K_A} = \frac{\sigma_B \sqrt[2]{0.26 a_A}}{\frac{1}{2} \sigma_B \sqrt[2]{a_A}} = 2\sqrt{0.26} \sim 1.02 \quad (23)$$

For very small changes in crack length the stress intensity factor at site B is 2% higher than the critical value above. Though this small change in crack length and ultimately the stress intensity factor may or may not be significant for this test, if we consider the same beam in 4 – point bending where:

$$\sigma_A = \sigma_B = \sigma \quad (24)$$

With the 1% longer crack at site B the ratio of stress intensity factors becomes

$$\frac{K_B}{K_A} = \frac{\sigma \sqrt[2]{0.26 a_A}}{\sigma \sqrt[2]{a_A}} = \sqrt{0.26} \sim 0.509 \quad (25)$$

Solving for K_A from Equation 25 yields:

$$K_A \sim 1.96 K_B \quad (26)$$

For a crack 1% longer than the critical value above produces a stress intensity factor that is nearly double that of the stress intensity factor at site B. From the analysis of the beam in 3 – point bending it is possible that larger flaws exist closer to the end of the sample but might not fail because of the lower stress that region of the beam is experiencing. This leads to a situation where higher flexural strength is computed for the beam. This possibility also applies to 4 – point bending but that chance of missing the large defect size is decreased due to the wider region of stress. It has been shown that for brittle materials there is a detectable difference in Weibull modulus [79] and in flexural strength [80,81] in 3 vs 4 point bending, with the results for 3 point bending being consistently higher. These differences can be attributed to dependence on fracture toughness, flaw populations, and applied stress state [82,83].

Though 3-point bending is less sensitive to pin eccentricity it becomes easy to reject samples that do not fail at the center loading pin, working under the assumption that the sample was damaged during preparation/handling, thus ensuring only the best samples are analyzed and inflating any reported value.

1.30.2. *Vickers Hardness*

Figure 28 shows that average hardness slightly decreases and then increases with increasing BNNP content, which is a different finding from other researchers who have shown increasing hardness with increasing reinforcement in HA composites [28,33,70,71] for samples of varying density and in some cases hardness of composite samples was significantly higher than that of pure HA. However, other studies have shown steady decreases in hardness with increasing reinforcement content in Al₂O₃ [22,84] and in Si₃N₄ [21,85,86] for samples with similar densities. The latter authors attribute the decrease in hardness to the reinforcing material being softer than the matrix material and thus causing the decrease in hardness. These results show that hardness is nearly unaffected by increased BNNP content for fully dense samples sintered under different conditions with varying grain sizes.

1.30.3. *Fracture Toughness*

As previously mentioned fracture toughness is a material property that describes the ability of a crack containing material to resist fracture. It is related to the critical energy release rate of the material. To cause crack propagation a tensile stress must be applied to the crack. During flexure, the applied bending stress is translated into energy cause crack extension, of an existing crack, in the natural direction of the crack. In the case of computing fracture toughness through indentation there are several factors that are different. During indentation, the energy of the

applied load is used to cause plastic/elastic deformation in the sample and as well as creating many new cracks in the material (Figure 42).

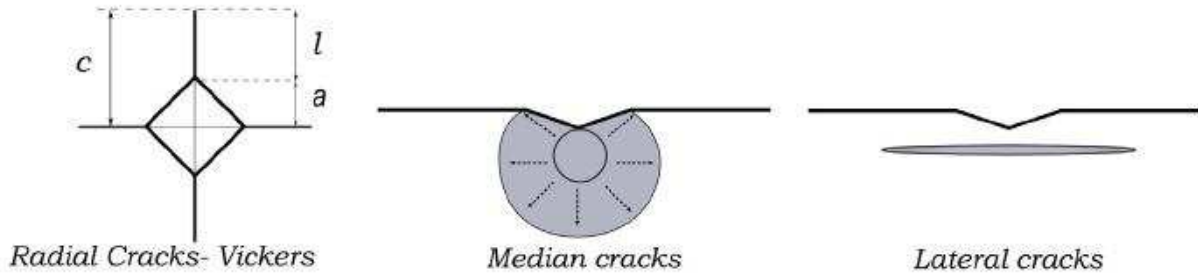


Figure 42: Comparison of geometries of radial, median, and lateral crack around a Vickers indentation [87]

With VIF it is crucial that cracks are accurately visualized. In this study and the studies of Miyazaki [58] cracks were imaged using contrast enhancing techniques. Miyazaki performed VIF tests on silicon carbide using a test load of ~ 20 kgf and enhanced crack contrast using varnish diluted with paint thinner. This method seems to be acceptable for measuring crack lengths greater than ~708 μm produced from higher indentation loads. In this study, using lower loads, VIF cracks were measured using a similar method where an oil based dye was diluted to 12 wt% in acetone and imaged using optical microscopy (Figure 43). Other samples sintered and tested at the same conditions were imaged in SEM using backscatter mode (Figure 44) and produced significantly different results.

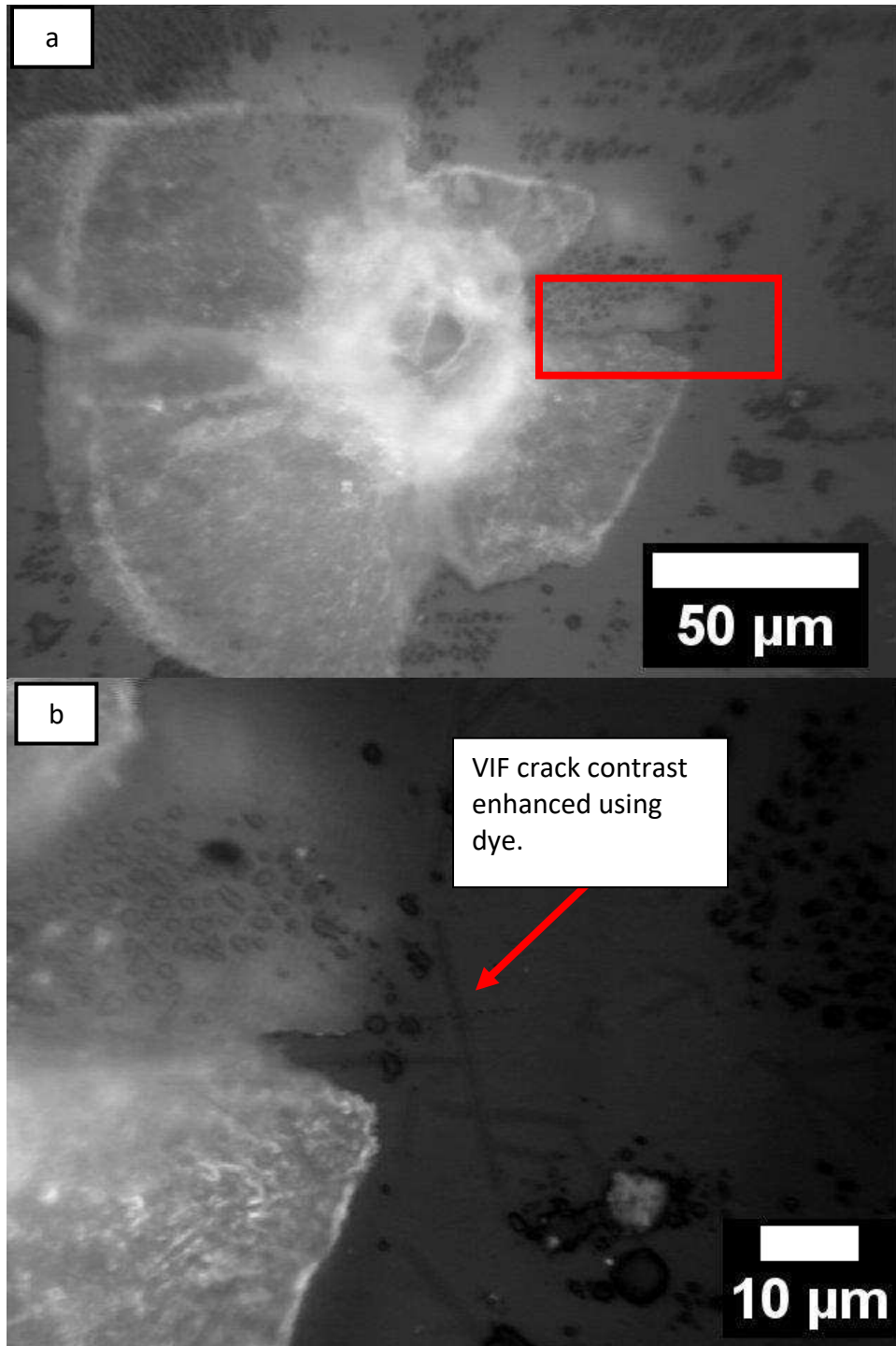


Figure 43: Optical images of VIF cracks. a) Image of whole indenter and b) zoomed in image of crack from a.

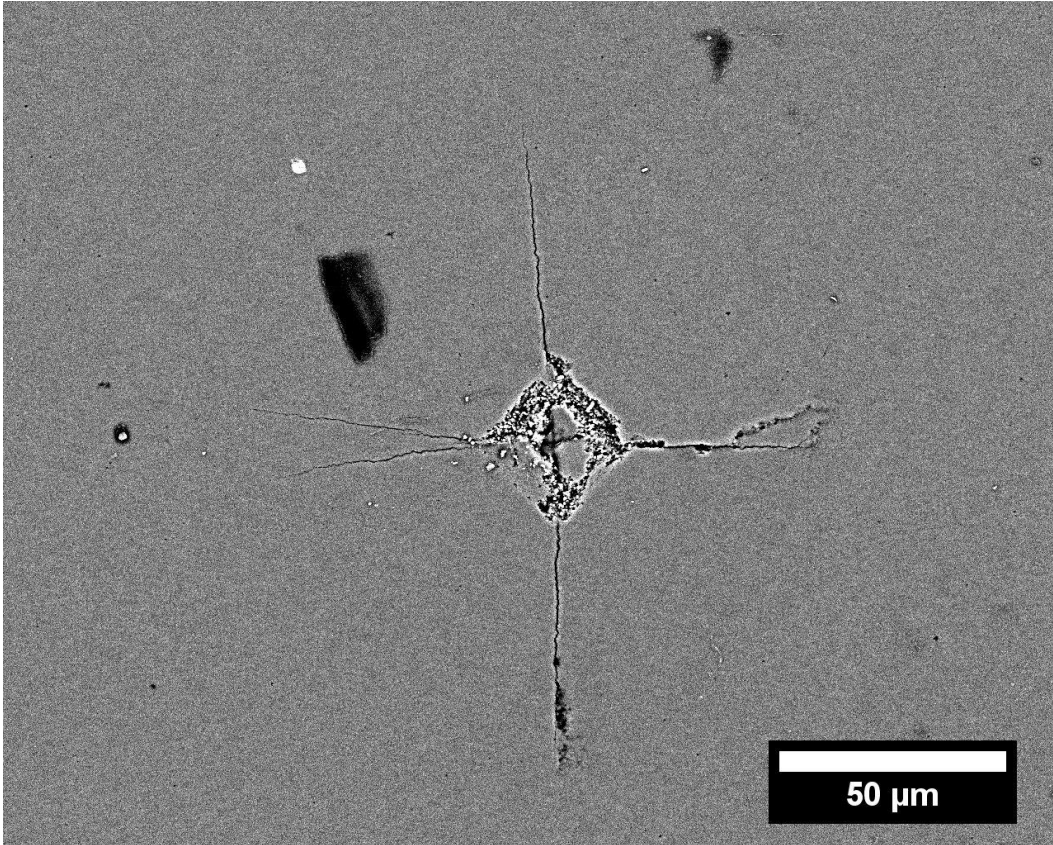


Figure 44: SEM image of HA VIF indent imaged in back scatter mode

For samples sintered and tested at the same conditions produced significantly different results. This demonstrates the dependence on crack imaging technique and it can also be concluded that enhancing crack contrast in this manner may not be appropriate for small cracks (~163-276 μm). Furthermore, with VIF, it is important that an accurate calibration constant be used in Equation 3 to obtain reliable results [87]. The calibration constant is especially important for materials with low fracture toughness because slight changes in the calibration constant can have a large effect on the computed fracture toughness. For brittle materials with low fracture toughness during Vickers indentation the material tends to suffer from spalling of the surface. Without accounting for the energy that was dissipated in spalling the sample, using the calibration constant, this can lead to inflated values of fracture toughness due to the dissipated energy not causing crack

extension. An example of surface spalling during indentation is shown in Figure 45. For these reasons in conjunction with our experimental findings, it can be concluded that the VIF technique may be inappropriate for brittle material K_{IC} determination [60].

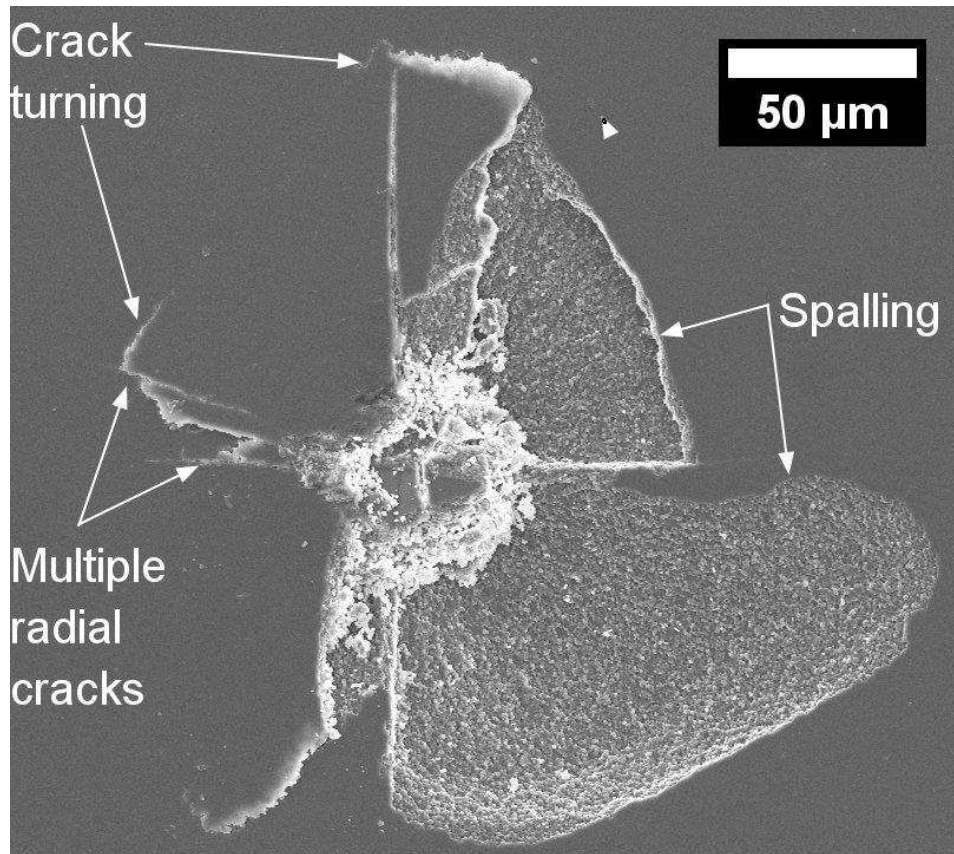


Figure 45: Flawed Vickers indentation

In Figure 29 SEVNB fracture toughness was evaluated against VIF indentation fracture toughness and shows that the fracture toughness measured using VIF is lower than measured by SEVNB. HA BNNP 1.0 and 2.0 wt. % samples were very brittle and were not able to be notched and sharpened with breaking prior to testing and consequently were not able to be tested. The SEVNB results being higher than that of VIF is opposite of what would be expected due to the lengthy sample preparation process [55] as compared to VIF samples [88]. Figure 29 also shows

increased HA fracture toughness for the 0.0 and 0.5 wt% samples using the SEVNB technique and for the VIF that fracture toughness initially decreases and then increases with increasing BNNP content at full density. This study shows decreasing VIF fracture toughness with increasing BNNP content, where other studies show increasing VIF fracture toughness with varying density and in some cases, composite density higher than that of the neat samples. Analyses of the VIF cracks shows increasing crack length with increasing BNNP content and analysis of the indents show that there is less surface spalling with increasing BNNP content. Despite all of this, it has been shown that VIF technique may not be appropriate for large volumes of brittle materials [60]. For the HA + 0.0wt% BNNP samples the fracture toughness was measured as $2.3 \text{ MPa m}^{1/2}$, a 130% over the previously published value of $1.0 \text{ MPa m}^{1/2}$. This increase can be attributed to the change from intragranular fracture to transgranular fracture due to the grain size refinement of the BNNPs.

1.31. Statistical Effects of BNNP Addition to Hydroxyapatite

As seen in Figure 31 there is a steady decrease in the measured Weibull Modulus for all samples and all mechanical tests of this study and from Table 6 we coincidentally see good agreement between the scale factor and the average. For the Normal Distribution, the average represents the point at which 50% of the sample population is toward the left tail of the distribution and for the Weibull distribution the scale factor represents the point at which 63% of the sample population is toward the left tail of the distribution. Figure 46 shows a comparison between the Weibull and Normal Probability Density Functions (PDF) for the HA + 1.0wt% BNNP flexural strength samples.

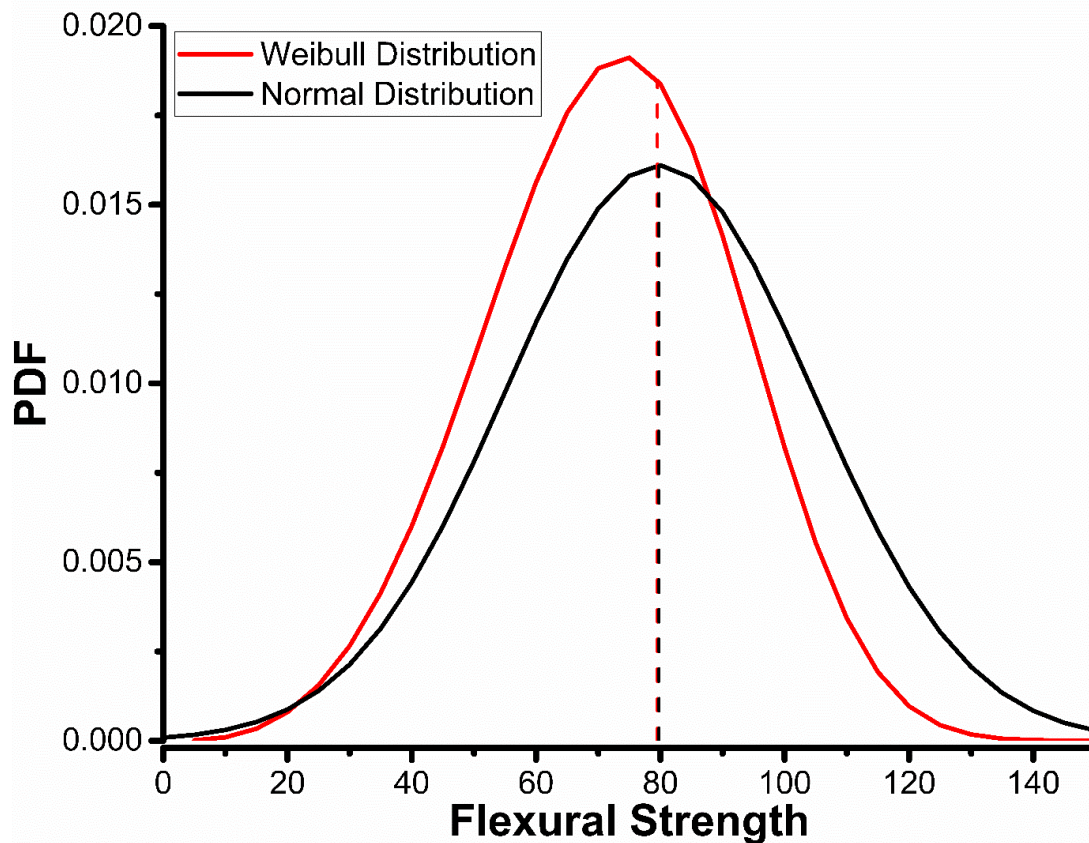


Figure 46: Weibull and Normal Probability Density Functions for HA + 1.0wt% BNNP flexural strength

From Figure 46 we can see that the agreement between the scale factor and average is due to the similarity in the shape of each distribution, where the dashed lines indicated the scale parameter, and average for the Weibull and Normal Distributions, respectively. The similarity between the Weibull and Normal distributions has previously been seen in construction materials [89]. As previously mentioned, studies have shown that a Normal Distribution of property values for a ductile material yields a reasonably accurate characterization of material behavior; the same cannot be said for the case of brittle materials. Instead the Weibull distribution is necessary to account for the variability of strength and the probability of survival of a particular component as a function of its volume and the applied stress [10].

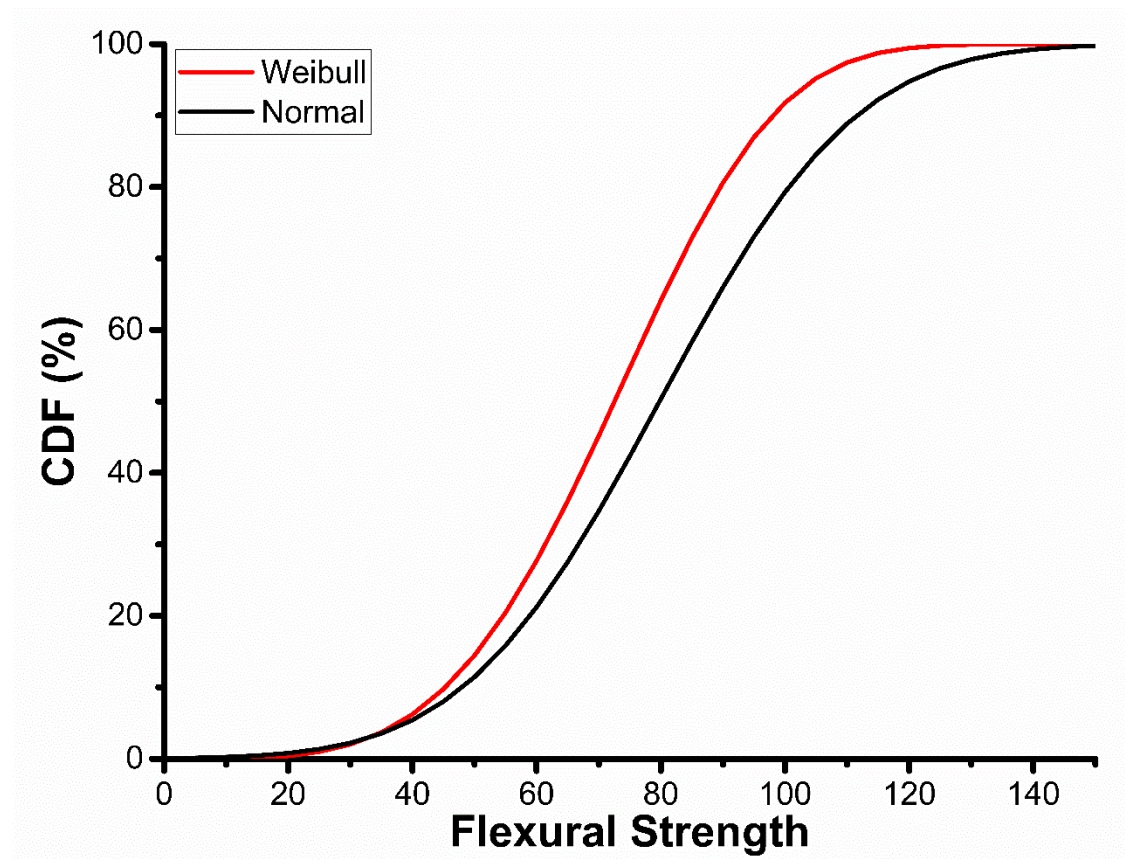


Figure 47: Weibull and Normal Cumulative Distribution Functions for HA + 1.0wt% BNNP flexural strength

Despite the similarities between the Normal and Weibull PDFs. Analysis of the Cumulative Distribution Functions (CDF), shown in Figure 47, shows that that the probability of failure at any given stress is higher for the Weibull distribution. The difference between the average strength and the strength scale factor is 0.34%, but this leads to a difference of 14% of the failure probability at 80 MPa, demonstrating the importance of using the correct statistical model to analyze the data.

1.32. Statistically Designed Loading of Materials

Using Figure 48 and Figure 49 the cumulative distribution functions for the flexural strength and SEVNB fracture toughness, respectively, can be used to compute the probability of failure for the composite.

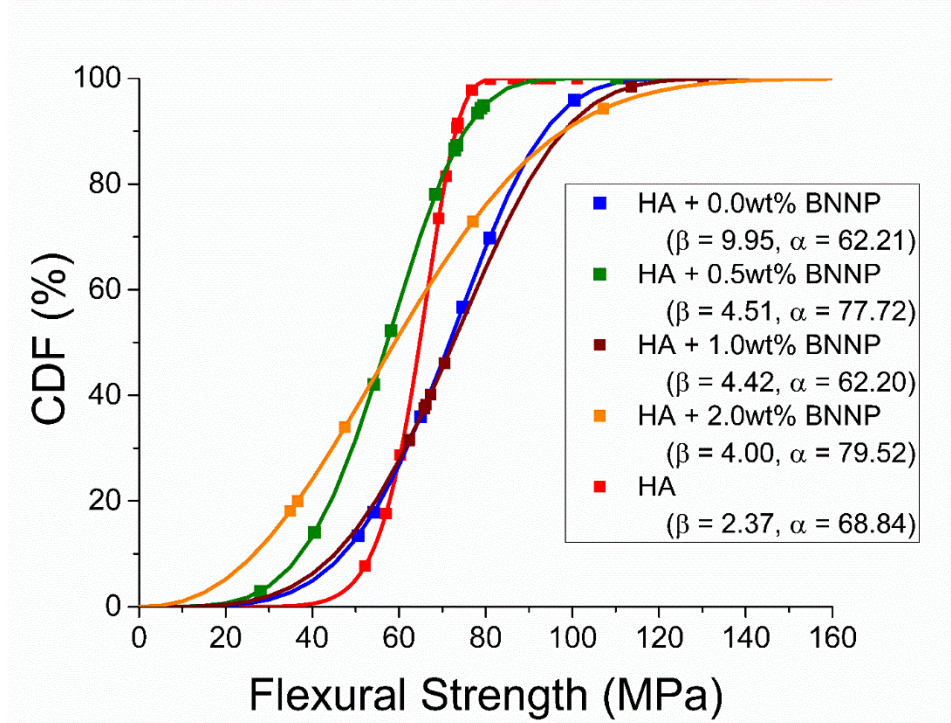


Figure 48: Flexural strength Cumulative Distribution Function

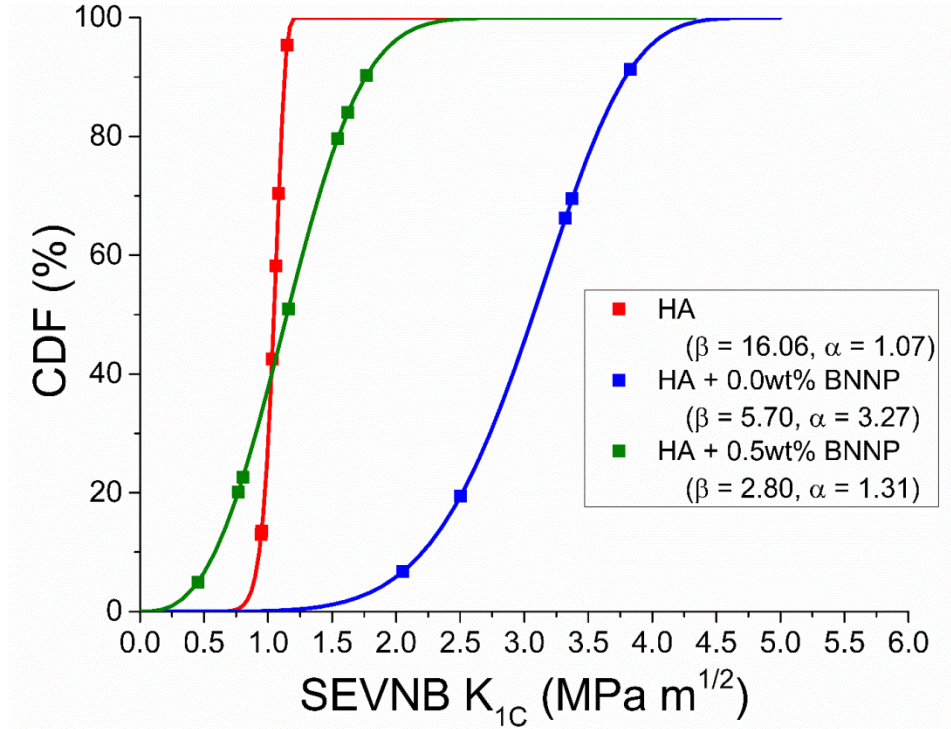


Figure 49: SEVNB Fracture Toughness Cumulative Distribution Function

Since the goal of this project is to design a suitable implant material for use in the human body it is important to interpret these results with respect to the intended application. If it is assumed that: the maximum force a human jaw can apply while biting is 1109 N [90], the jaw can be modeled as a rectangular beam with 12.00 mm base, 19.00 mm height, and 160 mm length, and that the jaw bone is loaded in 4 point bending, the stress the jaw bone would experience is 30.72 MPa. Using this stress to compute the probability of failure using Eq.12, there is less than 5% chance of failure for all compositions, except the 2.0wt% BNNP samples (Table 8).

Table 8: Flexural Strength Probability of Failure

Material	Scale factor, α (MPa)	Shape parameter, β	CDF
HA + 0.0 wt% BNNP	77.72	4.51	1.51%
HA + 0.5 wt% BNNP	62.2	4.42	4.33%
HA + 1.0 wt% BNNP	79.52	4	2.20%
HA + 2.0 wt% BNNP	68.84	2.37	13.73%
HA	62.21	9.95	0.09%

CHAPTER 6: CONCLUSIONS

Due to the application of pressure, fast heating rates, and inert environment that SPS can be used to prepare fully dense hydroxyapatite and boron nitride nanoplatelet composites.

This study demonstrates the utility of the Taguchi design of experiments method for obtaining optimum sintering parameters for ceramic matrix composites prepared using spark plasma sintering. These results are only applicable for this material system but this technique serves as a material independent approach of determining sintering parameters.

From the results of this study it is seen that increasing BNNP content leads to a steady decrease in reliability for all composites and all mechanical tests. From Figure 27, Figure 28, & Figure 29 increased strength, minimal change in hardness, and decreasing fracture toughness with increasing BNNP content is reported. Despite the trend downward with increased BNNP content increased fracture toughness over the published value of $1.0 \text{ MPa m}^{1/2}$ for the 0.0 and 0.5 wt% BNNP hydroxyapatite composites and increased flexural strength for all composites over published values and high reliability for the low pressure sintered hydroxyapatite is observed. The importance of using the SEVNB technique to measure fracture toughness is demonstrated, because the HA + 1.0 wt% and 2.0wt% BNNP samples were too brittle to test using this method indicating that these compositions may be unsuitable for use in the human body. Further demonstration of the importance of the SEVNB technique to measure fracture toughness and measuring flexural strength in 4 point bending for ceramics matrix composites is important because of the area of constant stress created with this testing geometry. It can also be concluded that Weibull analysis is extremely important for ceramics because of decreasing reliability with increasing BNNP content, especially for biomedical ceramics designed for

implantation in the human body. From these results, it can be concluded that it is better to report the scale parameter and shape factor for ceramics mechanical properties. These values give more information than averages and standard deviations for material properties. The shape factor yields information about the flaw distribution of the tested material population and the scale parameter can be used to compute a more accurate factor of safety when coupled with analysis of the cumulative distribution function of the material. This further leads to the conclusion that this analysis can help design safe operating parameters for ceramics, even with low reliability as evidenced in Figure 48, where the probability of failure is low under an assumed stress state for these HABNNP composites.

Most importantly, it can be concluded that BNNPs can increase the fracture toughness and flexural strength of hydroxyapatite for implantation materials but because of the decrease in reliability and the short length of BNNP, this material may not be the most ideal candidate for this application.

1.33. Pressure effects on the mechanical properties of hydroxyapatite

Watanabe et al. [91] reported that hydroxyapatite densified via SPS was found to have preferential epitaxial growth of the c – axis (Figure 50) in the HA crystal in the direction perpendicular to the load direction. This is indicated in Figure 50 by the green arrow, showing the circular plane that is perpendicular to the loading direction.

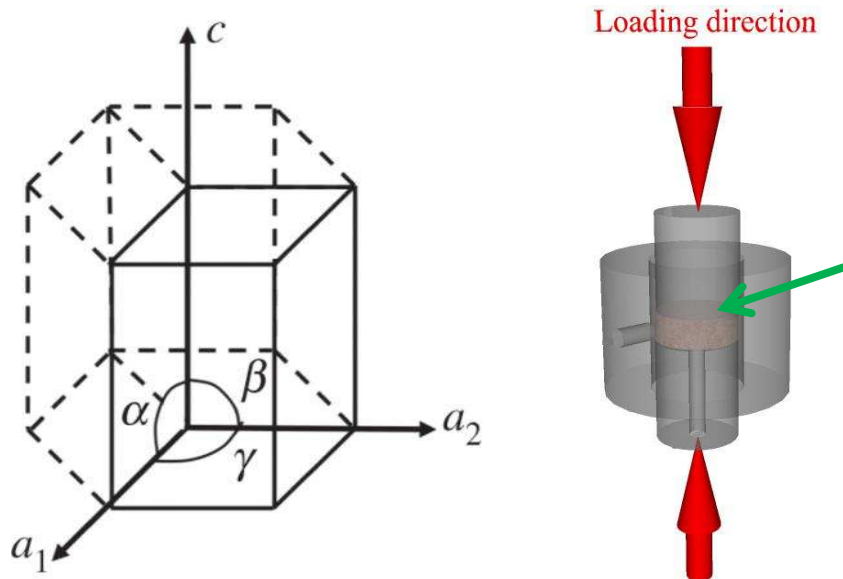


Figure 50: Left) Hexagonal crystal structure Right) Applied load during pressure assisted sintering processes.

This preferential growth could lead to possible differences in tested mechanical properties based on the orientation of the beam cut from the cylindrical puck. Countless combinations of various crystallite orientations exist but for the worst-case scenario where all the hydroxyapatite crystals growth in the same direction, there exists 3 distinct orientations of the beam, all of which are 90° apart (Figure 51). Figure 51 a represents a sintered specimen, where the blue line represents cut 1 and the red line represents cut 2, where the cuts travel through the thickness axial thickness of

the sample. Figure 51 b shows a beam that made from cut 1 then is rotated 90° (on its side with respect to cut direction) before testing, Figure 51 c represents a beam from cut 2, and Figure 51 d represents a beam from cut 1.

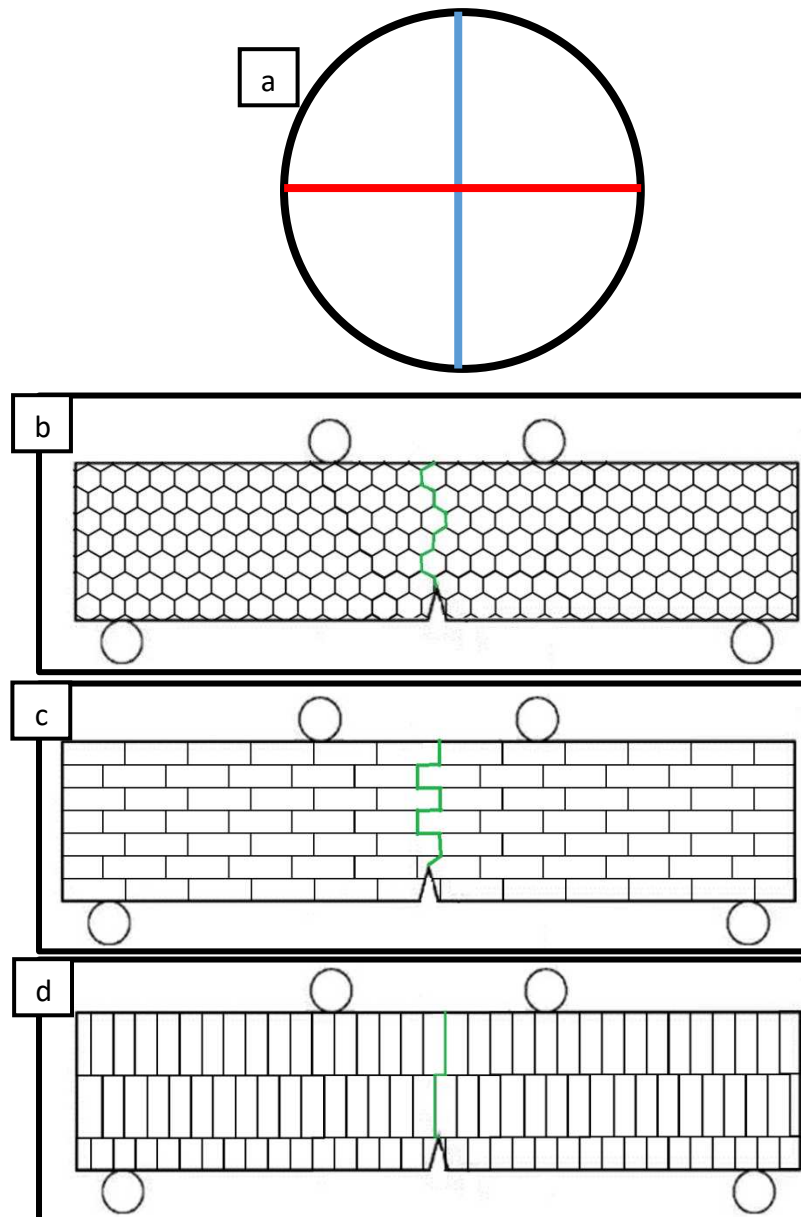


Figure 51: Hydroxyapatite C-axis orientation due to applied pressure. a) Cuts through sample, b) orientation 1, c) orientation 2, and d) orientation 3.

Shown in each figure is a SEVNB specimen that has been prepared for fracture toughness testing in 4 – point bending. The green arrows in each image (Figure 51 b – d) represent the direction a crack could travel. Because of the presence of more or less grain boundaries ahead of the crack tip the sample will have higher or lower fracture toughness or flexural strength. It would be beneficial to study the effect of sample orientation on the failure statistics of HA and HA – BNNP composites.

1.34. BN nanotubes

As briefly mentioned in Chapter 5: Section 5.3 Grain size effect on the properties (pg. 63) the BNNPs used in this study were all too short to contributed to the increases in strength. BN nanotubes with length greater than 3.25 μm will have an aspect ratio large enough that the BN nanotubes will see maximum loading during applied stress and therefore can contribute to increases in strength and fracture toughness.

1.35. Homogenous dispersion

Creating a homogenous dispersion prevents the reinforcing phase from agglomerating during drying and creating a weakening effect when sintered. It has been shown that nanoparticles can be coated with Cetyltrimethylammonium bromide (CTAB), which is a cationic surfactant. In water, the bromide ion associated with the head group of the surfactant dissociates at all values of pH to produce a positively charged head group [86]. This is demonstrated in Figure 52. It has been shown this process can create well dispersed mixtures by coating both GNPs and silicon – nitride nanoparticles in CTAB and then mixing the powders using an ultrasonicator [85,86]. Both phases being coated in a positive charge produces a repelling effect that they reasoned leads to creating a homogenous mixture. Similarly, Chen et al [6] created homogeneous dispersions of GNP and HA by individually mixing each powder in an aqueous solution of sodium dodecyl –

benzene sulfonate (an anionic surfactant) then combining both slurries and mixing using an ultrasonicator.

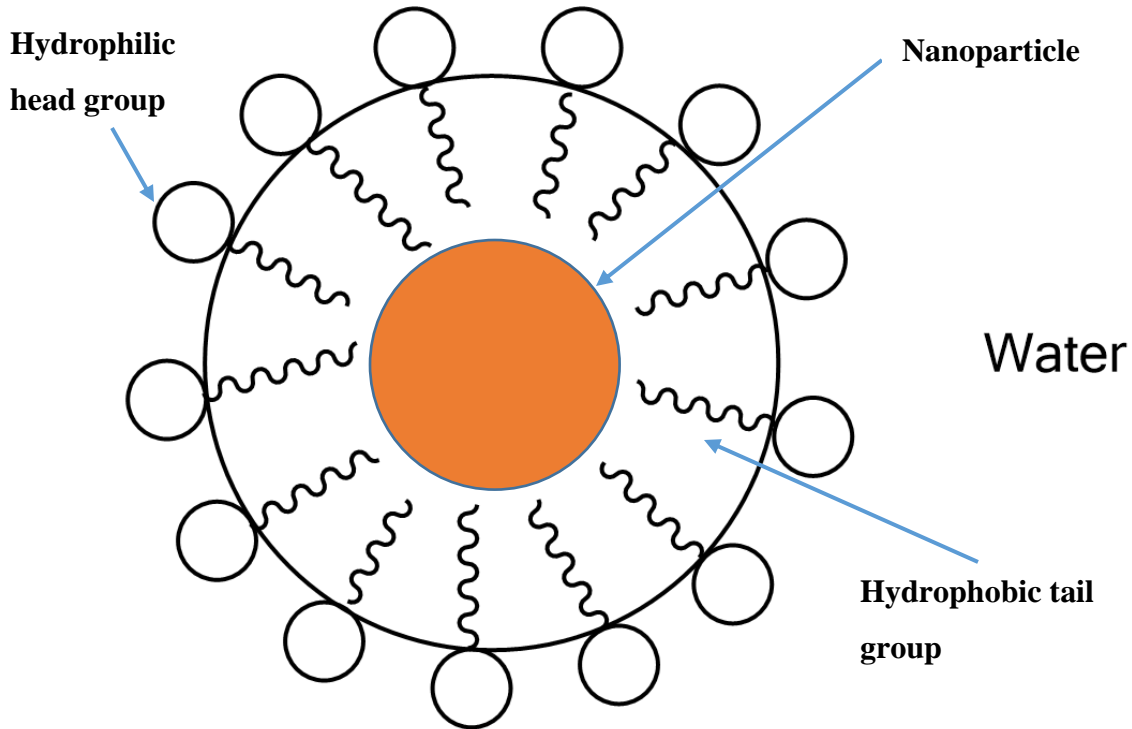


Figure 52: CTAB dissociation and coating of a ceramic nanoparticle

Applying this to HA – BNNP and HA – BNNT composites could create better dispersed mixtures. However, in both studies each constituent was coated in a surfactant with the same surface charge. The net repulsion of each powder could create a homogenous dispersion but also still lead to agglomeration. Mixing HA with a cationic surfactant and BNNPs or BNNTs with an anionic surfactant and then mixing both slurries using an ultrasonicator could produce a more homogenous suspension because the positively charged HA powder would be attracted to the negatively charged BNNPs or BNNTs. This better dispersion could lead to even further enhancement of the mechanical properties.

CTAB has shown to be toxic to the human body [92] so this is a concern for materials whose intended use is implantation. CTAB has also been shown to decompose at temperatures greater than 165 °C [93]. Since the sintering temperature for these materials 900 °C decomposition of CTAB will occur and will leave behind traces of carbon, nitrogen, and bromine. The human body is made of oxygen, carbon, hydrogen, nitrogen, calcium, and phosphorous so the trace amounts of carbon and nitrogen left behind should not increase the toxicity of the composite but may affect sintering kinetics and would need to be studied further. The trace amount of bromine left behind also should not increase the toxicity has bromine has been shown to be essential for life to occur [94].

1.36. Surface functionalization of BNNTs

In chemistry functionalization is defined as adding a functional group and a functional group is defined as a specific group of atoms within molecules that are responsible for the characteristic chemical reactions of those molecules. In the studies of Ciofani et al. [95] it was discovered that hydroxyl (OH) groups can be attached to BNNTs by ultrasonication in nitric acid (HNO₃) for six hours (Figure 53).

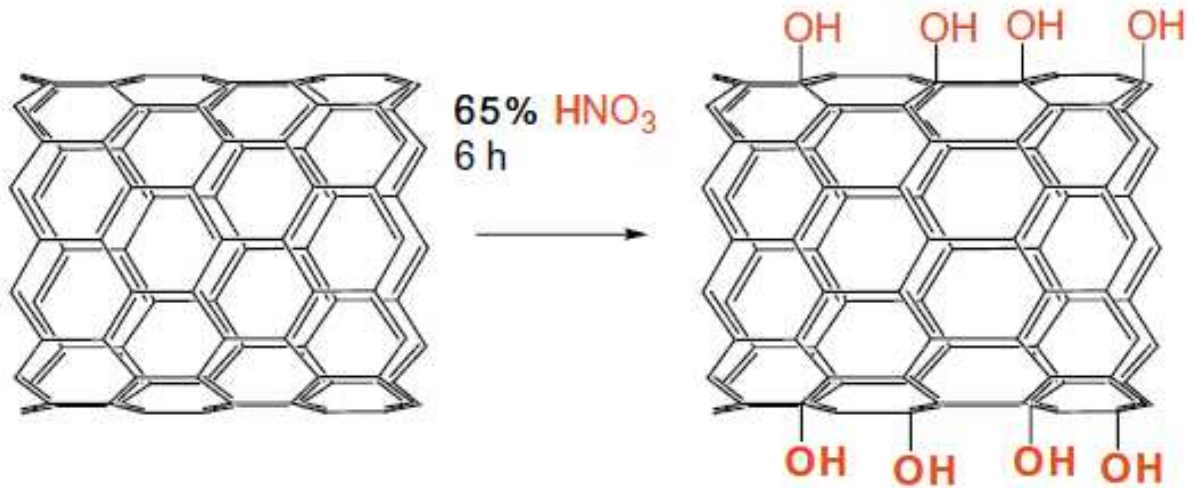


Figure 53: Functionalization of BNNTs [95]

The chemical formula of HA is denoted below in Equation 27.



The presence of additional hydroxyl groups on the surface of the BNNT or BNNP could lead to enhanced mechanical properties due to chemical attachment to of hydroxyl groups on the HA lattice (Figure 54) to the surface of the BNNTs and lead to HA epitaxy from the surface.

Epitaxial growth of HA from the surface of CNTs and BNNTs has already been shown [28,70] without surface functionalization.

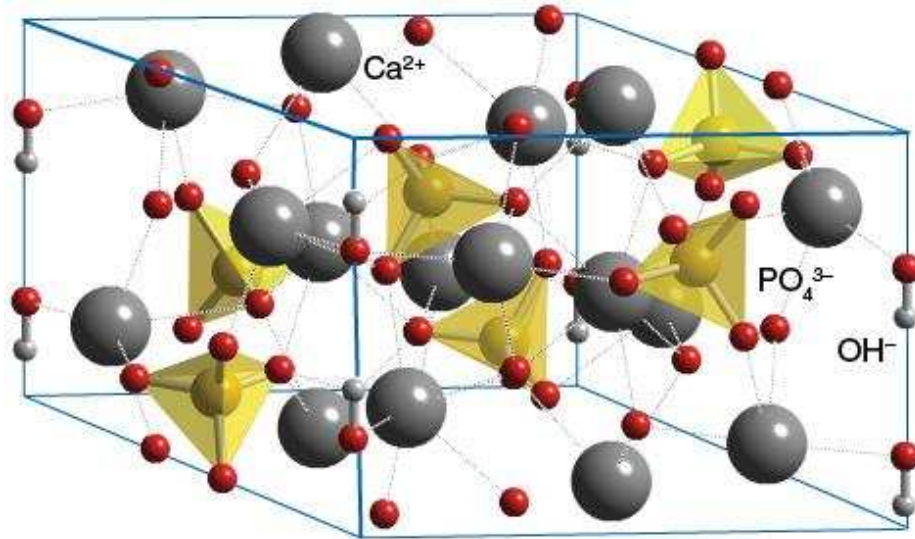


Figure 54: Hydroxyapatite crystalline lattice [96]. Ca^{2+} ions are the gray spheres, phosphate (PO_4) ions denoted by the yellow tetrahedra, and the hydroxyl groups are represented by the red (oxygen) and white (hydrogen) at the edges of the unit cell.

REFERENCES

- [1] D. Lahiri, S. Ghosh, A. Agarwal, Carbon nanotube reinforced hydroxyapatite composite for orthopedic application: A review, *Materials Science and Engineering: C*. 32 (2012) 1727–1758. doi:10.1016/j.msec.2012.05.010.
- [2] Q.D. Yang, B.N. Cox, R.K. Nalla, R.O. Ritchie, Re-evaluating the toughness of human cortical bone, *Bone*. 38 (2006) 878–887. doi:10.1016/j.bone.2005.10.014.
- [3] R.B. Cook, P. Zioupos, The fracture toughness of cancellous bone, *Journal of Biomechanics*. 42 (2009) 2054–2060. doi:10.1016/j.jbiomech.2009.06.001.
- [4] M. Aminzare, A. Eskandari, M.H. Baroonian, A. Berenov, Z. Razavi Hesabi, M. Taheri, S.K. Sadrnezhad, Hydroxyapatite nanocomposites: Synthesis, sintering and mechanical properties, *Ceramics International*. 39 (2013) 2197–2206. doi:10.1016/j.ceramint.2012.09.023.
- [5] Bioceramic, Wikipedia. (2014). <http://en.wikipedia.org/wiki/Bioceramic> (accessed December 13, 2014).
- [6] L. Zhang, W. Liu, C. Yue, T. Zhang, P. Li, Z. Xing, Y. Chen, A tough graphene nanosheet/hydroxyapatite composite with improved in vitro biocompatibility, *Carbon*. 61 (2013) 105–115. doi:10.1016/j.carbon.2013.04.074.
- [7] H. Liu, P. Xi, G. Xie, Y. Shi, F. Hou, L. Huang, F. Chen, Z. Zeng, C. Shao, J. Wang, Simultaneous Reduction and Surface Functionalization of Graphene Oxide for Hydroxyapatite Mineralization, *The Journal of Physical Chemistry C*. 116 (2012) 3334–3341. doi:10.1021/jp2102226.

- [8] A.A. White, S.M. Best, I.A. Kinloch, Hydroxyapatite–carbon nanotube composites for biomedical applications: a review, *International Journal of Applied Ceramic Technology*. 4 (2007) 1–13. <http://onlinelibrary.wiley.com/doi/10.1111/j.1744-7402.2007.02113.x/full> (accessed January 30, 2015).
- [9] D. Lahiri, V. Singh, A.P. Benaduce, S. Seal, L. Kos, A. Agarwal, Boron nitride nanotube reinforced hydroxyapatite composite: Mechanical and tribological performance and in-vitro biocompatibility to osteoblasts, *Journal of the Mechanical Behavior of Biomedical Materials*. 4 (2011) 44–56. doi:10.1016/j.jmbbm.2010.09.005.
- [10] R. Hertzberg, R. Vinci, J. Hertzberg, *Deformation and Fracture Mechanics of Engineering Materials*, 5th ed., John Wiley & Sons, Inc., 2013.
- [11] K. Budinski, M. Budinski, *Engineering Materials: Properties and Selection*, 6th ed., Prentice Hall, Upper Saddle River, 1999.
- [12] P. Cherukuri, S.M. Bachilo, S.H. Litovsky, R.B. Weisman, Near-Infrared Fluorescence Microscopy of Single-Walled Carbon Nanotubes in Phagocytic Cells, *Journal of the American Chemical Society*. 126 (2004) 15638–15639. doi:10.1021/ja0466311.
- [13] C. Cheng, K.H. Müller, K.K.K. Koziol, J.N. Skepper, P.A. Midgley, M.E. Welland, A.E. Porter, Toxicity and imaging of multi-walled carbon nanotubes in human macrophage cells, *Biomaterials*. 30 (2009) 4152–4160. doi:10.1016/j.biomaterials.2009.04.019.
- [14] C. Ramirez, P. Miranzo, M. Belmonte, M.I. Osendi, P. Poza, S.M. Vega-Diaz, M. Terrones, Extraordinary toughening enhancement and flexural strength in Si₃N₄ composites using graphene sheets, *Journal of the European Ceramic Society*. 34 (2014) 161–169. doi:10.1016/j.jeurceramsoc.2013.08.039.

- [15] C. Ramirez, M.I. Osendi, Toughening in ceramics containing graphene fillers, *Ceramics International*. 40 (2014) 11187–11192. doi:10.1016/j.ceramint.2014.03.150.
- [16] Tortuosity, Wikipedia. (2014). <http://en.wikipedia.org/wiki/Tortuosity> (accessed December 13, 2014).
- [17] D. François, A. Pineau, A. Zaoui, *Mechanical Behaviour of Materials*, Springer Netherlands, Dordrecht, 2013. <http://link.springer.com/10.1007/978-94-007-4930-6> (accessed January 5, 2015).
- [18] D. Golberg, Y. Bando, Y. Huang, T. Terao, M. Mitome, C. Tang, C. Zhi, Boron Nitride Nanotubes and Nanosheets, *ACS Nano*. 4 (2010) 2979–2993. doi:10.1021/nn1006495.
- [19] D. Lahiri, F. Rouzaud, T. Richard, A.K. Keshri, S.R. Bakshi, L. Kos, A. Agarwal, Boron nitride nanotube reinforced polylactide–polycaprolactone copolymer composite: Mechanical properties and cytocompatibility with osteoblasts and macrophages in vitro, *Acta Biomaterialia*. 6 (2010) 3524–3533. doi:10.1016/j.actbio.2010.02.044.
- [20] D. Askeland, P. Fulay, W. Wright, *The Science and Engineering of Materials*, 6th ed., Cengage Learning, Stamford, 2009.
- [21] C. Ramirez, P. Miranzo, M. Belmonte, M.I. Osendi, P. Poza, S.M. Vega-Diaz, M. Terrones, Extraordinary toughening enhancement and flexural strength in Si₃N₄ composites using graphene sheets, *Journal of the European Ceramic Society*. 34 (2014) 161–169. doi:10.1016/j.jeurceramsoc.2013.08.039.
- [22] A. Nieto, L. Huang, Y.-H. Han, J.M. Schoenung, Sintering behavior of spark plasma sintered alumina with graphene nanoplatelet reinforcement, *Ceramics International*. 41 (2015) 5926–5936. doi:10.1016/j.ceramint.2015.01.027.

- [23] N.G. Chopra, A. Zettl, Measurement of the elastic modulus of a multi-wall boron nitride nanotube, *Solid State Communications*. 105 (1998) 297–300.
[http://dx.doi.org/10.1016/S0038-1098\(97\)10125-9](http://dx.doi.org/10.1016/S0038-1098(97)10125-9).
- [24] C. Ramirez, M.I. Osendi, Toughening in ceramics containing graphene fillers, *Ceramics International*. 40 (2014) 11187–11192. doi:10.1016/j.ceramint.2014.03.150.
- [25] Q. Huang, Y. Bando, X. Xu, T. Nishimura, C. Zhi, C. Tang, F. Xu, L. Gao, D. Golberg, Enhancing superplasticity of engineering ceramics by introducing BN nanotubes, *Nanotechnology*. 18 (2007) 485706. doi:10.1088/0957-4484/18/48/485706.
- [26] W.-L. Wang, J.-Q. Bi, S.-R. Wang, K.-N. Sun, M. Du, N.-N. Long, Y.-J. Bai, Microstructure and mechanical properties of alumina ceramics reinforced by boron nitride nanotubes, *Journal of the European Ceramic Society*. 31 (2011) 2277–2284.
doi:10.1016/j.jeurceramsoc.2011.05.042.
- [27] M. Du, J.-Q. Bi, W.-L. Wang, X.-L. Sun, N.-N. Long, Microstructure and properties of SiO₂ matrix reinforced by BN nanotubes and nanoparticles, *Journal of Alloys and Compounds*. 509 (2011) 9996–10002. doi:10.1016/j.jallcom.2011.08.010.
- [28] D. Lahiri, V. Singh, A.P. Benaduce, S. Seal, L. Kos, A. Agarwal, Boron nitride nanotube reinforced hydroxyapatite composite: Mechanical and tribological performance and in-vitro biocompatibility to osteoblasts, *Journal of the Mechanical Behavior of Biomedical Materials*. 4 (2011) 44–56. doi:10.1016/j.jmbbm.2010.09.005.
- [29] J.-L. Tsai, T.-C. Lu, Investigating the load transfer efficiency in carbon nanotubes reinforced nanocomposites, *Composite Structures*. 90 (2009) 172–179.
doi:10.1016/j.compstruct.2009.03.004.

- [30] G.A. Shen, S. Namilae, N. Chandra, Load transfer issues in the tensile and compressive behavior of multiwall carbon nanotubes, *Materials Science and Engineering: A*. 429 (2006) 66–73. doi:10.1016/j.msea.2006.04.110.
- [31] C. Cheng, K.H. Müller, K.K.K. Koziol, J.N. Skepper, P.A. Midgley, M.E. Welland, A.E. Porter, Toxicity and imaging of multi-walled carbon nanotubes in human macrophage cells, *Biomaterials*. 30 (2009) 4152–4160. doi:10.1016/j.biomaterials.2009.04.019.
- [32] Y. Liu, J. Huang, H. Li, Synthesis of hydroxyapatite–reduced graphite oxide nanocomposites for biomedical applications: oriented nucleation and epitaxial growth of hydroxyapatite, *Journal of Materials Chemistry B*. 1 (2013) 1826. doi:10.1039/c3tb00531c.
- [33] S. Baradaran, E. Moghaddam, W.J. Basirun, M. Mehrali, M. Sookhakian, M. Hamdi, M.R.N. Moghaddam, Y. Alias, Mechanical properties and biomedical applications of a nanotube hydroxyapatite-reduced graphene oxide composite, *Carbon*. 69 (2014) 32–45. doi:10.1016/j.carbon.2013.11.054.
- [34] A. Shvedova, V. Castranova, E. Kisin, D. Schwegler-Berry, A. Murray, V. Gandelsman, A. Maynard, P. Baron, Exposure to Carbon Nanotube Material: Assessment of Nanotube Cytotoxicity using Human Keratinocyte Cells, *Journal of Toxicology and Environmental Health, Part A*. 66 (2003) 1909–1926. doi:10.1080/713853956.
- [35] H.-X. Ren, X. Chen, J.-H. Liu, X.-J. Huang, Toxicity of single - walled carbon nanotube: How we were wrong?, *Materials Today*. 13 (2010) 6–8.
- [36] M.A. Hussain, M.A. Kabir, A.K. Sood, On the cytotoxicity of carbon nanotubes, *Current Science*. 96 (2009) 664–673. http://repository.ias.ac.in/54812/1/19_pub.pdf (accessed February 14, 2016).

- [37] C. Bussy, M. Pinault, J. Cambedouzou, M.J. Landy, P. Jegou, M. Mayne - L'hermite, P. Launois, J. Boczkowski, S. Lanone, Critical role of surface chemical modifications induced by length shortening on multi-walled carbon nanotubes-induced toxicity, *Particle and Fibre Technology*. (2012) 1–15.
- [38] S. Jain, V.S. Thakare, M. Das, C. Godugu, A.K. Jain, R. Mathur, K. Chuttani, A.K. Mishra, Toxicity of Multiwalled Carbon Nanotubes with End Defects Critically Depends on Their Functionalization Density, *Chemical Research in Toxicology*. 24 (2011) 2028–2039.
doi:10.1021/tx2003728.
- [39] E.A. Olevsky, S. Kandukuri, L. Froyen, Consolidation enhancement in spark-plasma sintering: Impact of high heating rates, *J. Appl. Phys.* 102 (2007) 114913.
doi:10.1063/1.2822189.
- [40] W. Yao, J. Liu, T.B. Holland, L. Huang, Y. Xiong, J.M. Schoenung, A.K. Mukherjee, Grain size dependence of fracture toughness for fine grained alumina, *Scripta Materialia*. 65 (2011) 143–146. doi:doi: 10.1016/j.scriptamat.2011.03.032.
- [41] Y.W. Gu, N.H. Loh, K.A. Khor, S.B. Tor, P. Cheang, Spark plasma sintering of hydroxyapatite powders, *Biomaterials*. 23 (2002) 37–43.
<http://www.sciencedirect.com/science/article/pii/S014296120100076X> (accessed September 19, 2014).
- [42] Y. Gan, B. Zhou, Effect of grain size on the fracture toughness of nanocrystalline FeMoSiB, *Scripta Mater.* (2001) 625–630.
- [43] J. Wang, L.L. Shaw, Nanocrystalline hydroxyapatite with simultaneous enhancements in hardness and toughness, *Biomaterials*. 30 (2009) 6565–6572.
doi:10.1016/j.biomaterials.2009.08.048.

- [44] K. Budinski, M. Budinski, *Engineering Materials: Properties and Selection*, 6th ed., Prentice Hall, Upper Saddle River, 1999.
- [45] D. Leguillon, R. Piat, Fracture of porous materials – Influence of the pore size, *Engineering Fracture Mechanics*. 75 (2008) 1840–1853. doi:10.1016/j.engfracmech.2006.12.002.
- [46] D. Jauffrès, X. Liu, C.L. Martin, Fracture mechanics of porous ceramics using discrete element simulations, *Procedia Engineering*. 10 (2011) 2719–2724. doi:10.1016/j.proeng.2011.04.453.
- [47] D. Askeland, P. Fulay, W. Wright, *The Science and Engineering of Materials*, 6th ed., Cengage Learning, Stamford, 2009.
- [48] T. Anderson, *Fracture Mechanics: Fundamentals and Applications*, n.d.
- [49] K. Sairam, J.K. Sonber, T.S.R.C. Murthy, C. Subramanian, R.K. Fotedar, P. Nanekar, R.C. Hubli, Influence of spark plasma sintering parameters on densification and mechanical properties of boron carbide, *International Journal of Refractory Metals and Hard Materials*. 42 (2014) 185–192. doi:10.1016/j.ijrmhm.2013.09.004.
- [50] X.X. Wang, X.G. Tang, H.L.W. Chan, Electromechanical and ferroelectric properties of $(\text{Bi}_{1/2}\text{Na}_{1/2})\text{TiO}_3$ – $(\text{Bi}_{1/2}\text{K}_{1/2})\text{TiO}_3$ – BaTiO_3 lead-free piezoelectric ceramics, *Applied Physics Letters*. 85 (2004) 91. doi:10.1063/1.1767592.
- [51] H. Wang, J.-F. Li, C.-W. Nan, M. Zhou, W. Liu, B.-P. Zhang, T. Kita, High-performance $\text{Ag}_{0.8}\text{Pb}_{18+x}\text{SbTe}_{20}$ thermoelectric bulk materials fabricated by mechanical alloying and spark plasma sintering, *Applied Physics Letters*. 88 (2006) 92104. doi:10.1063/1.2181197.
- [52] B.-N. Kim, K. Hiraga, K. Morita, H. Yoshida, Spark plasma sintering of transparent alumina, *Scripta Materialia*. 57 (2007) 607–610. doi:10.1016/j.scriptamat.2007.06.009.

- [53] R.M. German, *Sintering Theory and Practice*, John Wiley & Sons, Inc., New York, 1996.
- [54] M.N. Rahaman, *Ceramic processing and sintering*, CRC, 2003.
- [55] J. Kubler, *Fracture Toughness of Ceramics using the SEVNB Method*, n.d.
http://www.astm.org/DIGITAL_LIBRARY/STP/PAGES/STP10473S.htm.
- [56] C28 Committee, *Standard Test Method for Flexural Strength of Advanced Ceramics at Ambient Temperature1*, ASTM International, n.d.
- [57] G.R. Anstis, P. Chantikul, B.R. Lawn, D.B. Marshall, A Critical Evaluation of Indentation Techniques for Measuring Fracture Toughness. I.—Direct Crack Measurements, *Journal of the American Ceramic Society*. 64 (1981) 533–538. http://www.ceramics.org/wp-content/uploads/2009/03/anstis_critical_evaluation.pdf (accessed January 29, 2016).
- [58] H. Miyazaki, Y. Yoshizawa, Novel measurement technique of crack length for indentation fracture (IF) method using high contrast image of crack tips through thin film coating, *Journal of the European Ceramic Society*. 35 (2015) 2943–2948.
doi:10.1016/j.jeurceramsoc.2015.04.008.
- [59] E04 Committee, *Test Methods for Determining Average Grain Size*, ASTM International, 2013. <http://www.astm.org/doiLink.cgi?E112> (accessed September 23, 2014).
- [60] G.D. Quinn, R.C. Bradt, On the Vickers Indentation Fracture Toughness Test, *Journal of the American Ceramic Society*. 90 (2007) 673–680. doi:10.1111/j.1551-2916.2006.01482.x.
- [61] M.G. Bothara, P. Vijay, S.V. Atre, S.J. Park, R.M. German, T.S. Sudarshan, R. Radhakrishnan, Design of experiment approach for sintering study of nanocrystalline SiC fabricated using plasma pressure compaction, *Science of Sintering*. 41 (2009) 125–133.
doi:10.2298/SOS0902125B.

- [62] L.J. Gibson, M.F. Ashby, B.A. Harley, Cellular Materials In Nature and Medicine, Cambridge University Press, n.d.
- [63] J.B. Wachtman, Mechanical Properties of Ceramics, 1st ed., John Wiley & Sons New York, New York, 1996.
- [64] Professional Reliability Analysis Routines and Reports, (n.d.).
<http://www.applicationsresearch.com/WeibullEase.htm>.
- [65] CDF, (n.d.).
<http://www.codecogs.com/library/statistics/distributions/continuous/weibull/cdf.php>.
- [66] T.B. Tran, Electric field-assisted sintering of nanocrystalline hydroxyapatite for biomedical applications, 2010. <http://adsabs.harvard.edu/abs/2010PhDT.....156T> (accessed August 13, 2016).
- [67] M. Geçgin, E. Alli, Y. Göncü, N. Ay, Mechanical properties of hydroxyapatite hexagonal boron nitride composites, (n.d.).
http://bildiri.anadolu.edu.tr/papers/bildirimakale/10625_b154c75.pdf (accessed April 27, 2016).
- [68] A. Royer, J.C. Viguie, M. Heughebaert, J.C. Heughebaert, Stoichiometry of hydroxyapatite: influence on the flexural strength, *Journal of Materials Science: Materials in Medicine*. 4 (1993) 76–82. <http://link.springer.com/article/10.1007/BF00122982> (accessed April 23, 2016).
- [69] A. Eskandari, M. Aminzare, H. Hassani, H. Barounian, S. Hesaraki, S. K Sadrnezhad, Densification behavior and mechanical properties of biomimetic apatite nanocrystals, *Current Nanoscience*. 7 (2011) 776–780.

<http://www.ingentaconnect.com/content/ben/cnano/2011/00000007/00000005/art00016>
(accessed February 16, 2016).

- [70] D. Lahiri, V. Singh, A.K. Keshri, S. Seal, A. Agarwal, Carbon nanotube toughened hydroxyapatite by spark plasma sintering: Microstructural evolution and multiscale tribological properties, *Carbon*. 48 (2010) 3103–3120. doi:10.1016/j.carbon.2010.04.047.
- [71] E. Prajatelista, Y.-H. Han, B.N. Kim, Y.-M. Kim, K. Lee, Y.-K. Jeong, D.-I. Kim, K.-H. Kim, S. Kim, Characterization of boron nitride-reinforced hydroxyapatite composites prepared by spark plasma sintering and hot press, *Journal of the Ceramic Society of Japan*. 121 (2013) 344–347. <http://jlc.jst.go.jp/DN/JALC/10016665322?from=Google> (accessed June 19, 2016).
- [72] Y. Liu, Z. Shen, Dehydroxylation of hydroxyapatite in dense bulk ceramics sintered by spark plasma sintering, *Journal of the European Ceramic Society*. 32 (2012) 2691–2696. doi:10.1016/j.jeurceramsoc.2012.02.025.
- [73] J. Cihlář, A. Buchal, M. Trunec, Kinetics of thermal decomposition of hydroxyapatite bioceramics, *Journal of Materials Science*. 34 (1999) 6121–6131. <http://link.springer.com/article/10.1023/A:1004769820545> (accessed August 29, 2015).
- [74] P.E. Wang, T.K. Chaki, Sintering behaviour and mechanical properties of hydroxyapatite and dicalcium phosphate, *Journal of Materials Science: Materials in Medicine*. 4 (1993) 150–158. <http://link.springer.com/article/10.1007/BF00120384> (accessed December 2, 2014).
- [75] C. Kothapalli, M. Wei, A. Vasiliev, M.T. Shaw, Influence of temperature and concentration on the sintering behavior and mechanical properties of hydroxyapatite, *Acta Materialia*. 52 (2004) 5655–5663. doi:10.1016/j.actamat.2004.08.027.

- [76] H. Tanaka, A. Yamamoto, J. Shimoyama, H. Ogino, K. Kishio, Strongly connected MgB polycrystalline bulks fabricated by solid-state self-sintering, *Superconductor Science and Technology*. 25 (2012) 115022. doi:10.1088/0953-2048/25/11/115022.
- [77] D. Lahiri, A. Hadjikhani, C. Zhang, T. Xing, L.H. Li, Y. Chen, A. Agarwal, Boron nitride nanotubes reinforced aluminum composites prepared by spark plasma sintering: Microstructure, mechanical properties and deformation behavior, *Materials Science and Engineering: A*. 574 (2013) 149–156. doi:10.1016/j.msea.2013.03.022.
- [78] K.K. Chawla, *Ceramic Matrix Composites*, 1st ed., Chapman & Hall, London, n.d.
- [79] P.D. Warren, Fracture of brittle materials: effects of test method and threshold stress on the Weibull modulus, *Journal of the European Ceramic Society*. (2000) 335–342.
- [80] Quinn, George D., J.B. Quin, A practical and systematic review of Weibull statistics for reporting strengths of dental materials, *Dental Materials*. 2 (2010) 135–147.
<http://www.ncbi.nlm.nih.gov/pmc/articles/PMC3086645/>.
- [81] J. Jin, H. TAKAHASHI, N. IWASAKI, Effect of test method on flexural strength of recent dental ceramics, *Dental Materials Journal*. 23 (2004) 490–496.
<http://jlc.jst.go.jp/DN/JALC/00246039628?from=Google> (accessed June 17, 2016).
- [82] R. Danzer, On the relationship between ceramic strength and the requirements for mechanical design, *Journal of the European Ceramic Society*. 34 (2014) 3435–3460.
doi:10.1016/j.jeurceramsoc.2014.04.026.
- [83] G.D. Quinn, Brian T. Sparenberg, P. Koshy, L.K. Ives, S. Jahanmir, D.D. Arola, Flexural strength of ceramic and glass rods, *Journal of Testing and Evaluation*. 37 (2009) 1–23.
http://www.astm.org/DIGITAL_LIBRARY/JOURNALS/TESTEVAL/PAGES/JTE101649.htm (accessed June 17, 2016).

- [84] Y. Fan, M. Estili, G. Igarashi, W. Jiang, A. Kawasaki, The effect of homogeneously dispersed few-layer graphene on microstructure and mechanical properties of Al₂O₃ nanocomposites, *Journal of the European Ceramic Society*. 34 (2014) 443–451. doi:10.1016/j.jeurceramsoc.2013.08.035.
- [85] L.S. Walker, V.R. Marotto, M.A. Rafiee, N. Koratkar, E.L. Corral, Toughening in Graphene Ceramic Composites, *ACS Nano*. 5 (2011) 3182–3190. doi:10.1021/nn200319d.
- [86] E.L. Corral, J. Cesarano, A. Shyam, E. Lara-Curzio, N. Bell, J. Stuecker, N. Perry, M. Di Prima, Z. Munir, J. Garay, E.V. Barrera, Engineered Nanostructures for Multifunctional Single-Walled Carbon Nanotube Reinforced Silicon Nitride Nanocomposites, *Journal of the American Ceramic Society*. 91 (2008) 3129–3137. doi:10.1111/j.1551-2916.2008.02533.x.
- [87] N. Cuadrado, J. Seuba, D. Casellas, M. Anglada, E. Jiménez-Piqué, Geometry of nanoindentation cube-corner cracks observed by FIB tomography: Implication for fracture resistance estimation, *Journal of the European Ceramic Society*. 35 (2015) 2949–2955. doi:10.1016/j.jeurceramsoc.2015.03.031.
- [88] C28 Committee, Standard Test Method for Vickers Indentation Hardness of Advanced Ceramics, ASTM International, 2015.
- [89] P.J. Tumidajski, L. Fiore, T. Khodabocus, M. Lachemi, R. Pari, Comparison of Weibull and normal distributions for concrete compressive strengths, *Canadian Journal of Civil Engineering*. 33 (2006) 1287–1292. doi:10.1139/106-080.
- [90] D. Koc, A. Dogan, B. Bek, Bite force and influential factors on bite force measurements: a literature review, *Eur J Dent*. 4 (2010) 223–232. <https://pdfs.semanticscholar.org/5ae3/cbd3b467b1574908b1db76ada4f05162b090.pdf> (accessed February 5, 2017).

- [91] Y. Watanabe, T. Ikoma, A. Monkawa, Y. Suetsugu, H. Yamada, J. Tanaka, Y. Moriyoshi, Fabrication of Transparent Hydroxyapatite Sintered Body with High Crystal Orientation by Pulse Electric Current Sintering: *Communications of the American Ceramic Society, Journal of the American Ceramic Society*. 88 (2004) 243–245. doi:10.1111/j.1551-2916.2004.00041.x.
- [92] D. Schachter, The source of toxicity in CTAB and CTAB-stabilized gold nanorods, Rutgers University-Graduate School-New Brunswick, 2013.
<https://rucore.libraries.rutgers.edu/rutgers-lib/39676/> (accessed March 11, 2017).
- [93] L. Huang, X. Chen, Q. Li, Synthesis of microporous molecular sieves by surfactant decomposition, *Journal of Materials Chemistry*. 11 (2001) 610–615. doi:10.1039/b005770n.
- [94] A.S. McCall, C.F. Cummings, G. Bhave, R. Vanacore, A. Page-McCaw, B.G. Hudson, Bromine Is an Essential Trace Element for Assembly of Collagen IV Scaffolds in Tissue Development and Architecture, *Cell*. 157 (2014) 1380–1392.
doi:10.1016/j.cell.2014.05.009.
- [95] G. Ciofani, G.G. Genchi, I. Liakos, A. Athanassiou, D. Dinucci, F. Chiellini, V. Mattoli, A simple approach to covalent functionalization of boron nitride nanotubes, *Journal of Colloid and Interface Science*. 374 (2012) 308–314. doi:10.1016/j.jcis.2012.01.049.
- [96] University of Liverpool, Hydroxyapatite $\text{Ca}_5(\text{OH})(\text{PO}_4)_3$, (n.d.).
<http://www.chemtube3d.com/solidstate/SShydroxyapatite.htm>.